

Spectroscopic ellipsometry on tailored siloxane-based nanostructures for low-voltage dielectric elastomer actuators

Inauguraldissertation

zur

Erlangung der Würde eines Doktors der Philosophie

vorgelegt der

Philosophisch-Naturwissenschaftlichen Fakultät

der Universität Basel

von

Tino Töpfer

aus Arnstadt, Deutschland

Basel, 2017

Originaldokument gespeichert auf dem Dokumentenserver der Universität Basel
<http://edoc.unibas.ch>



Dieses Werk ist lizenziert unter einer Creative Commons Namensnennung 4.0
<https://creativecommons.org/licenses/by/4.0>

Genehmigt von der Philosophisch-Naturwissenschaftlichen Fakultät auf Antrag von:

Prof. Dr. Bert Müller, Fakultätsverantwortlicher
Prof. Dr. Ernst Meyer, Korreferent

Basel, den 21. Juni 2016

Prof. Dr. Jörg Schibler, Dekan

Contents

Summary	v
Zusammenfassung	vii
List of Publications	xi
1 Introduction - ‘Smartsphincter’	1
1.1 Dielectric elastomer actuators	1
1.2 Compliant metal electrodes	2
1.3 Nanometer-thin polydimethylsiloxane films	3
1.4 Real-time spectroscopic ellipsometry	4
2 Results	5
2.1 Tailoring the mass distribution and functional group density of dimethyl- siloxane-based films by thermal evaporation	5
2.2 Characterization of ultraviolet light cured polydimethylsiloxane films for low-voltage, dielectric elastomer actuators	13
2.3 Strain-dependent characterization of electrode and polymer network of electrically activated polymer actuators	24
2.4 Siloxane-based thin films for biomimetic low-voltage dielectric actuators	36
2.5 Time resolved plasmonics on self-assembled hetero-nanostructures for soft nanophotonic and electronic devices	47
3 Conclusions and Outlook	79
Bibliography	82
Acknowledgments	87
Curriculum Vitae	88

Summary

To convert electric energy into mechanical motion dielectric elastomer actuators (DEAs) are known for their high strains combined with low power consumption. Based on micrometer-thick elastomer films DEAs are an established technology to serve as artificial muscles for soft robotics. The ‘Smartsphincter‘ project aims to develop artificial muscles to treat fecal incontinence. However, to use DEAs as medical implants, operation voltages have to be reduced from the kV-range well below the medically approved limit of 42 V. Hence, this work pursues the fabrication of nanometer-thin elastomer layers to enable the low-voltage operation of DEAs. To guarantee the acceptance as medical implant DEAs are composed of biocompatible materials. The excellent elasticity of cross-linked polydimethylsiloxane (PDMS) in combination with its biocompatibility renders PDMS the polymer of choice for a large range of medical applications, including DEAs. Due to its inherent chemical inertness combined with outstanding conductance, Au is considered as biocompatible electrode. Organic molecular beam deposition (OMBD) is a versatile technique employed to produce nanometer-thin films with unique homogeneity, however, for polymer material OMBD faces the challenge of evaporating oligomers at a reasonable rate at temperatures well below thermal degradation.

Herein, we present thermally evaporated linear PDMS serving as thin polymer films with a tailored molecular weight distribution (cp. Section 2.1). Limited by intermolecular interactions between the methyl side groups, molecular weights of up to 6.000 ± 100 g/mol corresponding to up to 80 repeating units of dimethylsiloxane are evaporated before thermal degradation. The functional group density per repeating unit dimethylsiloxane is adjusted between (2.8 ± 0.2) g/mol and (11 ± 0.1) g/mol. These thermally evaporated PDMS fractions exhibit a narrowed MWD with polydispersity index (PDI) of 1.06 ± 0.02 compared to the highly dispersive supplied polymer. The low PDI enables precise definition of functional group density anticipated to qualify for functionalized surfaces of biomedical devices e.g. microfluidic applications or tailoring cell-polymer interactions. Furthermore, we highlight the evaporation of high molecular weight PDMS chains to be of great importance to realize low elastic modulus cross-linked thin elastomer films.

Cross-linking of these PDMS macromolecules is activated through ultraviolet (UV) radiation, which induces a photo-initiated reaction of radicalized functional vinyl terminations. Nano-indentation and infrared spectroscopic studies clarify the understanding of the cross-linking mechanism in section 2.2 and section 2.4. Due to the strong absorption coefficient of PDMS in the UV-range, the cross-linking density is increased within the first nanometers of the film compared to the bulk indicating a skin-like SiO₂ surface. This stiffened silica-like surface combined with heat input through UV irradiation results in isotropic distributed wrinkled surface microstructures. Magnetron-sputtered gold coatings can release these wrinkled microstructures, which is accounted for a pre-stretching of the Au/SiO₂/PDMS heterostructure. This suggests these heterostructures to qualify for stretchable electronics.

One straightforward approach for increased electrode flexibility is a reduced metal-film thickness, which is applicable for gold films above 10 nm revealing the drawback of reduced conductivity (cp. section 2.2). Regarding DEA-based artificial muscles, strains higher than 10 % with maintained conductivity are needed to provide millisecond response time. As an important milestone within the ‘SmartSphincter’-project an OMBD system was setup, combining the deposition of metal and polymer as well as the UV-polymerization. Simultaneous *in situ* spectroscopic ellipsometry (SE) monitoring paves the way to tailor soft multilayer metal/elastomer heterostructures on the nanometer scale (cp. section 2.5). Synthesized bi-functional thiol-terminated PDMS was specifically tailored concerning the MWD for thermal evaporation to serve as self-assembled adhesion monolayer (SAM) for gold. It is hypothesized that the SH-PDMS chains and the subsequently evaporated Au form a viscous composite. Cross-linked to the underlying PDMS membrane, the SH-PDMS induces stability, which permits the generation of confluent Au films with a thickness as low as (12 ± 1) nm. We demonstrated a remarkably reduced percolation threshold at a film thickness of (4.4 ± 0.3) nm if a nanometer-thin wrinkled Cr-interlayer is applied to the PDMS membrane. Our results suggest a dramatic improvement towards homogeneous Au growth on soft PDMS membranes. We claim the specifically tailored hetero nanostructures to retrieve some flexibility under strain due to either localized covalent gold-thiol bonds or pre-stretched nanometer-thin Cr-wrinkles, especially beneficial for soft and stretchable nanoelectrodes.

To prove the envisioned concept a single layer DEA is presented (cp. section 2.4). Manufactured on a 25 μm -thick polyetheretherketone (PEEK) cantilever the bending characteristic gave evidence of a maintained actuation efficiency for a 200 nm-thin film, activated with voltages from 1 to 12 V, compared to a 4 μm -thick, spin-coated film, operated between 100 and 800 V. The force of this 200 nm-thin film cantilever actuator was about 10^{-4} N. Thus, a multilayer DEA with more than 10^4 layers would reach forces comparable to natural muscles.

To tackle the major drawback of OMBD, exhibiting evaporation rates limited below 0.1 nm/s, a cooperative study with the EMAP in Dübendorf aimed to validate alternate current electro-spray (ACES) as a cost-effective growth technique for nanometer-thin PDMS films. As presented for OMBD, *in situ* SE real-time analysis approved ACES to qualify for DEA manufacturing (Florian Weiss *et al.*, see publication list) permitting deposition rates above 10 $\mu\text{m}/\text{h}$. However, at these growth rates we obtained rather free-standing islands than a confluent film formation resulting in micrometer-rough surface morphologies. Thus, the outstanding homogeneity with sub-nanometer surface roughness accentuates OMBD better for soft nanotechnology.

Combining OMBD self-assembly with SE real-time tailoring of the electronic and optical properties allows the manufacturing of the nanometer-thin heterostructures with a unique precision. Soft, transparent, and biocompatible hetero-nanostructures based on electrically activated polymers are applicable to bio-MEMs, in nanophotonics as soft tuneable gratings or plasmonic absorbers, and flexible electronics. We propose a high impact for these nanostructures developing DEAs towards low-voltage operation. As unique property, sensing and actuating can be achieved concurrently within the same DEA hetero nanostructure. The fabrication of biocompatible actuator/sensor structures with compliance similar to that of human tissue is key to mimic natural muscles for biocompatible implants or soft robotics.

Zusammenfassung

Dielektrische Elastomer-Aktuatoren (DEA) sind bekannt für ihre hohe Flexibilität und zusammen mit ihrem geringen Energieverbrauch eignen sie sich besonders für die Umwandlung von elektrischer Energie in mechanische Arbeit. Basierend auf mikrometerdicken Elastomerschichten haben sich DEAs vor allem im Bereich von Robotik als künstliche Muskeln etabliert. Das ‘SmartSpincter‘-Projekt zielt darauf ab, die natürliche Muskelfunktion auf DEA-Basis zu imitieren und smarte Implantate zur Behandlung von Inkontinenz herzustellen. Um DEAs aber als medizinische Implantate einzusetzen zu können, muss die Betriebsspannung aus dem kV-Bereich unter das medizinisch akzeptierte Limit von 42 V reduziert werden. In dieser Arbeit wird der Ansatz der Schichtdickenreduktion in den Bereich von hunderten von Nanometern verfolgt um die Betriebsspannung auf wenige Volt zu reduzieren. Um die medizinische Akzeptanz zu garantieren, müssen biokompatible Materialien verwendet werden. Die exzellente Elastizität im vernetzten Zustand kombiniert mit Biokompatibilität macht Polydimethylsiloxane (PDMS) zum Polymer der Wahl für eine Vielzahl an medizinischen Anwendungen. Wegen seiner chemischen Widerstandsfähigkeit und der besonderen Leitfähigkeit wird Gold von uns als biokompatible Elektrode eingesetzt. Organische Molekularstrahldeposition (OMBD) verspricht eine vielseitige Methode für Polymerdünnfilme, jedoch steht sie vor der Herausforderung diese mit angemessenen Wachstumsraten innerhalb ihrer thermischen Stabilität zu verdampfen.

Wir demonstrieren das kontrollierte Wachstum von thermisch verdampften PDMS mit maßgeschneiderter Molekulargewichtsverteilung (MWD) (section 2.4). Durch Van-der-Waals Wechselwirkungen zwischen Methyl Seitengruppen der PDMS-Ketten limitiert, wurden Molekulargewichte von bis zu (6.000 ± 100) g/mol, korrespondierend zu 80 dimethylsiloxane Wiederholungseinheiten, vor ihrem thermischer Zerfall verdampft. Der Anteil funktioneller Gruppen pro Wiederholungseinheit dimethylsiloxane konnte zwischen (2.8 ± 0.2) g/mol und (11 ± 0.1) g/mol justiert werden. Verglichen zum bereitgestellten Original-PDMS haben die verdampften PDMS Fraktionen eine verschmälerte Molekulargewichtsverteilung (MWD) mit einer Polydispersität (PDI) von 1.06 ± 0.02 . Diese geringe Polidispersität ermöglicht es, die Dichte der funktionellen Gruppen präzise zu definieren, sodass sich PDMS Dünnfilme dazu qualifizieren, funktionalisierte Oberflächen für biomedizinische Geräte, beispielsweise mikrofluidische Anwendungen oder für Zell-Polymer Wechselwirkungssexperimente. Zudem ist das erfolgreiche Verdampfen von hohen PDMS-Molekulargewichten mit mehr als 80 dimethylsiloxane Wiederholungseinheiten von großer Bedeutung, um kleine Elastizitätsmodule für polymerisierte PDMS-Dünnfilme zu realisieren.

Durch photoinitierte Radikalreaktion, basierend auf ultraviolettem (UV) Licht, wurde das Vernetzen dieser PDMS Makromoleküle über die funktionellen Vinyl-Gruppen induziert. Eine detaillierte Atomkraftmikroskopie Studie zusammen mit infraroter Spektroskopie verdeutlicht den Vernetzungsmechanismus in section 2.2 and section 2.4. Wegen des hohen Absorptionskoeffizienten bei dieser Wellenlänge ist die Ver-

netzungsdichte von PDMS in den ersten Nanometern der Schicht höher, verglichen mit dem darunterliegenden PDMS Film, was auf eine filmartige SiO₂ Oberfläche zurückzuführen ist. Diese SiO₂-artige Oberfläche führt zusammen mit dem Wärmeeintrag zu einer isotropisch-gefalteten mikrostrukturierten Oberfläche. Magnetron-gesputterete Goldfilme können diese Faltenstrukturen wieder relaxieren was durch eine Art vorgespannte Au-SiO₂-PDMS Heterostruktur erklärbar ist. Das würde diese Heterostrukturen ausgesprochen für flexible Elektronik qualifizieren.

Ein unkomplizierter Ansatz für erhöhte Elektrodenflexibilität ist, die Schichtdicke des Metallfilms zu verringern (section 2.3). Dieses Prinzip ist für Goldfilmdicken oberhalb von 10 nm limitiert und geht einher mit sinkender Leitfähigkeit. Bezüglich DEA-basierten künstlichen Muskeln werden allerdings Dehnungen oberhalb von 10 % mit gleichbleibender Leitfähigkeit vorausgesetzt um die Reaktion im millisekunden Bereich zu garantieren. Als wichtiger Meilenstein innerhalb des ‘SmartSphincter’-Projektes wurde eine OMBD Kammer installiert, welche das Verdampfen von Polymer, Metallen, sowie die *in situ* UV-Behandlung der PDMS Schichten gleichzeitig ermöglicht. Simultane Echtzeitüberwachung des Wachstums mit spektroskopische Ellipsometry (SE) ebnet den Weg um multi-lagige Metall/Elastomer nanometer-dünne Heterostrukturen maßzuschneidern (section 2.5). Bi-funktionales thiol-PDMS (SH-PDMS) mit zugeschnittenem Molekulargewicht wurde synthetisiert um als selbstorganisierte monolagige (SAM) Adhesionsschicht für Gold zu dienen. Es ist anzunehmen, dass diese Schicht von Goldclustern eingebettet in die 7 nm-dünne unpolymerisierte SH-PDMS Schicht eine viskose Matrix formen. Bei gleichzeitiger UV-Beleuchtung der SH-PDMS Schicht während der Golddeposition ergaben sich geordnete kovalente Au-S Bindungen, welche stabilisiert werden durch Vernetzung der SH-PDMS Ketten mit der darunterliegenden PDMS Membran. Schließende Goldfilme werden dann schon ab einer Schichtdicke von (12 ± 1) nm erreicht. Eine bemerkenswerte Verringerung der Perkolationsschwelle wurde bei einer Goldfilmdicke von (4.4 ± 0.3) beobachtet, wenn gefaltene Cr-PDMS Heterostrukturen als Adhensionszwichenschicht angewendet werden. Unsere Resultate zeigen eine bemerkenswerte Verbesserung in Richtung eines homogenen Goldwachstums auf PDMS Dünnschichten. Wir behaupten, dass die Flexibilität der eingeführten Heterostrukturen unter Dehnung, entweder durch lokalisierte kovalente Au-S Bindungen oder durch vorgespannte Cr/PDMS Faltenoberflächen, erhalten bleibt.

Um das vorgestellte Konzept von Dünnschichtaktuatoren zu evaluieren, wurde ein dielektrischer Einzelschichtaktuator realisiert (cp. section 2.4). Fabriziert auf einem 25 μm -dicken polyetheretherketone (PEEK) Biegebalken ergab sich eine gleichbleibende Aktuatoreffizienz für einen 200 nm-dünnen Aktuator, welcher zwischen 1 und 12 V betrieben wurde, verglichen zu einem 4 μm -dicken Aktuator, welcher zwischen 100 and 800 V betrieben wurde. Dieser Aktuator, basierend auf einem 200 nm-Dünnschicht, erreichte eine Kraft im Bereich von 10^{-4} N. Somit müsste ein Multischichtaktuator, mit einer Schichtanzahl oberhalb von 10^4 Schichten, eine Kraft vergleichbar mit der von natürlichen Muskeln erreichen.

Die in dieser Arbeit präsentierten Resultate illustrieren einen erheblichen Fortschritt in Richtung einer verlässlichen Fabrikation von weichen, flexiblen PDMS/Metall Nanostrukturen mittels OMBD. Um den hauptsächlichsten Nachteil von limitierten Wachstumsraten von OMBD unterhalb von 0.1 nm/s anzusprechen, wurde eine Kooperation in Dübendorf vorangetrieben, in der Electro-spray (ACES), mit Wach-

tumsraten oberhalb von $10\ \mu\text{m}/\text{h}$, als alternativer Prozess für PDMS Dünnschichten validiert wurde. Wie auch für OMBD demonstriert, ist mithilfe von *in situ* SE die Qualität der ACES-gewachsenen Elastomerfilme als geeignet für Dünnschicht-DEAs empfunden worden (Florian Weiss *et al.*, siehe Publikationsliste). Es wurde jedoch beobachtet, dass für hohe Wachstumsraten ein Inselwachstum dominiert, welches in eine Morphologie mit mikrometer-rauer Oberfläche resultiert. Dies hebt OMBD als geeigneter für Polymer-Nanotechnologie hervor.

OMBD kombiniert mit SE erlaubt ein verlässliches Maßschneiden von elektronischen und optischen Eigenschaften von nanometer-dünnen Metall/Elastomer Heterostrukturen mit einzigartiger Präzision und Homogenität. Flexible, durchsichtige und biokompatible Heterostrukturen auf DEA-Basis finden Anwendung in BioMEMS, der Nanophotonik als abstimmbare Gitter oder plasmonische Absorber und dehnbare Elektronik. Schließlich behaupten wir, dass OMBD ein verlässliches Wachstum für eine Produktion von mehrschichtigen DEA Strukturen ermöglicht. Diese werden benötigt um die Kräfte natürlicher Muskeln nachzuahmen. Dazu haben wir einen Beweis geliefert, welcher einen Einschichtaktuator im Niederspannungsbetriebsmodus unter $12\ \text{V}$ präsentiert. Die außergewöhnliche Eigenschaft von Sensor und Aktuatorfähigkeit innerhalb derselben Heterostruktur macht Dünnschichtaktuatoren besonders interessant für Applikationen außerhalb medizinischer Implantate zum Beispiel für nanophotonische Sensoren oder abstimmbare Gitter und Linsen in der Mikrooptik. Hier möchten wir nochmals hervorheben, dass die Herstellung von weichen, dehnbaren und biokompatiblen DEA-Strukturen einen Schlüssel darstellt, um Aktuatoren mit mechanischen Eigenschaften vergleichbar zu denen von menschlichen Gewebe zu realisieren.

List of Publications

- T. Töpfer**, S. Lörcher, B. Osmani, V. Leung, T. Pfohl, B. Müller, “Time resolved plasmonics on self-assembled hetero-nanostructures for soft nanophotonic and electronic devices ” *submitted to Nature Nanophotonics*.
- F. Weiss**, Frederikke B. Madsen, B. Osmani, V. Leung, T. Töpfer, B. Müller, “Molecular beam deposition of high-permittivity polydimethylsiloxane for nanometer-thin elastomer films in dielectric actuators” *Materials and Design*, (2016), **105**, 106-113
- T. Töpfer**, S. Lörcher, F. Weiss, B. Müller, “Tailoring the mass distribution and functional group density of dimethylsiloxane-based films by thermal evaporation ” *APL Materials*, **4** 056101(2016) (doi:10.1063/1.4949362)
- T. Töpfer**, F. Wohlfender, F. Weiss, B. Osmani, B. Müller, “Characterization of ultraviolet light cured polydimethylsiloxane films for low-voltage, dielectric elastomer actuators.” *Proceedings of SPIE* **9798** 979821 (2016). (doi:10.1117/12.2218608)
- B. Osmani**, H. Deyhle, F. Weiss, T. Töpfer, M. Karapetkova, V. Leung, B. Müller, “Morphology and conductivity of Au electrodes on polydimethylsiloxane using (3-mercaptopropyl)trimethoxysilane (MPTMS) as an adhesion promoter.” *Proceedings of SPIE* **9798** 979822 (2016). (doi:10.1117/12.2219199)
- V. Leung**, E. Fattorini, M. Karapetkova, B. Osmani, F. Weiss, T. Töpfer, B. Müller, “ Biomimetic artificial sphincter muscles: status and challenges .” *Proceedings of SPIE* **9797** 97970M (2016). (doi:10.1117/12.2219090)
- F. Weiss, **T. Töpfer**, B. Osmani, H. Deyhle, G. Kovacs, B. Müller, “Thin film formation and morphology of electro-sprayed polydimethylsiloxane” *Langmuir*, **32** (13), 3276-3283 (2016).
- F. Weiss, **T. Töpfer**, B. Osmani, S. Peters, G. Kovacs, B. Müller, “Electro-spraying nanometer-thin elastomer films for low-voltage dielectric actuators” *Advanced Electronic Materials*, 1500476 (2016). (doi:10.1002/aelm.201500476)
- B. Osmani, **T. Töpfer**, F. Weiss, F. Wohlfender, V. Leung, C. Bippes, B. Müller, “Nanomechanical characterization of polydimethylsiloxane films.” *European Cells and Materials* **30** Supplement 1, 56 (2015)
- T. Töpfer**, B. Osmani, F. Weiss, B. Müller, “Viscoelastic properties of Polydimethylsiloxane studied by cantilever bending.” *European Cells and Materials* **30** Supplement 1, 68 (2015).
- T. Töpfer**, F. Weiss, B. Osmani, C. Bippes, V. Leung, B. Müller, “Siloxane-based thin films for biomimetic low-voltage dielectric actuators.” *Sensors and Actuators A* **233** 32-41 (2015). (doi:10.1016/j.sna.2015.06.014)

T. Töpfer, B. Osmani, F. Weiss, C. Winterhalter, F. Wohlfender, V. Leung, B. Müller, “Strain-dependent characterization of electrode and polymer network of electrically activated polymer actuators.” *Proceedings of SPIE* **9430** 94300B (2015). (doi:10.1117/12.2084595)

B. Osmani, **T. Töpfer**, C. Deschenaux, J. Nohava, F. Weiss, V. Leung, B. Müller, “Micro- and nanostructured electro-active polymer actuators as smart muscles for incontinence treatment.” *AIP Conference Proceedings* **1646** 91-100 (2015). (doi:10.1063/1.4908588)

F. Weiss, **T. Töpfer**, B. Osmani, C. Winterhalter, B. Müller, “Impact of electrode preparation on the bending of asymmetric planar electro-active polymer microstructures.” *Proceedings of SPIE* **9056** 905607 (2014).

1 Introduction - ‘Smartsphincter‘

Current aging of society leads to the increasing prevalence of social and economic burdening by age-related diseases. Among them fecal incontinence (FI), describing the involuntary loss of bowel content, affects more than 10% of the western population.¹ Severe consequences involve exclusion from social life, isolation, and stigmatization. Prevalence rates for urinary incontinence (UI) are higher for women than in men and ranging between 4.5 to 53% and 1.6 to 24%, respectively.² The number of patients suffering from incontinence increases with age. Statistically recorded figures of incontinence are said to be underestimated since it is often unuttered. Thus it has a considerable, but underrated, economic impact.³ For patients with moderate conditions of incontinence non-invasive treatments such as nervous stimulation or specific exercises of the pelvic floor muscles can be sufficient. As alternative medication the insertion of absorbing materials is considered. Contrary, in severe cases operational interventions are necessary. Available implants, however, are not part of everyday surgery due to long-term re-operation rates of 95% and definitive explantation rates of 40%. These studies indicate that up-to-date implants fail to reproduce the capabilities of the natural sphincter.³ Thus the increasing demand for smart solutions from medical doctors motivates the focused research on ‘Smart Sphincters‘.

A promising actuation principle is based on dielectric electro-active polymer actuators (DEA), especially attractive because of their versatility, millisecond response time, reaction forces, and high energy efficiency.⁴ This technology could enable fast pressure adaption comparable to the natural feedback mechanism, so that tissue atrophy and erosion can be avoided while maintaining continence during daily activities.

The required performance of electronics was developed by the Swiss Federal Laboratories for Materials Science and Technology (EMPA, Eidgenössische Materialprüfungs- und Forschungsanstalt). To increase the adaptivity and degree of biointegration, clinicians from Bern and Schaffhausen specified the required standards for the implant and developed a biomechanical model of the pelvic floor.

1.1 Dielectric elastomer actuators

Actuators based on the electro-active polymer (EAP) technology, also called dielectric elastomer actuators (DEAs), consist of two electrodes embedding a dielectric material. It is essential for DEAs to have an elastic dielectric material in order to allow for contraction and relaxation back to its original state. When a voltage U is applied between the two electrodes, an electrostatic pressure p leads to a strain in the vertical direction s_z , which is then, due to the incompressibility of the polymer network, equally translated into a strain in horizontal directions (cp. Eq. (1.1)).

$$s_z = Yp = Y\epsilon_0\epsilon_r E^2 = Y\epsilon_0\epsilon_r \left(\frac{U}{d}\right)^2 \quad (1.1)$$

The Maxwell pressure is directly proportional to the dielectric constant ϵ_r and quadratically dependent on the elastomer film thickness d and the applied voltage U . The vacuum permittivity is represented by ϵ_0 . The elastomeric material with elastic modulus Y is assumed to be incompressible meaning its volume must remain constant. Typically for the application within the field of robotics, driven voltages for DEAs are in the range of several 100 V. Regarding their power consumption, the necessary currents in combination with the high voltages are incompatible with physiological surroundings. Consequently, the design of dielectric EAPs has to be modified for low-voltage operation below 42 V to adapt for medical applications. Therefore, one should either increase the dielectric constant of the polymer, for example by adding fillers in the elastomer network^{5,6}, or decrease the film thickness to reduce the operation voltage. Based on Eq. 1.1 the change in elastomer film thickness would have a pronounced impact on the operation voltage compared to the change in dielectric constant. Taking advantage of organic molecular beam deposition (OMBD), this project targets the reduction of film thickness to the sub-micrometer range. Compared with the well-established spin coating, solvents are not required. In order to reach the necessary actuation forces stacking to multi-layer actuators is required. The dielectric elastomer material of choice is polydimethylsiloxane (PDMS). The excellent elasticity of cross-linked PDMS networks in combination with their biocompatibility renders PDMS the polymer of choice for a large range of medical applications. Gold, which is known for the high electric conductivity and its chemical inertness is utilized as the base material for electrode layer.

1.2 Compliant metal electrodes

Materials ranging from noble metals to graphene, composites,^{7,8} and conducting polymers⁹ have been investigated. The process complexity and the outstanding conductivities make metals the material of choice to charge the whole surface area on a millisecond time scale as desired for artificial sphincter implants. In contrast it has to be considered that metal films itself only allow for strains below 2%.¹⁰ As the elastic modulus of nobles metals is orders of magnitude above them of the elastomer layer the stiffening effect of the electrode has to be accounted regarding nanometer-thin multi-layer actuators. Thus, it is essential to realize compliant electrodes in order to maintain functionality of DEA structures.

Common methods to create metal electrodes for DEAs are magnetron sputtering, thermal evaporation and ion implantation. In contrast to the first two techniques, ion implantation does not lead to confluent metal films, but rather to PDMS/metal composites. Furthermore the diffusion depth of ion implanted Au-particles ranges up to a few tens of nanometer.¹¹ Difficult to control the process ion implantation is found to be not suitable for nanometer-thin DEAs.

Bi-layer systems of soft bulk polymer and rigid thin metal coatings have been studied for applications in packaging and microelectronics. It has been found, for example, that ultra-thin noble metal films on polymers including polydimethylsiloxane (PDMS) give rise to strains well above 10%.¹⁰ To optimize the polymer films as well

as the ultra-thin metal electrodes two techniques combined allow the electrical and mechanical properties of the actuators to be quantified. Four-point measurement, a well-established technique that allows the electrode resistivity characterization,¹² is applied on strained nanometer-thin gold films. The electrical conductivity of the electrodes is directly related to the response time of the engineered artificial muscle. In addition, mechanical properties such as elasticity of the stacked multilayers is extracted from cantilever-bending measurements. This principle is an established technique and used in a broad range of applications, for example atomic force microscopy.^{13,14} We have previously demonstrated that cantilever bending is a method well suited to evaluate EAP microstructures with high angular resolution at low voltages.^{15,16} Morphological details detected by optical and atomic force microscopy do support the quantitative results obtained by the four-point conductivity and cantilever-bending measurements.

Induced by the low surface energy of cured PDMS the adhesion of pure gold films on PDMS is problematic. Thus, additional adhesion layers are considered. Cr-films as adhesion promoter for gold on PDMS are well established. Corrugation effects during Cr-deposition occur due to the heat energy transferred from the evaporation source and the thermal energy of the atoms arriving on the PDMS film surface.¹⁷ The heated PDMS reacts with thermal expansion during the deposition and enlarges its surface area, which is simultaneously covered by metal. After deposition the PDMS shrinks towards to its original state hindered by the stiffening metal film and thus evolving into a wrinkled equilibrium state. Applying an unidirectional pre-strain during deposition is has been shown to yield aligned wrinkle formation with enhanced actuation performance.¹⁵

Herein, the formation of complex multilayer hetero nanostructure architectures is validated by spectroscopic ellipsometry.

1.3 Nanometer-thin polydimethylsiloxane films

Another crucial improvement towards low-voltage DEAs is the aspect of homogeneous nanometer-thin PDMS growth. Currently, efforts have been published regarding electro-spray deposition (ESD). This technique has been shown to be very effective for homogeneous nanoscale film or particle formation especially for inorganic materials¹⁸ or polymers.^{19,20} In cooperation with F.M. Weiss *et al.* we presented alternate current electro-spraying to be qualified for nanoscale PDMS film fabrication.²¹ Droplets of solution with a very low concentration of PDMS are accelerated within a high-voltage electric field exploding into smaller droplets with a homogeneous size distribution. This event is called a coulomb explosion.²² To manufacture nanometer-thin elastomeric films for multi-stack DEAs by ESD, the ac mode prevents charge accumulation on the substrate since only the first electrode is grounded. However, at high deposition rates confluent films were only detected for film thicknesses above one micrometer.²³ Thus, for the realization of PDMS films with only hundreds of nanometer in thickness an enhanced homogeneity is demanded. Physical vapor phase deposition is a versatile technique employed to produce nanometer-thin films.

Molecular beam deposition (MBD) well established for semiconductor materials²⁴ is a physical deposition from the gas phase, well-known for thin film growth with

homogeneity better than 2 %. Molecules in gas phase directed towards the substrate have no interaction between each other. Hence, their mean free path is orders of magnitude greater than the distance between evaporator and substrate allowing for precise process control.²⁵ MBD of polymer materials (OMBD)²⁶, however, faces the challenge to evaporate oligomers at a reasonable rate at temperatures below thermal degradation. Solely the sublimation of intact organic molecules under ultra-high vacuum conditions (10^{-9} mbar) has been accomplished through growth rates ranging from 5 to 6 nm/min.²⁷ Within this work the deposition of PDMS chains with up to 80 repeating units of dimethylsiloxane is presented for the first time. Molecular weights can be tailored by controlling the evaporation temperature.²⁸ The deposition and subsequent ultraviolet light curing is monitored in real-time with spectroscopic ellipsometry.

In addition, mechanical properties of the cured PDMS film such as elasticity and viscoelasticity are crucial for the success of DEAs. Cantilever-bending measurements are presented to characterize the cross-linking density of PDMS films and the actuation efficiency of nanometer-thin, low-voltage DEA microstructures.

1.4 Real-time spectroscopic ellipsometry

Recently, comprehensive studies on electro-spray film formation have presented spectroscopic ellipsometry as a powerful tool to obtain optical properties and morphology of polymer films simultaneously. Based on nuclei growth models even films with micrometer surface roughness can be characterized.^{21,23} On the other hand sub-nanometer structures of thermally grown PDMS films have been observed.²⁹ In addition the evolution of thermally grown metal films on soft polymer can be characterized.³⁰ As a result excited surface plasmons on nanoclusters within the dielectric function show prominent resonance peaks. Within this work the monitoring of real time plasmonics on nanostructured Au/PDMS composites is presented in section 2.5. Real-time determination of optical properties is based on a spectroscopic ellipsometer (SE801, Sentech, Berlin, Germany) with SpectraRay3 software. The spectroscopic Ψ and Δ data points ranged from 190 and 1050 nm are monitored at a frequency between 0.5 to 6 Hz at an incident angle of 70° . The incident beam diameter of 4 nm resulted in a measurement spot of $4 \times 10 \text{ mm}^2$. This highlights our spectroscopic measurement setup to obtain the film formation with millisecond resolution on a macroscopic area.

2 Results

2.1 Tailoring the mass distribution and functional group density of dimethyl-siloxane-based films by thermal evaporation

Molecular beam deposition enables the evaporation of single polydimethylsiloxane chains at temperatures below thermal degradation of functional groups.

Side groups of linear polydimethylsiloxane chains dominate intermolecular interactions and thus their vapor pressure.

The unique flexibility of linear polydimethylsiloxane enables folding at the crucible surface such that evaporated molecular weights can be tailored to maximum 6.000 g/mol corresponding to 80 repeating units of dimethylsiloxane.

Thermally evaporated polydimethylsiloxane fractions exhibit a narrow molecular weight distribution with polydispersity index of 1.06.

The content of functional end groups can be tailored between 2.8 to 11 %.

Published in APL Materials



Tailoring the mass distribution and functional group density of dimethylsiloxane-based films by thermal evaporation

Tino Töpfer,¹ Samuel Lörcher,² Florian Weiss,¹ and Bert Müller¹

¹Biomaterials Science Center, University of Basel, 4123 Allschwil, Switzerland

²Chemistry Department, University of Basel, 4056 Basel, Switzerland

(Received 23 February 2016; accepted 1 May 2016; published online 13 May 2016)

The tailoring of molecular weight distribution and the functional group density of vinyl-terminated polydimethylsiloxane (PDMS) by molecular beam deposition is demonstrated herein. Thermally evaporated PDMS and its residue are characterized using gel permeation chromatography and nuclear magnetic resonance. Thermal fragmentation of vinyl groups occurs for evaporation temperatures above 487 K (214 °C). At a background pressure of 10^{-6} mbar, the maximum molecular weight distribution is adjusted from (700 ± 100) g/mol to (6100 ± 100) g/mol with a polydispersity index of 1.06 ± 0.02 . The content of vinyl-termination per repeating unit of PDMS is tailored from $(2.8 \pm 0.2)\%$ to $(5.6 \pm 0.1)\%$. Molecular weights of vinyl-terminated PDMS evaporated at temperatures above 388 K (115 °C) correspond to those attributed to trimethyl-terminated PDMS. Side groups of linear PDMS dominate intermolecular interactions and vapor pressure. © 2016 Author(s). All article content, except where otherwise noted, is licensed under a Creative Commons Attribution (CC BY) license (<http://creativecommons.org/licenses/by/4.0/>). [<http://dx.doi.org/10.1063/1.4949362>]

Poly(dimethylsiloxane) (PDMS) is the most widely used silicone polymer.¹ Its backbone exhibits relatively high flexibility associated with a glass transition temperature as low as -125 °C and a melting temperature of -50 °C.² Because of its thermal and chemical stability, PDMS serves a broad range of applications, such as lubricants, adhesives, or passivation layers in the electronic and automotive industries.¹ The excellent elasticity of cross-linked PDMS networks in combination with their biocompatibility renders PDMS the polymer of choice for a large range of medical applications, including dielectric elastomer actuators (DEAs) for artificial muscles.^{3,4} Nanometer-thin films, with a homogeneity superior to that reached by current spin-coating or electro-spraying, have to be prepared.^{5,6} Physical vapor phase deposition is a versatile technique employed to produce nanometer-thin films. The molecular beam deposition (MBD)^{7,8} of polymer materials, however, faces the challenge of evaporating oligomers at a reasonable rate at temperatures well below thermal degradation. The sublimation of intact organic molecules under ultra-high vacuum conditions (10^{-9} mbar) has been realized through growth rates ranging from 5 to 6 nm/min.^{9,10} A recently published study describes the successful MBD of PDMS under high-vacuum conditions (10^{-6} mbar) at evaporation temperatures of up to 453 K (180 °C) and showing growth rates above 2 nm/min.³ Thermal stability, characterized by bond dissociation energies, has been investigated in detail. The cleavage of the Si–O backbone bonds results in the formation of cyclic oligomers with a corresponding activation energy of 180 kJ/mol.¹¹ It is known that dissociation energies of functional side groups are below those of the backbone bonds. The thermally activated decomposition of trimethyl-terminated PDMS under vacuum conditions occurs at a temperature of about 573 K (300 °C) with an activation energy of 175 kJ/mol.¹² An activation energy level of 98 kJ/mol¹² and a decomposition temperature of 503 K (230 °C) are found for vinyl termination.³

The evaporated oligomer mass depends exponentially on the inverse temperature according to the Clausius-Clapeyron relation. Thus, we hypothesize that MBD influences molecular weight distribution, polydispersity, and the density of the functional termination of the deposited polymer film.



Since the chain length of the oligomers determines the elastic modulus of cross-linked PDMS,¹³ the choice of deposition parameters determines the performance of DEAs.¹⁴ So far, thermal evaporation has been restricted to linear or cyclic PDMS, focusing on oligomers, i.e., macromolecules with less than eleven repeating units, with molecular weights below 1000 g/mol,^{15–17} or on the vaporization of decomposed PDMS fractions, using an evaporation temperature of 573 K (300 °C) at atmospheric pressures.¹⁸ In the present communication, vinyl-terminated PDMS is evaporated with molecular weights of up to 6100 g/mol, maintaining vinyl termination.

Our experimental setup has been described previously.³ Briefly, deposition experiments were carried out under high-vacuum conditions with a background pressure of 10^{-7} mbar. A low temperature effusion cell (Dr. Eberl MBE Komponenten GmbH, Weil der Stadt, Germany) with a 2 cm³ crucible was utilized. The temperature ramp of the evaporator was adjusted to 8.3×10^{-3} K/s to avoid boiling retardation. The final crucible temperature was held stable for one extra hour. With an opened shutter background pressure increased to 10^{-6} mbar, the substrate was mounted 300 mm in front of the evaporation source. The MBD study was based on two commercially available vinyl-terminated PDMS compounds both acquired from Gelest, Inc., Morrisville, PA, USA of which DMS-V21 has an average molecular weight of 6000 g/mol and DMS-V05 one of 800 g/mol. The PDMS starting materials were filled in the crucible as received from the supplier. Gel permeation chromatography (GPC) traces are recorded in WinGPC (v8.20 build 4815) and connected to an Agilent 1200 system equipped with a refractive index detector and a series of analytical SDV columns (pre-column (5 cm), 1×10^3 Å (30 cm), and 1×10^5 Å (30 cm), all 5 μm particles and 0.8 cm in diameter, PSS, Germany). The columns and the system were kept at a temperature of 35 °C and run at a flow rate of 0.017 ml s⁻¹. Average molecular weight M_n , mass average molecular weight M_w , peak molecular weight M_p , and the polydispersity index (PDI) were determined by calibrating the GPC system with narrow polystyrene standards from Sigma Aldrich.

The molecular weight distributions of the evaporated film fractions and the residues in the crucible after deposition are displayed as colored lines for DMS-V05 in Figs. 1(a) and 1(c) and for DMS-V21 in Figs. 1(b) and 1(d), respectively. The molecular weight distributions of the supplied materials are displayed as black lines. As expected, the peak molecular weight within the evaporated film fractions increases in line with temperature. The maximal evaporated molecular weight,

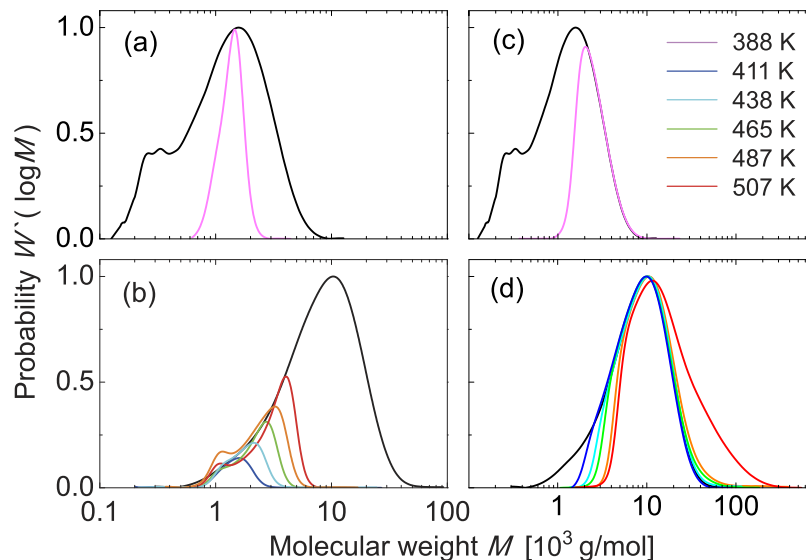


FIG. 1. Molecular weight distribution obtained from gel permeation chromatography traces of DMS-V05 [(a) and (c)] and DMS-V21 [(b) and (d)] is shown in black. The colored traces represent the film fractions evaporated from DMS-V05 (a) and DMS-V21 (b) as well as the corresponding residues [(c) and (d)] within the crucible at temperatures between 388 and 507 K.

extracted at $1/10^2$ - halfwidth of the GPC trace, ranges from (2000 ± 100) to (6100 ± 100) g/mol for evaporation temperatures between 388 K (115 °C) and 507 K (234 °C). The 100 g/mol error arises from estimating baseline variation. The molecular weight distributions of the supplied polymers cover a range between 150 to about 8000 g/mol for DMS-V05 and 600 to about 50 000 g/mol for DMS-V21, see black traces in Figure 1. These broad distributions offer the evaporation of same polymer fractions with both supplied polymers at a given temperature. Though, the increased availability of short-chain polymer within the DMS-V05 weight distribution results in increased growth rates pronounced for evaporation temperatures below 465 K. For an evaporation temperature of 388 K, a twenty times higher evaporation rate of (0.685 ± 0.005) nm/s for DMS-V05 compared to one of (0.035 ± 0.001) nm/s for DMS-V21 is detected within the present experimental configuration. Within the residual fraction, only polymers with a higher molecular weight than those deposited are detected. Their weight distribution exhibits a lower limit that corresponds to the highest molecular weights found in the evaporated fraction. At a crucible temperature of 507 K, molecular weights higher than those originally found in the supplied materials are detected. We attribute this finding to the thermal stability limit of the vinyl-double bond, which exhibits the lowest bond dissociation energy along the PDMS chain.¹⁹ The radicalization of vinyl groups leads to bond formation between PDMS chains, thus accounting for the increase in molecular weight.

Nuclear magnetic resonance ($^1\text{H-NMR}$) PDMS spectra were recorded on a Bruker DPX-400 spectrometer in deuterated chloroform without tetramethylsilane. They were then analyzed and processed (phase correction and Wittaker Smoother to adjust the baseline) in MestReNova 10.0.1-14 719 (Mestrelab Research S.L., Spain). The supplied PDMS is characterized by a distinct multiplet of around 0.1 ppm, attributed to the methyl side groups on the silicon atoms, three doublets of doublets between 5.6 and 6.2 ppm associated with vinyl termination (Fig. 2(a)). Signals between 0.5 and 4.1 ppm result from contaminants representing most likely residuals from the polymer synthesis. The characteristic peaks of vinyl and methyl groups are present at all evaporation temperatures ranging from 388 to 507 K in the evaporated as well as in the residual fractions. Thus, the combination of NMR with GPC analysis indicates the suitability of vinyl-terminated PDMS for thermal evaporation at temperatures of up to 487 K. At an evaporation temperature of 507 K, chain prolongation is observed within the residual fraction. Nevertheless, within the NMR data, no pronounced decrease in the vinyl chemical shift is found at that temperature (Fig. 2(c)).

The measured intensities of methyl and vinyl peaks are not calibrated values. They depend on the polymer concentration within the NMR tube. The density of vinyl groups is obtained by creating the ratio of the integral over the vinyl doublets of doublets and the integral over the chemical shifts of the methyl peak, cf. Fig. 2. Vinyl content, which specifies the number of vinyl terminations per repeating unit, is plotted in Fig. 3(a) as a function of deposition temperature. The vinyl content of the supplied material is determined to be $(1.35 \pm 0.07)\%$ for DMS-V21 and $(9.2 \pm 0.2)\%$ for DMS-V05 displayed at a temperature of 293 K in Fig. 3(a). Within the standard derivation, this agrees with the vinyl content of peak molecular weight derived from GPC measurements with $(1.28 \pm 0.03)\%$ and $(9.5 \pm 0.3)\%$ for supplied DMS-V21 and DMS-V05, respectively. For DMS-V05 deposited at a temperature of 388 K, a decrease in vinyl content to $(5.6 \pm 0.2)\%$ is observed. Conversely, an increase in vinyl content to $(4.0 \pm 0.2)\%$ is detected for DMS-V21 evaporated at a temperature of 407 K. Thus, either a reduction in vinyl group density for the evaporated DMS-V05 or an increase in the evaporated DMS-V21 fractions is realized. Independent of the molecular weight distribution of the supplied materials, the vinyl content of evaporated PDMS decreases with increasing evaporation temperature (Fig. 3(a) filled symbols) in line with an increased PDI (Fig. 3(b)). Within the range of thermal stability, i.e., at temperatures below 487 K, the vinyl content of deposited PDMS fractions decreases from $(5.6 \pm 0.2)\%$ to $(2.8 \pm 0.1)\%$ in line with increasing temperature.

The PDIs of the supplied materials are determined at 1.98 ± 0.02 (DMS-V05) and 1.87 ± 0.02 (DMS-V21) displayed at a temperature of 293 K in Fig. 3(b). For DMS-V05 evaporated at a temperature of 388 K, an explicit reduction of PDI to 1.06 ± 0.02 has been realized. DMS-V21 evaporated at a temperature of 411 K exhibited a PDI of 1.08 ± 0.02 . Using an evaporation temperature of 507 K for DMS-V21, the PDI became significantly larger and corresponded to 1.26 ± 0.20 . Thus, one can generally state that the PDI increases with the evaporation temperature, as the probability

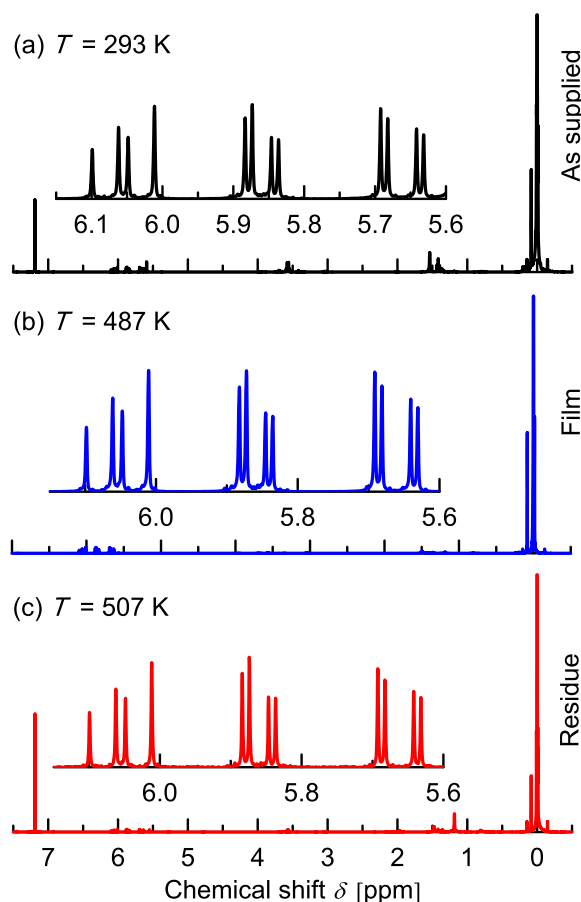


FIG. 2. Exemplary nuclear magnetic resonance spectra of supplied DMS-V21 at room temperature: (a) the film evaporated at a temperature of 487 K (b) and its residue in the crucible evaporated at a temperature of 507 K (c). The peaks attributed to the vinyl groups (multiplet from 5.6 to 6.1 ppm) are present before and after evaporation. ^1H NMR (400 MHz, CHCl_3 , δ): 0.1, m, $-\text{Si}-\text{O}-\text{Si}((\text{CH}_3)_2)-$, 6.06 (dd, $J = 20.3, 14.8$ Hz, 1H), 5.86 (dd, $J = 14.8, 4.0$ Hz, 1H), 5.66 (dd, $J = 20.2, 4.0$ Hz, 1H), m, $-\text{CHCH}_2$.

of long-chain molecule evaporation rises and the molecular weight distribution broadens to higher molecular weights. It is anticipated that by controlling the substrate temperature, low-molecular weight chains will desorb during film deposition, and narrow molecular weight distributions will also be approachable at evaporation temperatures already above 388 K. The half-width of the molecular weight distribution is then determined solely by the broadening of the Boltzmann energy distribution, which enables the tailoring of a well-defined molecular weight and vinyl content of evaporated PDMS. Within the residue, the PDI decreases in line with increasing temperature caused by the extraction of low-molecular weight polymer. At an evaporation temperature of 507 K, a distinct increase in the PDI to 2.02 ± 0.03 occurs in the residue. This broadening behavior is correlated to PDMS chain extensions, cf. Fig. 1(d).

Peak molecular weights M_p of thin film fractions evaporated at selected temperatures between 388 K and 507 K are displayed in Fig. 4. The range of accessible molecular weights is framed by thermal degradation (above 487 K)—upper limit—and by background pressure—the lower limit. At a pressure of 10^{-6} mbar, oligomers with molecular weights below (700 ± 100) g/mol are not detected within the deposited film, cf. Fig. 1(a), because, presumably, they evaporated at rather low temperatures before the deposition experiment started. This correlates with vapor pressure data

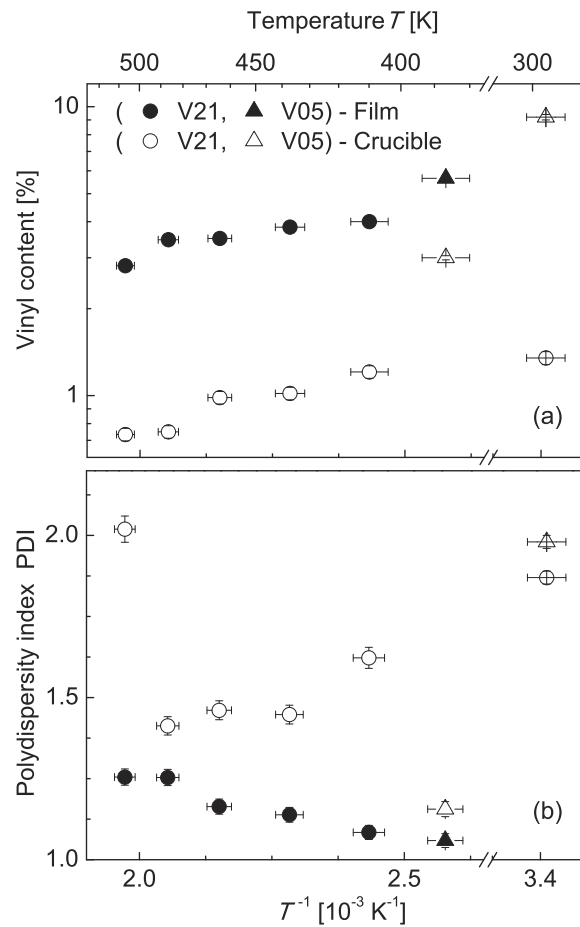


FIG. 3. The density of vinyl groups (a) and the polydispersity index (b) are presented with respect to the crucible temperature for the deposited films (filled circles, triangles) and its residue in the crucible (open circles, triangles). The supplied materials are shown as crossed symbols at a temperature of 293 K.

reported for trimethyl-terminated polysiloxanes.^{16,17} Thus, the peak molecular weights of deposited vinyl-terminated PDMS can be tailored within the range (700 ± 100) to (4050 ± 100) g/mol. The present data for vinyl-terminated PDMS, shown by the filled squares in Fig. 4, are compared with the experimental results from Ref. 16 represented by the open triangles in Fig. 4, where enthalpies of linear dimethylsiloxane oligomer vaporization with up to ten repeating units were determined at a background pressure of 10^{-2} mbar. To calculate the molecular weights of trimethyl-terminated PDMS evaporated at a background pressure of 10^{-6} mbar, the Clausius-Clapeyron relation with the coefficients of Ref. 17 is applied. Therefore, the molecular weights of the evaporated molecules depend linearly on the logarithm of the vapor pressure. For example, the reduction of the background pressure from 10^{-2} to 10^{-6} mbar results in a shift of the evaporated peak molecular weight at room temperature from 400 to 700 g/mol. In general, a reduced background pressure enables the evaporation of polymer with higher molecular weights. A comparison between the molecular weights of vinyl-terminated and trimethyl-terminated PDMS exhibits reasonable agreement between molecular weights of 700 to 1600 g/mol—a range which corresponds to eight to 19 repeating units of dimethylsiloxane. It is known that for PDMS oligomers with more than two repeating units of dimethylsiloxane, the side groups dominate intermolecular chain interactions and vaporization heat.¹⁷ Within the present study, evaporated polymers have molecular weights higher than

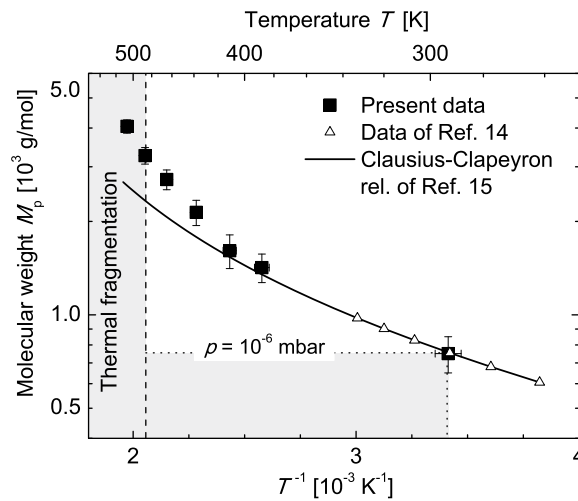


FIG. 4. The crucible temperature dependence of the peak molecular weight M_p of vinyl-terminated PDMS polymer (filled squares) is compared with derived vapor pressure data of trimethyl-terminated PDMS from Lei *et al.* (Ref. 16) (open triangles) and from Wilcock (Ref. 17) (line). Gray shading marks the boundaries of thermal fragmentation (dashed line) and the background gas pressure (dotted line).

(700 ± 100) g/mol with more than eight repeating units of dimethylsiloxane. Hence, we expect the contribution of vinyl groups to van der Waals interactions to be negligible for these chain lengths. Moreover, methyl side group interactions dominate the evaporation process.

For evaporation temperatures above 400 K, evaporated vinyl-terminated PDMS shows molecular weights higher than predicted by the Clausius-Clapeyron relation. The unique flexibility of the Si-O backbone presumably enables linear PDMS to form folded chains on the crucible surface. A conformational energy of 5 kJ/mol depicts the energy barrier of linear bending, which has to be overcome.²⁰ Energy barriers of 3.3 kJ/mol, corresponding to Si-O-Si rotation, and 0.4 kJ/mol, for methyl side group rotation, are even well below the energy barrier of linear bending.²⁰ This offers PDMS the chance to arrange its conformation at the melt-vacuum interface more easily than, for example, hydrocarbon or silane-based polymers. Thus, a stepwise breaking of intermolecular bonds and the subsequent bending of the PDMS chain explain the reduced vaporization heat, which emerge for PDMS with a molecular weight above 1600 g/mol, i.e., 19 repeating units. In general, the linear dimethylsiloxane exhibits exceptionally low intermolecular interactions obtained by shielding the Si-O backbone through the methyl groups. Thus, linear dimethylsiloxane with exclusively functional end termination offers the broadest range of molecular weights that can be tailored by MBD before thermal degradation. This behavior distinguishes PDMS from polyaniline-C₆₀,⁷ with a reduced oxidation state, or polythiophene (PTh),⁸ with a reduced conjugation length after thermal evaporation.

The maximal vinyl content of end-terminated PDMS can be adjusted to 11.1%, corresponding to nine repeating units of dimethylsiloxane evaporated just above a temperature of 293 K. Using copolymers with altered side terminations can extend the accessible range of functional group density. As a drawback, the substitution of methyl groups, for example, by vinyl or phenyl groups results in increased steric hindrance or polarity. The resulting increase in vaporization heat would narrow the spectrum of accessible molecular weights. The low PDI enables the well-defined functional group density content of evaporated PDMS. We anticipate that this technique will qualify for realizing the functionalized surfaces of biomedical devices, such as microfluidic applications,²¹ or tailoring cell-polymer interactions.¹⁸ We propose the incorporation of phenyl terminations, which helps to manipulate the refractive index to qualify for biosensor applications.²² Based on this functionalization, the dielectric constant can be adapted to influence actuation efficiency positively in dielectric elastomer actuators. Furthermore, the evaporation of high molecular weight polymer

056101-7 Töpfer *et al.*

APL Mater. 4, 056101 (2016)

is of great importance to realize low elastic modulus cross-linked thin elastomer films. This enables high actuation strains of dielectric elastomer actuators. Together with unique homogeneity, MBD of PDMS is expected to realize biocompatible dielectric actuators serving artificial muscle implants.^{23,24}

In summary, thermally evaporated linear dimethylsiloxane serves thin polymer films with a tailored molecular weight distribution. Limited by intermolecular interactions between the methyl side groups, molecular weights corresponding to up to 80 repeating units of dimethylsiloxane are evaporated before thermal degradation.

This work was funded by the Swiss National Science Foundation (Project No. 200021-135496) and by the nanotera.ch initiative, a collaboration between the Biomaterials Science Center (BMC) of the University of Basel, the Swiss Federal Laboratories for Material Science and Technologies (EMPA), the Institute for Surgical Technology and Biomechanics (ISTB), Kantonsspital Schaffhausen, and Inselspital Bern.

- ¹ H. F. Mark, *Encyclopedia of Polymer Science and Technology* (John Wiley & Sons, New York, 2014).
- ² S. J. Clarson and J. A. Semlyen, *Siloxane Polymers* (Prentice Hall PTR, 1993).
- ³ T. Töpfer, F. M. Weiss, B. Osmani, C. Bippes, V. Leung, and B. Müller, *Sens. Actuators, A* **233**, 32 (2015).
- ⁴ R. Pelrine, R. Kornbluh, Q. Pei, and J. Joseph, *Science* **287**(5454), 836 (2000).
- ⁵ D. B. Hall, P. Underhill, and J. M. Torkelson, *Polym. Eng. Sci.* **38**(12), 2039 (1998).
- ⁶ F. M. Weiss, T. Töpfer, B. Osmani, S. Peters, G. Kovacs, and B. Müller, "Electrospraying Nanometer-Thin Elastomer Films for Low-Voltage Dielectric Actuators," *Adv. Electron. Mater.* (to be published).
- ⁷ M. Irimia-Vladu, N. Marjanovic, A. Vlad, A. M. Ramil, G. Hernandez-Sosa, R. Schwödiauer, S. Bauer, and N. S. Sariciftci, *Adv. Mater.* **20**(20), 3887 (2008).
- ⁸ P. Kovacic, G. Sforazzini, A. G. Cook, S. M. Willis, P. S. Grant, H. E. Assender, and A. A. R. Watt, *ACS Appl. Mater. Interfaces* **3**(1), 11 (2011).
- ⁹ B. Müller, C. Cai, A. Kündig, Y. Tao, M. Bösch, M. Jäger, C. Bosshard, and P. Günter, *Appl. Phys. Lett.* **74**(21), 3110 (1999).
- ¹⁰ F. F. So, S. R. Forrest, Y. Q. Shi, and W. H. Steier, *Appl. Phys. Lett.* **56**(7), 674 (1990).
- ¹¹ K. Chenoweth, S. Cheung, A. C. T. van Duin, W. A. Goddard, and E. M. Kober, *J. Am. Chem. Soc.* **127**(19), 7192 (2005).
- ¹² G. Deshpande and M. E. Rezac, *Polym. Degrad. Stab.* **76**(1), 17 (2002).
- ¹³ J. E. Mark and J. L. Sullivan, *J. Chem. Phys.* **66**(3), 1006 (1977).
- ¹⁴ A. G. Bejenariu, L. Yu, and A. Ladegaard Skov, *Soft Matter* **8**(14), 3917 (2012).
- ¹⁵ O. L. Flaningam, *J. Chem. Eng. Data* **31**(3), 266 (1986).
- ¹⁶ Y. D. Lei, F. Wania, and D. Mathers, *J. Chem. Eng. Data* **55**(12), 5868 (2010).
- ¹⁷ D. F. Wilcock, *J. Am. Chem. Soc.* **68**(4), 691 (1946).
- ¹⁸ E. J. Park, K.-D. Kim, H. S. Yoon, M.-G. Jeong, D. H. Kim, D. Chan Lim, Y. H. Kim, and Y. D. Kim, *RSC Adv.* **4**(57), 30368 (2014).
- ¹⁹ Y. Israëli, J. Cavezzan, and J. Lacoste, *Polym. Degrad. Stab.* **37**(3), 201 (1992).
- ²⁰ J. S. Smith, O. Borodin, and G. D. Smith, *J. Phys. Chem. B* **108**(52), 20340 (2004).
- ²¹ L. Wong and C.-M. Ho, *Microfluid. Nanofluid.* **7**(3), 291 (2009).
- ²² S. Rahong, B. Saekow, S. Porntheerapat, J. Nukeaw, C. Hruanun, and A. Poyai, in *3rd Nanoelectronics Conference (INEC)* (IEEE, 2010), p. 1303.
- ²³ B. Müller, H. Deyhle, S. Mushkolaj, and M. Wieland, *Swiss Med. Wkly.* **139**(41-42), 591 (2009).
- ²⁴ E. Fattorini, T. Brusa, C. Gingert, S. E. Hieber, V. Leung, B. Osmani, M. D. Dominiotto, P. Büchler, F. Hetzer, and B. Müller, *Ann. Biomed. Eng.* **44**(5), 1355–1369 (2016).

2.2 Characterization of ultraviolet light cured polydimethylsiloxane films for low-voltage, dielectric elastomer actuators

Ultraviolet-light post-curing of submicrometer-thin PDMS films induces a gradient of cross-linking density.

Radicalization of methyl side groups leads to a silica-like surface of nanometer thickness.

The interplay of cross-linking gradient and heat input from the irradiation source leads to isotropic-distributed wrinkled microstructures on the film surface.

The amplitude can be tailored by irradiation intensity and film thickness.

UV-induced microstructures on PDMS thin-films coated with sputtered gold can be pre-stretched and qualify for DEA contact layers tolerating high strains.

Published in Proceedings of SPIE 2016

Characterization of ultraviolet light cured polydimethylsiloxane films for low-voltage, dielectric elastomer actuators

Tino Töpfer*, Fabian Wohlfender, Florian M. Weiss, Bekim Osmani, and Bert Müller

Biomaterials Science Center, Department of Biomedical Engineering, University of Basel, 4123 Allschwil, Switzerland.

ABSTRACT

The reduction the operation voltage has been the key challenge to realize of dielectric elastomer actuators (DEA) for many years - especially for the application fields of robotics, lens systems, haptics and future medical implants. Contrary to the approach of manipulating the dielectric properties of the electrically activated polymer (EAP), we intend to realize low-voltage operation by reducing the polymer thickness to the range of a few hundred nanometers. A study recently published presents molecular beam deposition to reliably grow nanometer-thick polydimethylsiloxane (PDMS) films. The curing of PDMS is realized using ultraviolet (UV) radiation with wavelengths from 180 to 400 nm radicalizing the functional side and end groups. The understanding of the mechanical properties of sub-micrometer-thin PDMS films is crucial to optimize DEAs actuation efficiency. The elastic modulus of UV-cured spin-coated films is measured by nano-indentation using an atomic force microscope (AFM) according to the Hertzian contact mechanics model. These investigations show a reduced elastic modulus with increased indentation depth. A model with a skin-like SiO₂ surface with corresponding elastic modulus of (2.29 ± 0.31) MPa and a bulk modulus of cross-linked PDMS with corresponding elastic modulus of (87 ± 7) kPa is proposed. The surface morphology is observed with AFM and 3D laser microscopy. Wrinkled surface microstructures on UV-cured PDMS films occur for film thicknesses above (510 ± 30) nm with an UV-irradiation density of $7.2 \cdot 10^{-4}$ J cm⁻² nm⁻¹ at a wavelength of 190 nm.

Keywords: ultraviolet curing, polydimethylsiloxane, nano-indentation, atomic force microscopy, 3D laser microscopy, polymer films

1. INTRODUCTION

The significance of age-related diseases has been increasingly pronounced by changing demographics of modern society. Among them fecal incontinence (FI) affects between 11 and 15 % of adults [1] and increases with age [2]. Artificial sphincters based on electrically activated polymer (EAP) actuator implants offer a possible solution to treat severe fecal incontinence. Yet, it remains a significant challenge for researchers to build artificial muscles, which reproduce the capabilities of the natural sphincter [3]. Based on the versatility of EAPs including response time, forces, and energy consumption [4], they can mimic the rapidly adaptive pressure response, comparable to the natural feedback mechanism of the human body. [5]

Regarding EAP actuators for biomimetic implants the focus lies on a significant reduction of the actuation voltages [6, 7]. Silicone-based polymer films, prepared by spin-coating, are limited to micrometer thickness and require operation voltages above several 100 V to reach thickness strains of 25 to 48 % [8]. Alternative techniques aim to realize nanometer-thin polymer films with actuation voltages below 42 V, e.g. alternate-current electro-spraying of polydimethylsiloxane (PDMS) in solution [9, 10]. However, this approach exhibits the drawback of inhomogeneous, non-confluent films formed by PDMS-droplets at film thicknesses below 600 nm. Contrary, molecular beam deposition (MBD) of PDMS has been presented as a promising growth technique for nanometer-thin elastomer films [11]. Based on that, EAP actuators did exhibit strains comparable to that of micrometer-thick EAPs with actuation voltages well below the approved medical limit. Combined with homogeneity of better than 2 %, MBD of polymers allows for a reliable and repeatable growth process for stacked actuators, which makes them promising candidates for biomimetic artificial muscles.

*tino.toepper@unibas.ch; phone 0041 61 207 54 45; fax 41 61 265 9699; www.bmc.unibas.ch

Electroactive Polymer Actuators and Devices (EAPAD) 2016, edited by Yoseph Bar-Cohen, Proc. of SPIE Vol. 9798, 979821 · © 2016 SPIE · CCC code: 0277-786X/16/\$18 · doi: 10.1117/12.2218608

Proc. of SPIE Vol. 9798 979821-1

The excellent elasticity of cross-linked PDMS, in combination with its biocompatibility, makes it the most widely used silicone polymer for medical applications, including EAPs [12]. Its backbone exhibits high flexibility associated with a glass transition temperature as low as $-125\text{ }^{\circ}\text{C}$ and a melting temperature of $50\text{ }^{\circ}\text{C}$ [13]. Additionally, linear siloxane-based PDMS offers the broadest range of molecular weight and functional group density to be tailored [14]. Cross-linking of PDMS is achievable through the presence of functional end- or side groups, activated either by heat-induced curing using a catalyst or applying ultraviolet (UV) radiation to force the photo-initiated reaction of radicals [15, 16]. The UV cross-linking of vinyl-terminated PDMS has been successfully shown [9, 11].

Nevertheless, the understanding of the resulting PDMS network properties is crucial for efficient EAP-actuator operation. It has been shown, that the elasticity of the elastomer film is directly proportional to the chain length of the cross-linked PDMS oligomers [17]. This directly affects the strain, realized by EAP actuators. For thick bulk materials, the elastic modulus is usually determined by using standard characterization methods such as the unconfined compression test [18]. In case of soft films with thicknesses below one micrometer, these bulk-testing methods are not applicable due to unknown contributions from the stiffness of the underlying substrate. For nanometer-thin polymer films, asymmetric cantilevers have been utilized to describe their elastic/ viscoelastic behavior under applied strain [19]. With the advantage of a less complex preparation process, nano-indentation (NI) recently received great attention for the determination of mechanical material properties on the micro- and nanometer scale. Thus, we present a detailed mechanical characterization of UV-cross-linked vinyl-terminated PDMS films with weight average molecular weights ranging from 800 to 62,000 g/mol. The elastic modulus is determined by NI with an atomic force microscopy (AFM).

It is well known, that UV-treatment with wavelengths below 200 nm affects the chemical stability of the methyl side groups as well as the functional terminations such as vinyl groups [20, 21]. UV-initiated decomposition results in the creation of a SiO_2 surface layer with thicknesses of about five nanometers [8]. Stress at the SiO_2 – PDMS interface induces a wrinkled surface structure. The morphology of UV-treated PDMS films of varying thickness is characterized by 3D laser microscopy and AFM surface scans. Electrically activated polymer actuators are based on sandwich structures consisting of an elastomer layer embedded between electrodes. Current research on biocompatible stretchable electronics has brought up a wide range of possible material and geometrically solution, e.g. carbon nanotube, graphene or silver nanowires [22, 23]. Nevertheless, due to its less complex deposition methods, electrodes consisting of sputtered or thermally evaporated gold are a reliable electrode material with maintained conductivity for strains above 20 % [24]. Thus, optical micrographs are presented to characterize the morphology of a sputtered 10 nm-thin Au film on a UV-treated PDMS film. A qualitative observation of strain release of the wrinkled PDMS surface will be provided.

2. EXPERIMENTAL

2.1 PDMS film preparation

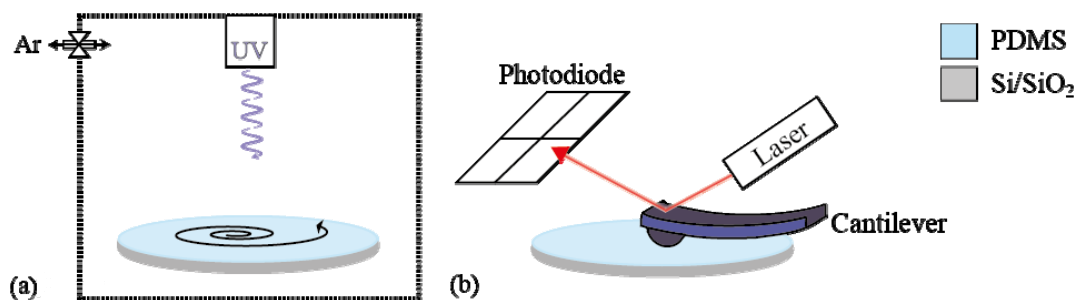


Figure 1. (a) The schematic UV-treatment setup of spin-coated PDMS films is shown. Applying an inert Ar atmosphere reduces UV-light absorption of oxygen. Sample rotation guarantees a homogenous irradiation profile. (b) The schematic principle of nano-indentation by atomic force microscopy is presented. The deflection of the laser beam induced by the cantilever bending is detected on a photodiode.

Vinyl-terminated dimethylsiloxanes DMS-V05, DMS-V21, DMS-V25, DMS-V31 and DMS-V41 (Gelest Inc., Morrisville, PA, USA) are spin-coated on Si-wafers using a tabletop spin-coater (WS-400B-6NPP, Laurell Technologies, North Wales, USA). The n-doped 3-inch Si(100) (Silicon Materials Inc., Pittsburgh, PA, USA) with a thickness (381 ± 25) μm are cleaned with ethyl acetate and acetone (both Merck KGaA, Darmstadt, Germany). Spin-coating

parameters of the five polymers are listed in Table 1. The rotation speed, spin-coating time and acceleration were individually adapted to receive comparable layer thicknesses.

Subsequently, the samples were UV-cured in Ar atmosphere using an in-house fabricated chamber with an attached deuterium lamp (H2D2 light source unit L11799, Hamamatsu Photonics K.K., Hamamatsu, Japan), *cf.* Figure 1(a). The spectrum of the deuterium UV lamp ranges from 160 to 400 nm, with a peak intensity at approximately 190 nm. The maximal power density of the deuterium lamp is $0.6 \mu\text{W cm}^{-2} \text{nm}^{-1}$ at 190 nm at a distance of 50 cm to the light source. The curing time was 1200 s.

The absolute thickness of the UV-cured PDMS film was determined using a spectroscopic ellipsometer SE801 (Sentech Instruments GmbH, Berlin, Germany).

Table 1. Weight average molecular weight M_w and viscosity of the supplied polymer and the processing parameters of the spin-coated film are presented.

Polymer	M_w [kg/mol]	Viscosity [cSt.]	Spin coating Speed [rpm] (time [s])	Film thickness [nm]
DMS-V05	0.8	4-8	2,000 (120)	985 ± 25
DMS-V21	6.0	100	5,500 (150)	$1,217 \pm 30$
DMS-V25	17.2	500	8,000 (240)	$1,331 \pm 35$
DMS-V31	28.0	1,000	8,000 (240)	$1,790 \pm 50$
DMS-V41	62.7	10,000	8,000 (240)	$2,600 \pm 60$

The Au-electrode layer was sputtered with a final thickness of 10 nm. The related sputtering conditions in the Balzers Union SCD 040 system (Balzers, Lichtenstein) corresponded to 0.05 mbar Ar-atmosphere (Carbagas AG, Gümligen, Switzerland) and a constant working current of 30 mA. The thickness was determined beforehand by a calibration curve plotting time versus thickness measured using a quartz crystal microbalance (QSG 301, Balzers, Balzers, Lichtenstein).

2.2 Nano-indentation measurements by atomic force microscopy

For the nano-indentation experiments a FlexAFM ARTIDIS system (Nanosurf AG, Liestal, Switzerland) was utilized. To reduce the maximum penetration depth of the cantilever tip, B150_CONTR cantilevers (Nanotools GmbH, Munich, Germany) with a spherical carbon-tip of $(150 \pm 15) \mu\text{m}$ were mounted. Load-displacement curves of all samples were measured with a constant speed while measuring the applied load. Adequate indentation parameters were evaluated with characterization measurements on an UV-cured DMS-V21 sample. An indentation speed of $0.5 \mu\text{m/s}$ was found to realize fast sample scanning and simultaneously suppress viscoelastic effects. The maximum applied load was set to 5 nN to limit the indentation depth below 150 nm. Thus, substrate effects can be neglected within the applied HERTZ model.

The measurement data was processed according to the HERTZ model, which is based on the classical Hertzian contact theory [18]. The deformation caused by spherical indentation is dependent on the applied load P and is described by the contact radius a as seen in Equation 1.

$$a^3 = \frac{6R}{8E_r} P \quad (1)$$

The proportional constants are the spherical indenter radius R and the reduced elastic modulus E_r . The stiffness S can be extracted from the slope of the load-displacement curves and is related to the contact radius a according to the following equation:

$$a = \frac{S}{2E_r} = \frac{1}{2E_r} \frac{dP}{dh} \quad (2)$$

Taking into account the Poisson's ratio ν_s of the sample, the elastic modulus of the soft polymer film can be expressed as given in Equation 3.

$$E_s = \sqrt{\frac{(1-\nu_s^2)^2}{6R}} \left(\frac{dP}{dh}\right)^3 \frac{1}{P} \quad (3)$$

Nano-indentation was executed on five spots of interest with 64×64 points corresponding to a spot size of $60 \mu\text{m} \times 60 \mu\text{m}$.

2.3 Morphology characterization by 3D laser microscopy and atomic force microscopy

Optical profilometry by means of a 3D laser scanning microscopy (Keyence VK-X200, Keyence International, Belgium) with 50 times optical magnification has been used to create surface profiles of $1 \times 1 \text{mm}^2$ in size with 2048×2048 points. For higher spatial resolution an atomic force microscope (AFM), FlexAFM ARTIDIS system, Nanosurf AG, Liestal, Switzerland, was applied. Here, areas of $97.5 \times 97.5 \mu\text{m}^2$ (512×512 points) were recorded in tapping mode with a Tap150Al-G tip (Budget Sensors, Innovative Solutions Bulgaria Ltd., Sofia, Bulgaria).

3. RESULTS

3.1 Elastic modulus of ultraviolet light cured polydimethylsiloxane films

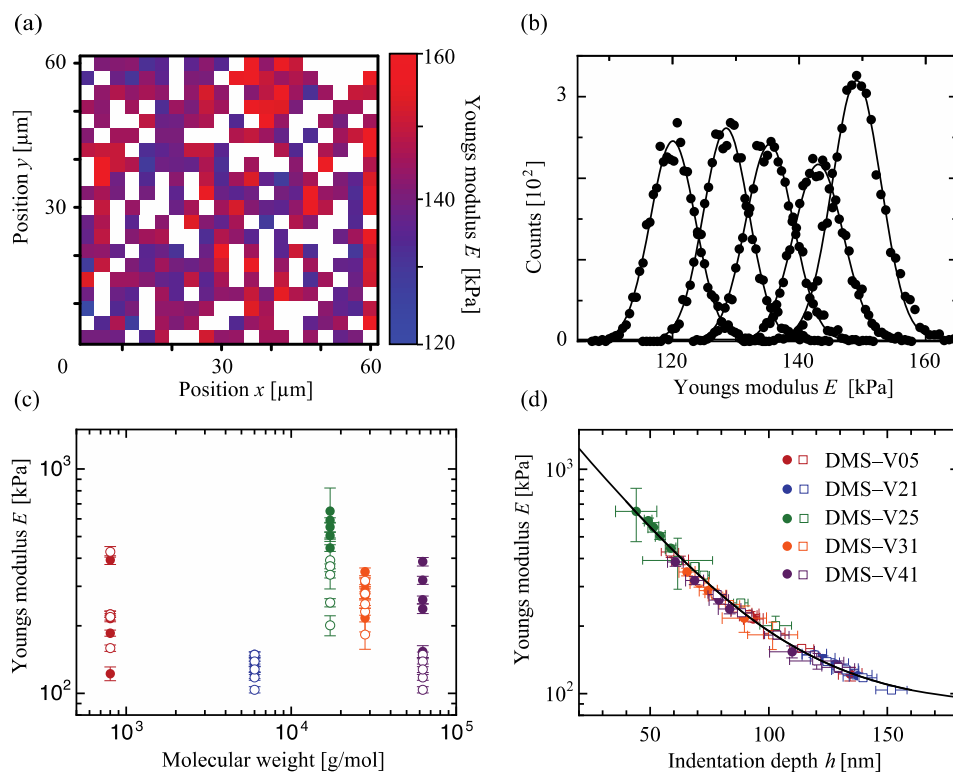


Figure 2. (a - b) Exemplary nano-indentation data on a UV-cured DMS-V21 film with a spot size of $60 \mu\text{m} \times 60 \mu\text{m}$ is presented. The color map represents the elastic modulus from 120 kPa (blue) to 160 kPa (red). White squares correspond to spots without suitable fit. The extracted elastic modulus distributions are displayed for five measurement areas on the PDMS film. A Gaussian fit characterizes the center of the elastic modulus distribution. (c) The extracted elastic moduli of forward (filled circles) and backward (open squares) load-displacement curve are plotted with respect to the molecular weights of the supplied polymers ranging from 800 g/mol for DMS-V05 to 62,700 g/mol for DMS-V41. (d) The elastic moduli are shown with respect to the indentation depth of the AFM tip. An exponential fit function is utilized to characterize the dependency, see Equation 4.

Figure 1 represents experimental data of the nano-indentation measurements of polydimethylsiloxane films. An exemplary 2D indentation map of a UV-cured DMS-V21 film is shown in panel (a). The values of the elastic modulus are displayed using a color map ranging from 120 kPa (blue) to 160 kPa (red) within the scanned area of $60 \mu\text{m} \times 60 \mu\text{m}$. White squares correspond to spots with no suitable fit processed to the load displacement curve according to Equation 3. The resulting distribution of the elastic moduli is presented in panel (b) of Figure 1 for five measurement spots randomly distributed over the 3-inch Si wafer. The peak elastic modulus is defined by the center of a Gaussian fit model. The corresponding error is given by the full width half maximum (FWHM).

Five measurement spots are analyzed for each UV-cured PDMS film composed of molecular weights ranging from 800 to 62,700 g/mol, see Table 1. The extracted elastic moduli of forward (filled circles) and backward (open squares) displacement curves are displayed as a double logarithmic plot in panel (c) of Figure 1. A distribution of elastic moduli between 100 and 700 kPa is observed for all samples prepared. No distinct dependency of film elastic modulus with respect to the consisting molecular weight of the polymer can be extracted. Contrary, a significant decrease of elastic modulus E with increasing indentation depth h of the AFM cantilever tip is found. This characteristic behavior can be described by an exponential fit:

$$E = \exp\left(\frac{A-h}{B}\right) + E_0 \quad (4)$$

The fit constants $A = (254 \pm 13) \text{ nm}$ and $B = (33 \pm 3) \text{ nm}$ are found. The y -axis offset is determined to $E_0 = (87 \pm 7) \text{ kPa}$. Thus, a decrease of elastic modulus from 2.29 MPa at zero nanometer indentation depth to 87 kPa at infinite indentation depth is observed independent of the molecular weight.

3.2 Surface morphology of ultraviolet light cured polydimethylsiloxane films

For the analysis of the thin film morphology the atomic force microscopy is a powerful tool. One can examine surface structures with nanometer resolution. Exemplary surface scans of the DMS-V21 UV-treated thin film are presented as $97.5 \times 97.5 \mu\text{m}^2$ and $24.5 \times 24.5 \mu\text{m}^2$ frames in Figure 1(a-b). The height variation on the surface spans a range of about $1.5 \mu\text{m}$. An extract of the Fourier transformation of part (a) in Figure 1 reveals no distinct orientation of these wrinkled surface structures. The oscillation wavelength of the wrinkles was determined to $(4.5 \pm 0.2) \mu\text{m}$. The white artifacts crossing the center of the Fourier transformation are related to analyzing errors induced by the frame of the AFM image.

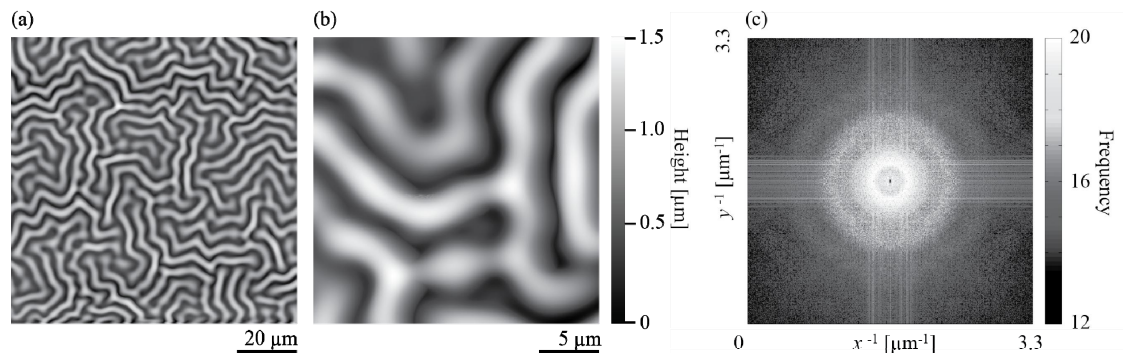


Figure 3. (a - b) Atomic microscope surface scans of a UV-treated DMS-V21 film are presented. The gray scale map represents the height of the wrinkled surface from zero (black) to $1.5 \mu\text{m}$ (white). (c) The corresponding Fourier transform of the AFM scan of part (a) exhibits the width of the wrinkles, given by the oscillation wavelength of the frequency.

An alternative technique to characterize the morphology accurately is the imaging by means of 3D laser scanning microscopy. To resolve this effect of surface wrinkling with respect to the thickness of PDMS films under UV-irradiation, a 200 nm-thin spin-coated, UV-treated DMS-V05 film is analyzed. Optical micrographs and cross sections parallel and perpendicular to the film thickness gradient are shown in Figure 4. Surface tension at the edge of the 3-inch wafer induces a thickness gradient while spin-coating of about $1 \mu\text{m}/\text{mm}$, see part (d) of Figure 4. A scratch at the left bottom side of the micrograph sets the baseline related to the Si-substrate surface and enables thickness determination of the PDMS film. The mean film thickness h_f is defined as the average over the height oscillation within the displayed

range, exemplary shown in part (b) of Figure 4. The cross section at a mean film thickness of $h_f = 200$ nm reveals an average wrinkle amplitude of about $h_w = (4.5 \pm 0.3)$ nm (Figure 4(c)). Contrary at a mean film thickness of $h_f = 1.65$ μ m an average wrinkle amplitude of $h_w = (0.71 \pm 0.08)$ μ m is detected (Figure 4(b)).

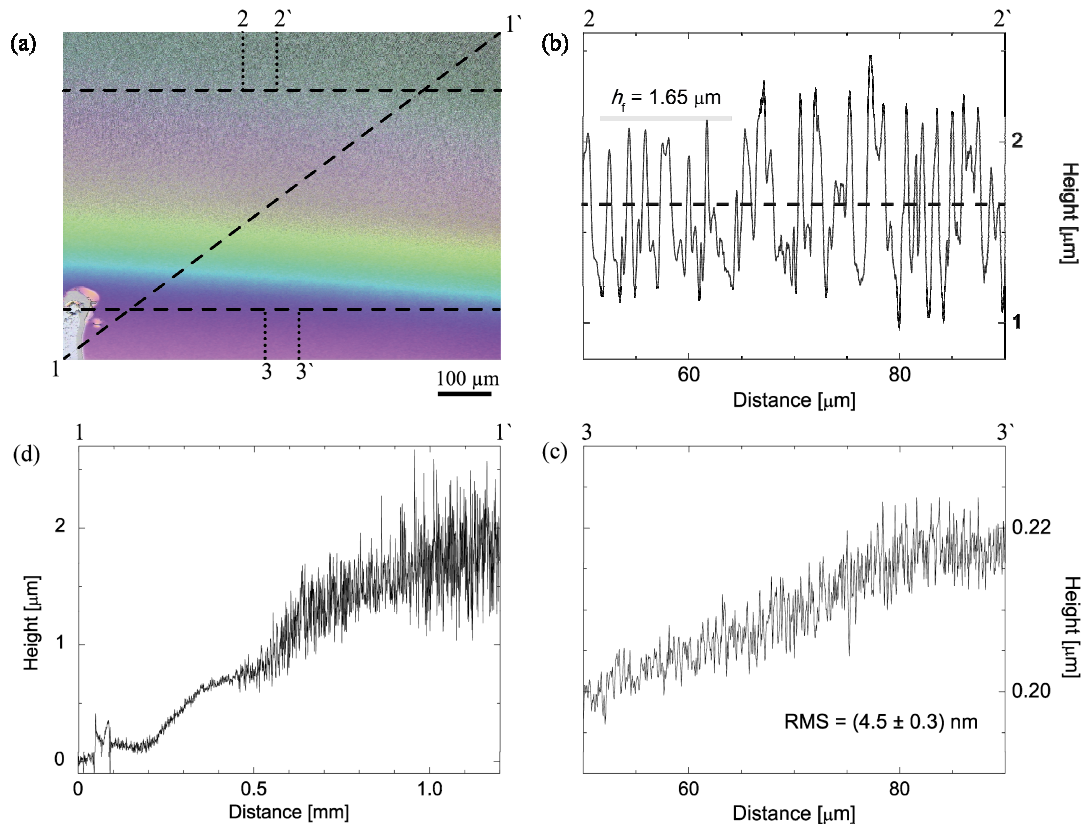


Figure 4. (a) Optical micrograph of a spin-coated, UV-treated DMS-V05 film exhibits the thickness gradient at the edge of the 2-inch wafer indicated by the color variations. The scratch at the bottom-left side sets the zero position of film thickness at the Si-substrate. (b-c) Cross-sections, captured at 150 times optical magnification, parallel to the edge of the wafer reveal increased surface roughness with increased film thickness. (d) The cross-section, captured at 50 times optical magnification, perpendicular to the wafer edge exhibits a film thickness gradient of about 1 μ m/mm and increasing wrinkle amplitudes with respect to the film thickness.

The extraction of average wrinkle amplitude h_w with respect to the UV-treated PDMS film thickness is presented in Figure 5. For film thickness below 500 nm stable average wrinkle amplitudes of (20 ± 10) nm are extracted. This constant wrinkle amplitude is attributed to the limited resolution at a 50 times optical magnification applied for the cross-section of panel (d) in Figure 4. For film thicknesses above 500 nm a constant increase of the wrinkle amplitude can be observed. A linear fit $y = (0.576 \pm 0.026)$ nm/mm \times $h_f - (299.8 \pm 29.8)$ nm describes the characteristic slope. The intersection of the linear function with the y -axis is found at (510 ± 30) nm, characterizing the onset of wrinkle formation.

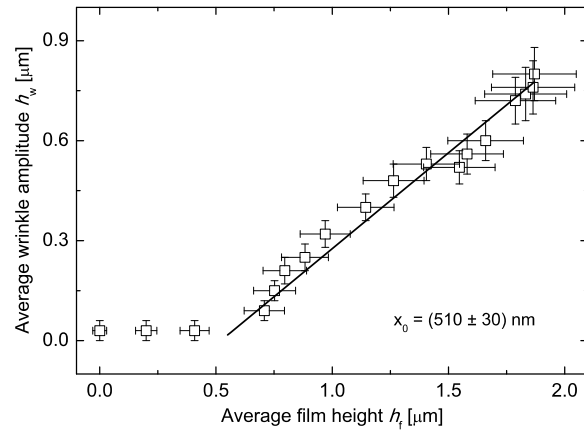


Figure 5. The extracted average wrinkle amplitude is presented with respect to the thickness of a UV-treated PDMS film. The resolution of a 50 times optical magnification limits the determination of the wrinkle amplitude for film heights below 500 nm. For film thicknesses above 500 nm a linear fit describes the increase of wrinkle amplitude with increasing film height.

3.3 Morphology of UV-treated PDMS coated with a 10 nm-thin Au-film

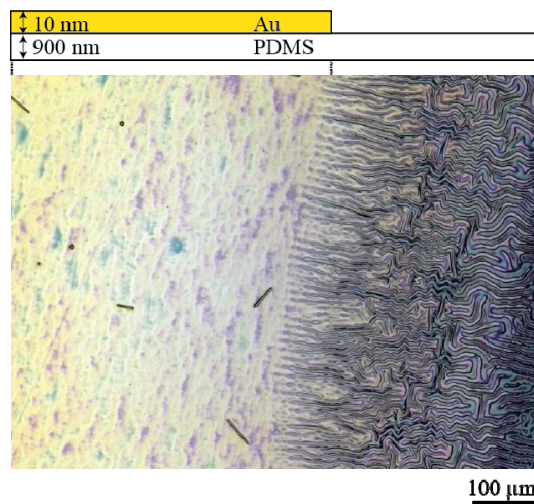


Figure 3. A 3D laser scanned micrograph with 50 times optical magnification presents the morphology of UV-treated, 900 nm-thin DMS-V05 film, partially covered with sputtered 10 nm-thin Au.

Surface characterization of a sputtered Au-electrode is presented in Figure 6. 3D laser microscopy with a 50 times optical magnification reveals the morphology of the UV-treated, 985 nm-thin DMS-V05 film partially covered with a 10 nm Au-layer. The sketch at the top of the photograph indicates the edge of the Au-mask applied within the sputtering vacuum chamber. Within the uncovered area of pure UV-treated PDMS the typical wrinkled surface with average amplitude of about 280 nm is observed. An associated mean surface roughness of (190 ± 10) nm is detected for a spanned area of $100 \times 100 \mu\text{m}^2$. The surface of Au-covered PDMS exhibits a flattened morphology with a mean surface roughness of (45 ± 7) nm within an area of same size. At the edge generated by the mask a thickness gradient of the

deposited Au-film can be observed. This effect occurs due to the unidirectional sputtering conditions within the sputter setup inducing an Au-shadow below the mask. Within this region a gradual increase of wrinkle amplitude with decreasing Au-thickness is detected.

4. DISCUSSION

Contrary to the studies on elastic properties of end-linked PDMS networks of Mark *et al.* [17], AFM nano-indentations revealed no correlation between elastic modulus and the utilized molecular weight of the UV-polymerized PDMS networks. An exponential decrease of elastic modulus with respect to indentation depth is found. We correlate this to the strong absorption of the UV-light in the PDMS surface near region. According to Lambert-Beer law the absorbance is logarithmically dependent on the penetration depth. The PDMS effective absorption coefficient of $3.27 \times 10^4 \text{ cm}^{-1}$ at a 248 nm irradiation wavelength [25] does result in an absorbance above 90 % at a penetration depth of about 270 nm. For irradiation depths above a few hundred nanometers fractional amounts of UV irradiation are transmitted. Thus, the radicalization and subsequently the speed of radicalization follow the irradiation profile, resulting in a high radicalization rate at the surface and decreasing rate with increased penetration depth. This concentrated absorbance of UV light located close to surface results in a highly cross-linked surface near region descending within the first few hundreds of nanometer to a bulk region with elastic modulus of $(87 \pm 7) \text{ kPa}$. The bulk elastic modulus is relatively low compared to that of PDMS micrometer-thick films reported in literature with a few MPa [18, 26, 27]. A surface near region has also been reported for heat-cured PDMS exhibiting an increased elastic modulus down to a thousand nanometers [26]. Nevertheless, this effect is contributed to an enriched cross-link density within the surface region. Contrary, we attribute the high elastic modulus of the UV-treated PDMS surface to a SiO_x -enriched layer ($1.5 < x < 2$) of a few nanometers as reported in literature [8]. At irradiation wavelengths below 190 nm methyl groups become sensitive to radicalization. C-H or even Si-C bonds are radicalized and methyl side groups are separated from the Si-O backbone of the PDMS chain [11, 20, 21]. Thus, the detected low bulk modulus of PDMS allows for the interpretation of a partially polymerized PDMS network underneath a silica-like surface.

The film morphology characterization has revealed wrinkled surface microstructures for all UV-cured PDMS films. We also correlate this to the inhomogeneous UV-irradiation density perpendicular to the film surface. Furthermore, the high absorption within the surface near region localizes the heating of PDMS film. Due to the different expansion coefficients of PDMS and silica a stress at the interface is induced. The stress-release after UV-treatment termination results in a wrinkled surface structure. Based on Genzer *et al.* the thickness of the silica-like surface layer can be calculated according to Equation 5 [28].

$$h = \frac{\lambda}{2\pi} \left[\frac{(1-\nu_f^2)E_s}{(1-\nu_s^2)E_f} \right]^{-1/3} \quad (5)$$

Exemplary AFM surface scans of the DMS-V21 1.2 μm -thin film show unidirectional distribution of wrinkles with a wavelength $\lambda = (4.5 \pm 0.2) \mu\text{m}$. With the elastic moduli $E_s = 87 \text{ kPa}$, $E_f = 36.7 \text{ GPa}$ and the Poisson's ratio $\nu_s = 0.5$, $\nu_f = 0.17$ of the PDMS substrate and the silica film, the thickness h of the silica-like film on the surface was determined to $(10.1 \pm 0.4) \text{ nm}$. The dependency of wrinkle amplitude with respect to the film thickness follows a linear behavior with a threshold at a film thickness of $(510 \pm 30) \text{ nm}$. This increase of wrinkle amplitude is related to the cross-linking density, which decreases with increasing thickness of the underlying PDMS film. The determined threshold of wrinkled microstructures, the oscillation wavelength as well as the thickness of the silica-like surface skin are dependent on the irradiation intensity.

Nevertheless, it has been found that wrinkled surface patterns enhance the stretch ability of electrode layers on soft substrates [29]. Thus, a sputtered 10 nm-thin Au-electrode on UV-treated DMS-V05 has been characterized by means of 3D laser scanning microscopy. On the Au-covered surface, no wrinkled surface microstructures are present. A decrease of mean surface roughness by a factor of 4.5 is found for a UV-treated DMS-V05 film coated with 10 nm Au compared to uncoated, UV-treated DMS-V05. We relate the vanishing of wrinkled surface structures to the plasma environment while the Au-film growth process. Similar to UV-light treatment, plasma-treatment induces high energy densities within the surface near region [30]. Heat-induced uniaxial stretching of the silica like surface promotes a smoothed surface after Au-film deposition.

5. CONCLUSIONS

We have demonstrated that UV-cured polydimethylsiloxane films exhibit a silica-like surface with thickness up to 10 nm and a soft bulk region with elastic modulus down to 87 kPa. Due to the limitations of spin coating, we expect that films with thicknesses of a few hundred nanometers to be only partially polymerized. Thus, the anticipated dependency of elastic modulus with respect to the molecular weight of the polymer was not detected. For detailed investigations, we propose MBD of PDMS to realize nanometer thin films. This technique would enable an in-situ UV-curing while the PDMS oligomers reach the substrate and thus a homogenous polymerization grade within the whole PDMS films.

From 3D laser microscopy scanning and atomic force microscopy characterizations we conclude that wrinkled surface microstructures on UV-cured PDMS films occur at a thickness threshold, which is dependent on the irradiation intensity and treatment time of the UV-light. With increasing PDMS film thickness the amplitude of these wrinkles increases in a linear fashion. Based on sputtered Au-deposition the wrinkled microstructures can be released. The resulting pre-stretched Au/PDMS sandwich structure would qualify for highly stretchable electronics [31]. Regarding the operation conditions for EAP-based artificial muscles, high strains with maintained conductivity are needed. Thus UV-induced wrinkled microstructures can be advantageous for potential stretchable contact layers for DEAs.

ACKNOWLEDGMENTS

The authors are grateful to Monica Schönenberger, Physics department, University of Basel, Switzerland, for the help and advice concerning the 3D laser microscopy measurements. The financial support of the Swiss nano-tera.ch initiative *SmartSphincter* and of the Swiss Nanoscience Institute (SNI) is gratefully acknowledged.

REFERENCES

- [1] A. K. Macmillan, A. E. Merrie, R. J. Marshall *et al.*, "The prevalence of fecal incontinence in community-dwelling adults: a systematic review of the literature," *Diseases of the Colon and Rectum*, 47(8), 1341-9 (2004).
- [2] J. Stoker, S. Halligan, and C. I. Bartram, "Pelvic floor imaging," *Radiology*, 218(3), 621-41 (2001).
- [3] B. Müller, H. Deyhle, S. Mushkolaj *et al.*, "The challenges in artificial muscle research to treat incontinence," *Swiss Medical Weekly*, 139, 591-595 (2009).
- [4] R. Pelrine, R. Kornbluh, Q. Pei *et al.*, "High-speed electrically actuated elastomers with strain greater than 100%," *Science*, 287(5454), 836-839 (2000).
- [5] E. Fattorini, T. Brusa, C. Gingert *et al.*, "Artificial Muscle Devices: Innovations and Prospects for Fecal Incontinence Treatment," *Annals of Biomedical Engineering*, 1-15 (2016).
- [6] Y. Bar-Cohen, [Application of Dielectric EAP Actuators] SPIE Press, Bellingham, 16 (2004).
- [7] F. Carpi, D. Rossi, R. Kornbluh *et al.*, [Dielectric elastomers as high-performance electroactive polymers] Elsevier Ltd., Hungary, 2 (2008).
- [8] A. E. Özçam, K. Efimenko, and J. Genzer, "Effect of ultraviolet/ozone treatment on the surface and bulk properties of poly(dimethyl siloxane) and poly(vinylmethyl siloxane) networks," *Polymer*, 55(14), 3107-3119 (2014).
- [9] F. M. Weiss, T. Töpfer, B. Osmani *et al.*, *Adv. Elec. Mater.*, (in press), (2016).
- [10] F. M. Weiss, T. Töpfer, B. Osmani *et al.*, "Thin film formation and morphology of electro-sprayed polydimethylsiloxane," *Langmuir*, in press, (2016).
- [11] T. Töpfer, F. M. Weiss, B. Osmani *et al.*, "Siloxane-based thin films for biomimetic low-voltage dielectric actuators," *Sensors and Actuators A: Physical*, 233, 32-41 (2015).
- [12] H. F. Mark, [Encyclopedia of Polymer Science and Technology] Wiley & Sons: New York, (2014).
- [13] S. J. C. J. A. Semlyen, [Siloxane Polymers] Prentice Hall PTR, (1993).
- [14] T. Töpfer, S. Lörcher, F. M. Weiss *et al.*, "Tailoring the mass distribution and functional group density of dimethylsiloxane-based films by thermal evaporation," *Applied Physics Letters*, submitted, (2016).
- [15] N. Tomer, F. Delor-Jestin, L. Frezet *et al.*, "Oxidation, chain scission and cross-linking studies of polysiloxanes upon ageings," *Open Journal of Organic Polymer Materials*, 2 (2), 13-22 (2012).
- [16] U. Müller, H. J. Timpe, K. G. Häusler *et al.*, "Lichtinitiierte Polymer- und Polymerisationsreaktionen. 36. Mitt.: Photovernetzung vinylgruppenhaltiger Poly(dimethylsiloxane)," *Acta Polymerica*, 41 (1), 54-59 (1990).

- [17] J. E. Mark, and J. L. Sullivan, "Model networks of end-linked polydimethylsiloxane chains. I. Comparisons between experimental and theoretical values of the elastic modulus and the equilibrium degree of swelling," *The Journal of Chemical Physics*, 66 (3), 1006-1011 (1977).
- [18] F. Carrillo, S. Gupta, M. Balooch *et al.*, "Nanoindentation of polydimethylsiloxane elastomers: Effect of crosslinking, work of adhesion, and fluid environment on elastic modulus," *Journal of Materials Research*, 20(10), 2820-2830 (2005).
- [19] T. Töpper, B. Osmani, F. M. Weiss *et al.*, "Viscoelastic properties of polydimethylsiloxane studied by cantilever bending," *European Cells and Materials*, 30, 68 (2015).
- [20] L. Prager, L. Wennrich, R. Heller *et al.*, "Vacuum-UV irradiation-based formation of methyl-Si-O-Si networks from Poly(1,1-dimethylsilazane-co-1-methylsilazane)," *Chemistry – A European Journal*, 15(3), 675-683 (2009).
- [21] C. Dölle, M. Pappmeyer, M. Ott *et al.*, "Gradual photochemical-induced conversion of liquid polydimethylsiloxane layers to carbon containing silica coatings by VUV irradiation at 172 nm," *Langmuir*, 25(12), 7129-7134 (2009).
- [22] M.-S. Lee, K. Lee, S.-Y. Kim *et al.*, "High-performance, transparent, and stretchable electrodes using graphene-metal nanowire hybrid structures," *Nano Letters*, 13(6), 2814-2821 (2013).
- [23] T. Cheng, Y. Zhang, W.-Y. Lai *et al.*, "Stretchable thin-film electrodes for flexible electronics with high deformability and stretchability," *Advanced Materials*, 27(22), 3349-3376 (2015).
- [24] T. Töpper, B. Osmani, F. M. Weiss *et al.*, "Strain-dependent characterization of electrode and polymer network of electrically activated polymer actuators," *Proc. SPIE* 9430, 94300B (2015).
- [25] V.-M. Graubner, O. Nuyken, T. Lippert *et al.*, "Local chemical transformations in poly(dimethylsiloxane) by irradiation with 248 and 266 nm," *Applied Surface Science*, 252(13), 4781-4785 (2006).
- [26] C. A. Charitidis, "Nanoscale deformation and nanomechanical properties of polydimethylsiloxane (PDMS)," *Industrial & Engineering Chemistry Research*, 50(2), 565-570 (2011).
- [27] Z. Wang, A. A. Volinsky, and N. D. Gallant, "Crosslinking effect on polydimethylsiloxane elastic modulus measured by custom-built compression instrument," *Journal of Applied Polymer Science*, 131(22), (2014).
- [28] J. Genzer, and J. Groenewold, "Soft matter with hard skin: From skin wrinkles to templating and material characterization," *Soft Matter*, 2(4), 310-323 (2006).
- [29] J. Tang, H. Guo, M. Zhao *et al.*, "Highly stretchable electrodes on wrinkled polydimethylsiloxane substrates," *Scientific Reports*, 5, 16527 (2015).
- [30] M.-W. Moon, and A. Vaziri, "Surface modification of polymers using a multi-step plasma treatment," *Scripta Materialia*, 60(1), 44-47 (2009).
- [31] O. K. Oyewole, D. Yu, J. Du *et al.*, "Micro-wrinkling and delamination-induced buckling of stretchable electronic structures," *Journal of Applied Physics*, 117(23), 235501 (2015).

2.3 Strain-dependent characterization of electrode and polymer network of electrically activated polymer actuators

Four point measurements on sputtered Au on polydimethylsiloxane reveal a step-like increase in bulk resistivity for Au-film thicknesses below 10 nm.

Improved conductivity for 10 nm-thin Au films compared to 30 nm-thin Au films with areal strain applied.

10 nm-thin Au films tolerate areal strains above 20 % with maintained conductivity.

The cantilever bending setup qualifies to determine the elastic properties and cross-linking density of polydimethylsiloxane films.

Published in Proceedings of SPIE 2015

Strain-dependent characterization of electrode and polymer network of electrically activated polymer actuators

Tino Töpper^a, Bekim Osmani^a, Florian M. Weiss^{a,b}, Carla Winterhalter^a, Fabian Wohlfender^a,
Vanessa Leung^a, and Bert Müller^{*a}

^aBiomaterials Science Center, University of Basel, c/o University Hospital, 4031 Basel, Switzerland;

^bSwiss Federal Laboratories for Materials Science and Technology, Überlandstrasse 129, 8600 Dübendorf, Switzerland

ABSTRACT

Fecal incontinence describes the involuntary loss of bowel content and affects about 45 % of retirement home residents and overall more than 12 % of the adult population. Artificial sphincter implants for treating incontinence are currently based on mechanical systems with failure rates resulting in revision after three to five years. To overcome this drawback, artificial muscle sphincters based on bio-mimetic electro-active polymer (EAP) actuators are under development. Such implants require polymer films that are nanometer-thin, allowing actuation below 24 V, and electrodes that are stretchable, remaining conductive at strains of about 10 %. Strain-dependent resistivity measurements reveal an enhanced conductivity of 10 nm compared to 30 nm sputtered Au on silicone for strains higher than 5 %. Thus, strain-dependent morphology characterization with optical microscopy and atomic force microscopy could demonstrate these phenomena. Cantilever bending measurements are utilized to determine elastic/viscoelastic properties of the EAP films as well as their long-term actuation behavior. Controlling these properties enables the adjustment of growth parameters of nanometer-thin EAP actuators.

Keywords: Compliant electrode, ultra-thin gold-film resistivity, four-point conductivity measurement, cantilever bending, asymmetric planar electro active polymer, polyetheretherketone, polydimethylsiloxane, viscoelasticity

1. INTRODUCTION

The changing demographics of modern society have resulted in the increasing prevalence of socially and economically significant, age-related diseases. Among them is a loss of control of the defecation process, also known as fecal incontinence (FI) [1]. FI encompasses all forms of involuntary loss of bowel content, including flatus, mucus, liquid and solid feces. In adults, the overall prevalence of FI is between 11 and 15 % [1] and increases with age [2]. Approximately one third of individuals in retirement homes or similar institutions are affected [2]. FI prevalence in retirement homes in the U.S. is about 45 % [3, 4], a figure which agrees with those found in European cross-sectional studies [5]. Individuals with FI experience detrimental effects, which include the exclusion from social life, isolation and stigmatization [1], and economic impact [2].

Artificial sphincter implants offers a possible solution to treat severe fecal incontinence. Yet, it remains a significant challenge for the researchers to build artificial muscles to reproduce the capabilities of the natural sphincter [6]. Currently available implants show long-term re-operation rates of 95 % and definitive ex-plantation rates of 40 %. The high risk of failure excludes these implants from everyday surgery. Electrically activated polymer (EAP) actuators can potentially fill the pressing need for a bio-mimetic implant [6]. Technical advantages of EAPs include their versatility, response time, forces, and energy consumption [7]. Biomimetic artificial sphincters based on EAPs will support a rapidly adaptive pressure response, comparable to the natural feedback mechanism of the human body.

An artificial sphincter device might be actuated by an EAP-based sandwiched nanostructure and controlled by an implantable battery-powered microcomputer re-charged using the power of the human body. The innovation lies in the avoidance of constant compression and therefore erosion of the tissue. For example, a series of shutter modules work over a pre-defined length of the digestive tube or the urethra and should open and close in a certain time sequence.

*bert.mueller@unibas.ch; phone 41 61 265 9660; fax 41 61 265 9699; www.bmc.unibas.ch

Electroactive Polymer Actuators and Devices (EAPAD) 2015, edited by Yoseph Bar-Cohen, Proc. of SPIE
Vol. 9430, 94300B · © 2015 SPIE · CCC code: 0277-786X/15/\$18 · doi: 10.1117/12.2084595

Proc. of SPIE Vol. 9430 94300B-1

To employ EAP structures as active and powered implants, voltages should not exceed the medically acceptable range of 24 V. Multi-layer stacks allow the actuation of multiple low-voltage dielectric EAP structures with a thickness in the nanometer regime to be harnessed in parallel. Such stacking results in an effective actuation comparable to that of currently available high-voltage EAP structures with a thickness in the micrometer range. Yet, the impact of the Young's modulus of the metal on the effective modulus of the entire EAP structure is pronounced in multi-stack actuators, even if the electrodes are much thinner than the polymer layer. Compliant electrodes that do not dominate the stiffness of the entire structure have yet to be clearly identified, although several potential candidates exist. Bi-layer systems of soft polymer bulk material and rigid thin-layered coatings have been studied for applications in packaging and microelectronics. It has thus been found, for example, that ultra-thin noble metal films on polymers including polydimethylsiloxane (PDMS) give rise to strains well above 10 % [8].

For the optimization of polymer films as well as the ultra-thin metal layer electrodes in dielectric electro active actuators (DEA)-microstructures, several measurement techniques must be employed. In our case, a combination of two techniques allows the electrical and mechanical properties of the actuators to be quantified. The electrical conductivity of the electrodes is essential for the response time of the actuator and must be characterized for the optimized performance of the engineered artificial muscle. Four-point measurement is a well-established technique that allows the measurement of the electrode resistivity [9-12].

In addition, mechanical properties such as elasticity and viscoelasticity are crucial for the success of an EAP actuator. Cantilever-bending measurements are based on an established technique used in a broad range of applications, for example atomic force microscopy [13-18]. We have previously demonstrated that cantilever bending is a method well suited to evaluate EAP microstructures with high angular resolution at low voltages [19, 20]. Finally, qualitative knowledge of the morphological details can support the quantitative results obtained by the four-point conductivity and cantilever-bending measurements. The morphology of the substrate is characterized through the combination of optical microscopy and atomic force microscopy.

2. EXPERIMENTAL

2.1 Cantilever preparation

The asymmetric EAP-microstructures evaluated were built on polyetheretherketone (PEEK) substrates (APTIV 2000, Victrex, Lancashire, UK) with a thickness of 25 μm or the n-doped Si-wafers with a thickness of (20 ± 10) μm from Wafer World Inc., West Palm Beach FL, USA. The PEEK films were cut to the dimensions of a 3-inch wafer. The substrates were cleaned with acetone (Merck KGaA, Darmstadt, Germany). Subsequently, gold (Lesker, East Sussex, UK) was magnetron-sputtered on the rougher side of the PEEK film, mean surface roughness about 0.8 μm , or on the polished side of the Si wafer under vacuum conditions at room temperature. The related sputtering conditions in the Balzers Union SCD 040 system (Balzers, Lichtenstein) corresponded to 0.05 mbar Ar-atmosphere (Carbagas AG, Gumligen, Switzerland) and a constant working current of 30 mA. The thickness of the Au electrodes ranged from 7 to 30 nm, determined by a calibration curve plotting time versus thickness measured using a quartz crystal microbalance (QSG 301, Balzers, Balzers, Lichtenstein). In the next step, the Au-covered substrates were spin-coated using PDMS (Elastosil 745 A/B, Wacker Chemie AG, Munich, Germany) mixed in a volume ratio 1:1 (component A and B) or Sylgard 184 (DowCorning, Wiesbaden, Germany) with a ratio of 10:1 of elastomer to curing agent with rotation speeds to obtain layer thicknesses ranging from 2 to 5 μm . Before crosslinking the PDMS films at a temperature of 120 $^{\circ}\text{C}$ for a duration of 30 to 120 minutes, the coated substrates were partly submerged into ethyl acetate (Fisher Scientific, Reinach, Switzerland) to dissolve and wash off the PDMS in order to become access to the lower electrode as described previously [21]. After PDMS-crosslinking, a mask covered some parts of the structure to obtain two electrodes with a step-like profile as displayed in Figure 5 of Ref. [22]. The uncovered PDMS surfaces were then sputter-coated with Au under the comparable conditions as the first electrode.

2.2 Bending measurement

In principle, the operation mode of electrically activated polymer (EAP) structures is based on the COULOMB attraction between positively and negatively charged electrodes embedding a dielectric elastomer such as silicone or acrylic based polymers. If a voltage is applied the two electrodes become oppositely charged and due to the attraction force squeeze the elastomer layer in z -direction, whereas the area increases because the volume is assumed to remain constant. Thus, an voltage-dependent expansion in x - and y -directions can be observed.

In case of an asymmetric planar structure such as a cantilever-shaped structure the applied strain will induce a torque, which results in a bending of the structure if one end is fixed on a mount while the other one freely moves [20]. To isolate the EAP-microstructure electrically, a Teflon mount was chosen. The voltage was applied via wires coated with drops of fluid metal (Coollaboratory Liquid Pro, Coollaboratory, Magdeburg, Germany). The bending can be recorded by a position sensitive detector (PSD), which detects the displacement of the reflected laser beam as described previously [20, 21]. To avoid disturbance of this sensitive displacement detection by external acoustic, motional, and thermal influences the entire setup is sealed within an aluminum box [22].

2.3 Four-point conductance measurement on soft substrates

To quantify the sheet resistance R_s of the conducting electrode layer we used the well-established four-point method, schematically shown in part (a) of Figure 1 [10, 11]. In contrast to two-terminal sensing the advantage of four-terminal sensing is that the resistances of wires, contacts and the internal resistance of ampere meter and voltage source will not influence the result, since the current does not circulate through the electrodes returning the voltage difference [11]. Applying current I through two point-like outer contacts on an infinite plane gives rise to an electrostatic potential $\phi(r)$. If this potential is measured at the two inner contacts and the four contacts are aligned equally spaced on a straight line, the resulting voltage difference can be written according to Ref. [23]:

$$U = \phi(r_1) - \phi(r_2) = \frac{\ln(2)}{\pi} R_s I \quad (1)$$

Since the sample is finite and the current- and voltage-connecting tips are not infinitesimally small, geometric effects must be considered [10]. Therefore, the Hall-bar symmetry (see scheme part (a) of Figure 1) was applied to determine the dependence between resistance and electrode thickness of Au on PDMS. The voltage drop is measured at two contacts not lying in the current flow. Therefore, effects due to tip sizes are negligible. The resistance of a Hall bar of length L and width W is obtained by

$$R_s = \frac{U W}{I L} \quad (2)$$

To determine the strain-dependent resistance, a circularly shaped Au layer with a diameter of 37 mm was deposited on PDMS, which was spin-coated on a VHB F9460PC film (3M, St. Paul, USA) and subsequently mounted on a translation stages to be stretched. The distance s between the tips was set to 5 mm. Correction factors are available to compensate for the round shape of the layer [12]. If the four-point probe is centered and the tips are equally spaced with distance s , the voltage drop on a circularly shaped sample with diameter d is:

$$U = \frac{I R_s}{\pi} \left[\ln(2) + \ln \left(\frac{\left(\frac{d}{s}\right)^2 + 3}{\left(\frac{d}{s}\right)^2 - 3} \right) \right] \quad (3)$$

The setup did consist of four semi-spherical probe tips (SPA-3J, Everett Charles Technologies, Distriect) mounted on micro positioners (Signatone, aps Solutions GmbH, Munich, Germany) to place the measurement tips on the specimen individually. A non-destructible contact between tip and specimen was realized by adding a liquid metal drop onto the tip (Coollaboratory Liquid Pro, Coollaboratory, Magdeburg, Germany). To apply current and determine the voltage drop, a commercially available source meter (Keithley 2401) and a multimeter (Agilent 34461A Truevolt) were employed. For the measurements a constant current of 10 mA was chosen. The variation of voltage was detected.

2.4 Imaging of EAP-electrodes

The Au surface was imaged with an optical light microscope (Stemi DV4 SPOT, Carl Zeiss AG, Feldbach, Switzerland) using an optical magnification of 50. For higher spatial resolution an atomic force microscope (AFM), FlexAFM ARTIDIS system, Nanosurf AG, Liestal, Switzerland, was applied. Here, areas of $97.5 \mu\text{m} \times 97.5 \mu\text{m}$ (512×512 points) were recorded in tapping mode with a Tap150Al-G tip (Budget Sensors, Innovative Solutions Bulgaria Ltd., Sofia, Bulgaria). For visualization purposes mean plane subtraction was applied using the Gwyddian software (Department of Nanometrology, Czech Metrology Institute, Brno, Czech Republic).

3. RESULTS

3.1 Thickness- and strain-dependent resistivity of nanometer-thin Au electrodes on PDMS

Figure 1 represents experimental data of the four-point measurements for Au on PDMS. Part (b) includes the dependence of the bulk resistivity to the layer thickness determined within the Hall-bar symmetry, as sketched in part (a). The relation between measured resistance R_s , according to Equation 2, and the bulk resistivity ρ is simply the product of resistance and electrode thickness d [10].

$$\rho = R_s d \quad (4)$$

For Au thicknesses larger than 14.0 nm a constant bulk resistivity of $(1.4 \pm 0.2) \cdot 10^{-7} \Omega\text{m}$ was observed. Although the resistance increases from (6.7 ± 0.7) via (7.5 ± 0.8) to $(10.4 \pm 1.1) \Omega$ for 21.0, 17.5 and 14.0 nm, respectively, their product stays constant. A further reduction of the Au layer thickness, however, leads to a larger increase of their resistance, i.e. (22 ± 2) and $(103 \pm 11) \Omega$ for 10.5 and 7.0 nm. Additionally, a remarkable increase of the bulk resistivity to (2.31 ± 0.22) and $(7.21 \pm 7.80) \cdot 10^{-7} \Omega\text{m}$ is obtained.

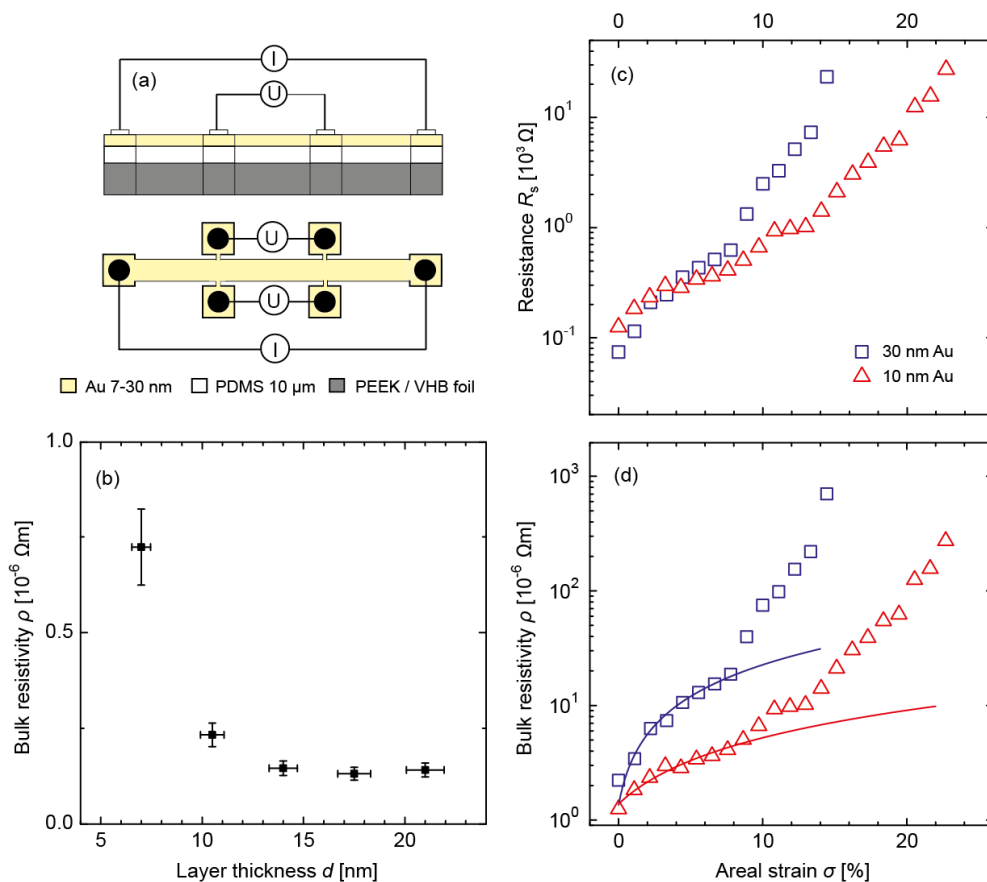


Figure 1. (a - b) The four-point resistance measurements of sputtered Au layers on PDMS are shown. The Hall-bar symmetry was chosen to exclude the influence of the contact resistance through the tips. The bulk resistivity ρ is comparable to the literature values of $0.2 \times 10^{-6} \Omega\text{m}$ for stress-free gold layers on PET [24] if no stress is applied. (c - d) The strain dependence of resistance R_s and bulk resistivity ρ was determined with a four-point measurement on a 60 mm \times 60 mm VHB film for 30 and 10 nm-thin Au films on PDMS. A maximal areal strain of up to 23 % in one lateral direction of the multilayer stack was applied. The fits illustrate the linear behavior of the bulk resistivity for areal strains up to 8 %.

Parts (c) and (d) of Figure 1 present strain-dependent resistance and resistivity data of 10 and 30 nm-thin Au films on PDMS. An in-line setup of four tips each 5 mm apart was fixed, whereas the sample mounted on a VHB-film was stretched. For this setup, the resistance was calculated according to Equation 3. In a relaxed state a 1.5 times lower resistance for 30 compared to 10 nm-thin Au layer was detected. Both, the 10 and 30 nm-thin Au layers exhibit a bulk resistivity, which is at least one order of magnitude higher than for thicker Au layers on PDMS deposited on PEEK. This behavior might be due to the flexibility and related morphology changes before the controlled areal strain could be applied.

When a lateral strain is applied to this multilayer stack a rise of resistance is monitored. Here, the slope for the 30 nm-thin layers is larger than for the 10 nm-thin layers on PDMS. At an areal strain above 5 % the 30 nm-thin Au layer exhibits a higher resistance than the 10 nm-thin Au layer on strained PDMS. The translation of resistance into bulk resistivity according to Equation 4 reveals a linear slope for the resistivity with increasing strain of up to 8 %. For the thicker Au film this slope was found to be 5.6 times higher than for the thinner one, cp. (2.13 ± 0.09) vs. $(0.38 \pm 0.03) 10^{-6} \Omega\text{m}$. At 13 % areal strain the 30 nm-thin Au layer shows a two orders of magnitude higher resistivity with respect to the 10 nm-thin Au layer.

One might expect that the changes in the conductance relate to the surface morphology. Therefore, 20 % areal strain was applied to the 10 and 30 nm-thin Au films on PDMS and optical micrographs, as shown in Figure 2, captured. The strain was applied in horizontal direction of the image orientation. The images with selected magnifications illustrate the relaxation behavior of the EAP-structures under strain.

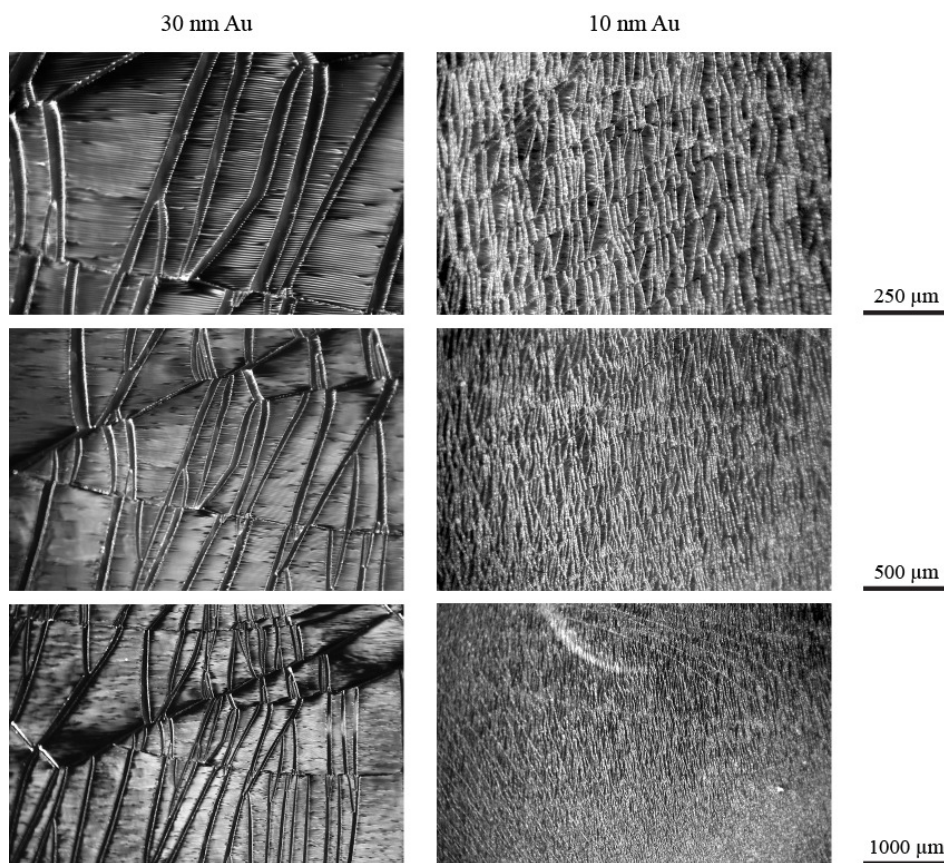


Figure 2. Optical micrographs of 30 nm (left side) and 10 nm (right side) thin Au-layers sputtered on PDMS on top of stretched VHB-films are shown. Horizontally to the images shown, 20 % areal strain was applied.

The 30 nm-thin Au layer forms islands of millimeter size. Cracks of up to 30 μm in horizontal direction occur. At the same strain level, the 10 nm-thin Au shows smaller islands and cracks with a width of only a very few micrometers. The images with lowest magnification in Figure 2 reveal the average crack densities, i.e. 4 and 30 mm^{-1} for the thicker and thinner Au-layers, respectively.

The AFM images represented in Figure 3 give a more detailed insight into the surface morphology of the Au-layers. In the relaxed state, the surfaces appear smooth. The features up to 60 nm high are attributed to dust particles common if the layers are prepared under ambient conditions. After the application of 20 % areal strain one also recognizes the five to ten micrometers wide cracks on the 10 nm-thin Au layer. The AFM data, however, also show horizontally orientated wrinkles with the height of 1.1 and 2.2 μm for 10 and 30 nm-thin Au-layers, respectively. This microstructure is probably a result of the shrinking of the VHB film in vertical direction to compensate for the stretching in horizontal direction. For thicker Au-layers the amplitude of the wrinkles is not only two times larger but also their width of approximately 9.0 μm is significantly larger with respect to the value found for the 10 nm-thin Au-layers, i.e. 2.3 μm .

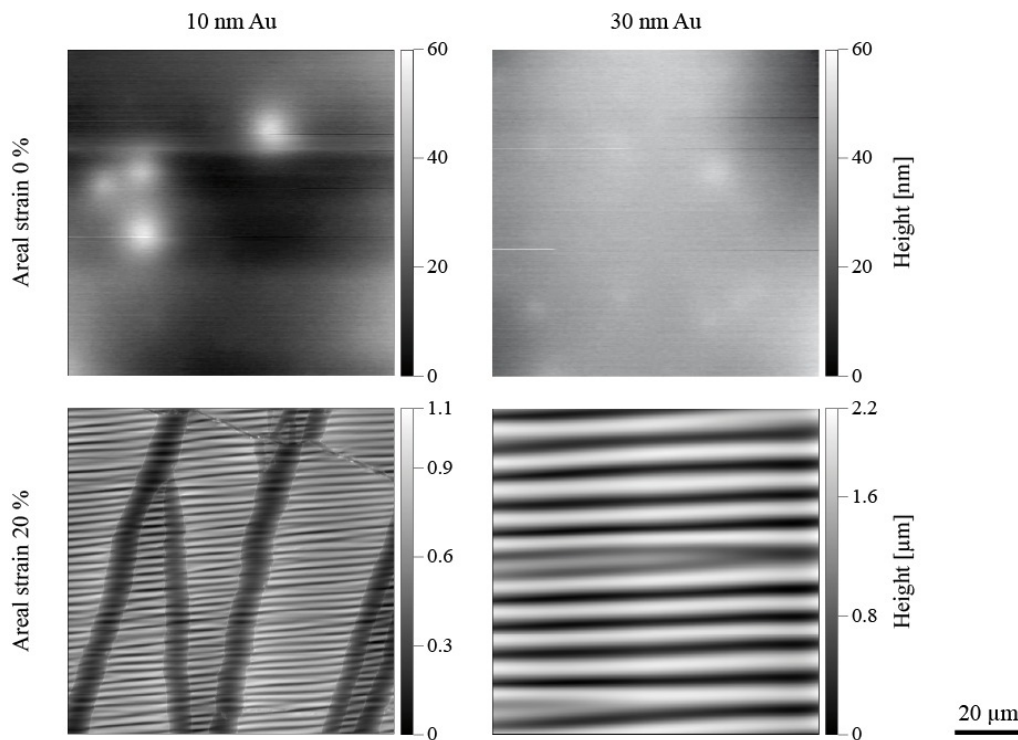


Figure 3. The AFM images of 30 and 10 nm-thin Au-layers sputtered on PDMS demonstrate the effect of applying 20 % areal strain in horizontal direction to the image. One finds periodically arranged wrinkles of micrometer size.

3.2 Elastic properties of EAPs determined by cantilever bending

For the actuation analysis of EAP microstructures the cantilever bending method is a powerful tool to access the elastic properties. For example, one can study the actuation as the function of polymerization time. The curvature of the cantilever depends on the applied voltage, as for example shown in Figure 4. EAP actuators based on Elastosil A/B, embedded between 15 nm-thin Au electrodes, and deposited on 25 μm -thick PEEK films were heat cured for 1.8×10^3 s (0.5 h) and 7.2×10^3 s (2 h), respectively. Subsequently, an actuation voltage of 200 and 400 V was applied for a period of 80 s. The actuator cured for the shorter period of time (0.5 h) showed more than doubled deflection compared to the other actuator. Nevertheless, its actuation dropped within a period of 10 to 20 s to a lower but stable value. This relaxation process can be characterized by the time constant τ , which was determined by an exponential fit function to $\tau = (2.93 \pm 0.03)$ s, see Figure 4. For actuator heat-cured for two hours no such relaxation behavior was observed.

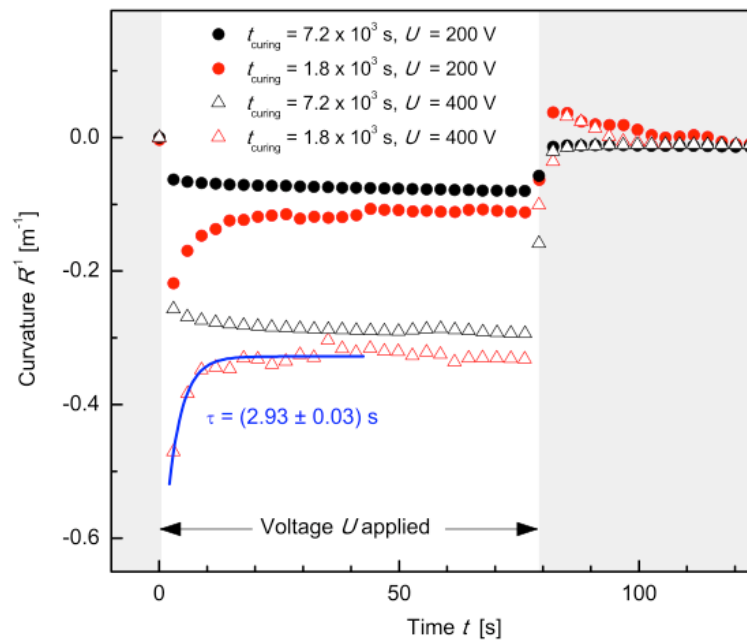


Figure 4. The actuation behavior of EAP-microstructures on PEEK cantilevers is presented for actuation voltages of 200 and 400 V and compared for curing times of 1.8 and 7.2 10³ s (0.5 and 2.0 h), respectively. Heat curing of the Elastosil A/B layers at a temperature of 120 °C seems to be incomplete, if the curing time is restricted to half an hour. Nevertheless, the actuation is larger for the incompletely cured layers than for the fully polymerized elastomer.

It is worth mentioning that a certain period of time, which is about 10 s, is required to observe the maximal curvature. A similar phenomenon is found, when the voltage is switched off, cp. Figure 4.

To gain a more detailed insight to the actuation as the function of the curing time, the period for curing was set to 1.2, 1.8, 2.4, 3.6 10³ s. The corresponding time constants for relaxation were derived and are summarized in Table 1. This table also contains the ratios between the maximal bending and the one measured after equilibration. As expected, the relative actuation relaxation values decrease and the time constants increase as the curing time is extended.

Table 1. Relaxation parameters obtained from an asymmetric EAP-structures based on Elastosil A/B, see section 2.2, heat cured at a temperature of 120 °C for a period between 1.2 and 3.6 10³ s, i.e. 20 to 60 minutes. The presented relaxation characteristics were determined at an actuation voltage of 400 V, which corresponds to a Maxwell strain of 22 %.

Time of heat curing [10 ³ s]	τ [s]	Actuation relaxation [%]
1.2	0.32 ± 0.01	93 ± 1
1.8	2.9 ± 0.6	43 ± 2
2.4	14 ± 2.8	36 ± 4
3.6	60 ± 24	14 ± 2

3.3 Actuation characteristics determined by multi-cycle cantilever bending

The cantilever bending induced by EAP-actuators on top of a polymeric substrate including PEEK has been successfully applied to characterize the electrode properties [21]. Nevertheless, reasonable reliability tests over a longer period of time and a related number of cycles require stability of the experimental setup and the EAP-structure. Therefore, the actuation characteristics of EAP-structures consisting of 2 μm -thin PDMS (Sylgard®184 silicone elastomer, Dow Corning Corporation, Midland MI, USA) with 20 nm-thin sputtered Au electrodes on single-crystal 20 μm -thick Si substrates were measured. The curvature of the cantilever directly yields the actuation amplitude. Figure 5 displays the results as a function on the cycle number and the time (logarithmic scale). For an applied voltage of 32 V the actuation is initially increasing until the electrodes of the EAP-structures are fully charged. During the actuation polymer and electrodes develop a characteristic defect structure associated with changes in the actuation amplitude. After about 300 actuation cycles the changes become negligible. Applying a three times higher actuation voltage, i.e. 96 V, one also observes this behavior with a steady state level reached at 1,600 cycles.

Printing the time scale in logarithmic fashion, as given in the right diagram of Figure 5 reveals that during the first 10 s charging periods the used 96 V pulses are too short to fully load the capacity of the EAP-structure.

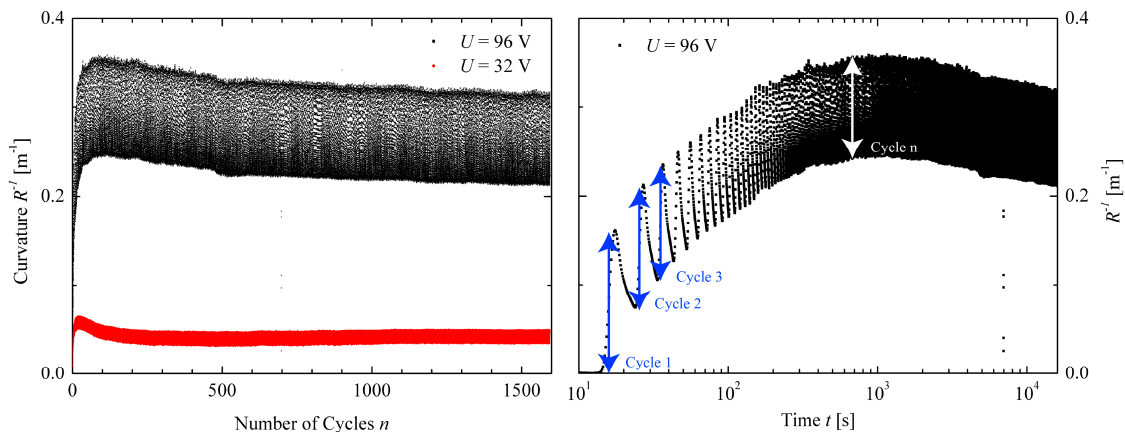


Figure 5. Bending of a 20 μm -thin Si cantilever induced by a 2 μm -thin EAP-structure on top. Applying 1,600 pulses of 32 and 96 V with a frequency of 0.1 Hz, the curvature changes in a characteristic manner. The charging and discharging of the EAP-structure follows the conventional behavior of the resistance-capacitance circuit. Thus, the EAP-actuator is fully charged after a number of cycles, given by the pulse frequency.

4. DISCUSSION

The four-point conductivity measurements on nanometer-thin Au films revealed the expected increase of sheet resistance with decreasing layer thickness. Nevertheless, the related bulk resistivity was found to stay constant for a film thickness down to 14 nm, implying that Au films on polymeric substrates with thicknesses above that level keep their bulk-like conductivity behavior. For a smaller thickness, a remarkable increase of the bulk resistivity was detected, concluding that a continuity of the Au film cannot be assumed [24]. The findings correspond to the measured bulk resistivity of 50 nm-thin Au on PDMS with $3.5 \cdot 10^{-7} \Omega\text{m}$ [9] and $2 \cdot 10^{-7} \Omega\text{m}$ for 21 nm-thin Au on polyethylene terephthalate (PET) [24]. The transition thickness, at which the step-like increase of bulk resistivity occurs, was found between 5 and 7 nm for Au on PET [25]. The difference to the data in the present communication, i.e. between 10.5 and 14.0 nm for Au on PDMS, is probably a result of the surface morphology and defect structure of the Au film, which depend on the substrate film and the deposition parameters. It should be noted that the layer resistivity above the transition thickness is about one order of magnitude higher than that of bulk gold, i.e. $2 \cdot 10^{-8} \Omega\text{m}$ [26]. The low thickness values, related to less compact arrangements of the Au atoms, justify the difference derived.

In the range up to 8 % areal strain the strain-dependent resistivity measurements revealed a significantly greater linear increase for 30 nm-thin Au film than for the 10 nm-thin one. Optical micrographs have evidentially shown that for the thicker Au film larger cracks occur and thus hinder the current flow in the direction of applied strain. At 20 % areal

strain the thinner Au film exhibited a crack density of 30 mm^{-1} , more than a factor of seven larger than for the three times thicker Au film. It becomes therefore clear that the more compact and bulk-like Au film is the less adaptable to the substrate under strain. The larger crack width between the islands of the thicker Au film results in the steeper slope of the resistivity as the function of the applied strain. This behavior is disadvantageous for the response time of the actuator, which is directly proportional to the resistance of the electrodes. Furthermore, it implies that during actuation micrometer-size regions form, in which no electrical charge can be deposited, thus resulting in reduced actuation efficiency. The results of Graz et al. [9] revealed that for a 50 nm-thin Au films grown on 5 nm-thin Cr the increase was found to be linear up to 20 % strain with a slope of $0.65 \cdot 10^{-6} \Omega\text{m}/\%$. This value is three times smaller than the one for the 30 nm-thin Au layer grown on PDMS.

The cantilever bending measurements allow for the characterization of the actuation response of the electrically activated polymer layer. Exemplarily, we investigated dielectric actuators based on heat-cured Elastosil A/B. The polymer film shows a curing-time dependent compliance under strain. Increasing the curing time of the polymer layer the relaxation process of the actuation decreases. Simultaneously, the relaxation is slowed down, which we quantified by means of a time constant. As the completely cross-linked PDMS layers are known to be incompressible, we can attribute the observed change of actuation response to the degree of cross-linking within the polymer network. Consequently, the cantilever bending method enables us to assess the viscoelastic response of polymer thin films to the applied MAXWELL strain. It represents a promising alternative to the established characterization of thermal wrinkling of confined polymer films [27] in order to determine the elastic and viscoelastic properties of micrometer-thin films.

Furthermore, we performed multiple-actuation cycling of the dielectric structures on single-crystalline Si cantilever substrates. The bending of the cantilever was reliably recorded for several hundred charging cycles with a frequency of 0.1 Hz. One observes, however, temporal changes in amplitude and characteristic offsets, which depend on the applied voltage. Although we cannot explain the related phenomena in quantitative fashion, we believe that a combination of reasons can be assigned. Reordering of atoms and molecules within the electrode and polymer layers occur. In addition, the n-doped Si substrate with the native oxide on top could be charged as the result of the applied voltage pulses. This phenomenon could also explain the high level of deflection, which is well above the predicted values by STONEY formula [20]. The hypothesis, that the 20 or 30 nm-thin SiO_2 -layer acts as solid dielectric and generates an additional torque on the substrate, has to be proven, but sounds reasonable.

5. CONCLUSIONS

From the strain-dependent conductivity measurements we conclude that 10 nm-thin Au electrodes are a reasonable choice, although they show a resistivity twice as high as films thicker than 14 nm. Optical and AFM imaging served for the visualization of the defect structure of the thin-film Au electrodes. These images, that show a network of cracks, allow for an explanation of the electrode-thickness-dependent actuation characteristics for strains of up to 20 %.

We have demonstrated that the cantilever bending approach enables the measurement of the mechanical properties of the partially polymerized silicone films, which were heat-cured for selected periods of time. The actuation response can quantitatively be described using the decay constant and the total relaxation of actuation, both dependent on the degree of cross-linking of the confined micrometer-thin polymer film.

The cantilever bending approach also yields the voltage-dependent characteristics of multi-cycle actuation with a frequency of for example 0.1 Hz. For the single-crystalline Si substrate we identified actuation amplitudes that are higher than expected. The characteristic temporal behavior includes a relaxation of the maximum deflection with increasing number of actuation cycles, a phenomenon equally pronounced for the applied voltages. The detailed understanding of these observations need further research activities.

ACKNOWLEDGMENTS

The authors are grateful to Prof. Dr. Thomas Ihn, Physics Department, ETH Zurich, Switzerland, for the detailed discussions and advice concerning the conductivity measurements. The financial support of the Swiss National Science Foundation (project 200021-135496) and the nano-tera.ch initiative *SmartSphincter* is gratefully acknowledged. Furthermore, the authors thank VICTREX for supporting us with PEEK films.

REFERENCES

- [1] Macmillan, A. K., Merrie, A. E., Marshall, R. J., and Parry, B. R., "The prevalence of fecal incontinence in community-dwelling adults: a systematic review of the literature," *Diseases of the Colon and Rectum* **47**(8), 1341-1349 (2004).
- [2] Stoker, J., Halligan, S., and Bartram, C. I., "Pelvic floor imaging," *Radiology* **218**(3), 621-641 (2001).
- [3] Dey, A. N., [Characteristics of elderly nursing home residents: Data from the 1995 National Nursing Home Survey] US Department of Health and Human Services, Centers for Disease Control and Prevention, National Center for Health Statistics, (1997).
- [4] Nelson, R., Furner, S., and Jesudason, V., "Fecal incontinence in Wisconsin nursing homes," *Diseases of the Colon and Rectum* **41**(10), 1226-1229 (1998).
- [5] Saga, S., Vinsnes, A., Morkved, S., Norton, C., and Seim, A., "Prevalence and correlates of fecal incontinence among nursing home residents: a population-based cross-sectional study," *BMC Geriatrics* **13**(1), 87 (2013).
- [6] Müller, B., Deyhle, H., Mushkolaj, S., and Wieland, M., "The challenges in artificial muscle research to treat incontinence," *Swiss Medical Weekly* **139**, 591-595 (2009).
- [7] Pelrine, R., Kornbluh, R., Pei, Q., and Joseph, J., "High-speed electrically actuated elastomers with strain greater than 100%," *Science* **287**(5454), 836-839 (2000).
- [8] Habrard, F., Patscheider, J., and Kovacs, G., "Super-compliant metallic electrodes for electroactive polymer actuators," *Proc. of SPIE* **8340**, 834013 (2012).
- [9] Graz, I. M., Cotton, D. P. J., and Lacour, S. P., "Extended cyclic uniaxial loading of stretchable gold thin-films on elastomeric substrates," *Applied Physics Letters* **94**(7), 071902 (2009).
- [10] Smits, F. M., "Measurement of sheet resistivities with the four-point probe," *Bell System Technical Journal* **37**(3), 711-718 (1958).
- [11] Valdes, L. B., "Resistivity measurements on germanium for transistors," *Proc. of IRE* **42**(2), 420-427 (1954).
- [12] Wang, Y., Schimpf, P. H., Haynor, D. R., and Yongmin, K., "Geometric effects on resistivity measurements with four-electrode probes in isotropic and anisotropic tissues," *IEEE Transactions on Biomedical Engineering* **45**(7), 877-884 (1998).
- [13] Binnig, G., Quate, C. F., and Gerber, C., "Atomic Force Microscope," *Physical Review Letters* **56**(9), 930-933 (1986).
- [14] Gimzewski, J. K., Gerber, C., Meyer, E., and Schlittler, R. R., "Observation of a chemical reaction using a micromechanical sensor," *Chemical Physics Letters* **217**, 589-594 (1994).
- [15] Köser, J., Gaiser, S., and Müller, B., "Contractile cell forces exerted on rigid substrates," *European Cells and Materials* **21**, 479-487 (2011).
- [16] Meyer, G., and Amer, N. M., "Novel optical approach to atomic force microscopy," *Applied Physics Letters* **53**(12), 1045-1047 (1988).
- [17] Urwyler, P., Häfeli, O., Schiff, H., Gobrecht, J., Battiston, F., and Müller, B., "Disposable polymeric micro-cantilever arrays for sensing," *Procedia Engineering* **5**, 347-350 (2012).
- [18] Urwyler, P., Schiff, H., Gobrecht, J., Häfeli, O., Altana, M., Battiston, F., and Müller, B., "Surface patterned polymer micro-cantilever arrays for sensing," *Sensors and Actuators A: Physical* **172**(1), 2-8 (2011).
- [19] Weiss, F. M., Deyhle, H., Kovacs, G., and Müller, B., "Designing micro- and nanostructures for artificial urinary sphincters," *Proc. of SPIE* **8340**, 83400A (2012).
- [20] Weiss, F. M., Zhao, X., Thalmann, P., Deyhle, H., Urwyler, P., Kovacs, G., and Müller, B., "Measuring the bending of asymmetric planar EAP structures," *Proc. of SPIE* **8687**, 86871X (2013).
- [21] Weiss, F. M., Töpfer, T., Osmani, B., Winterhalter, C., and Müller, B., "Impact of electrode preparation on the bending of asymmetric planar electro-active polymer microstructures," *Proc. of SPIE* **9056**, 905607 (2014).
- [22] Osmani, B., Töpfer, T., Deschenaux, C., Nohava, J., Weiss, F. M., Leung, V., and Müller, B., "Micro- and nanostructured electro-active polymer actuators as smart muscles for incontinence treatment," *AIP Conference Proceedings* **1646**, 91-100 (2015).

- [23] Ihn, T., [Semiconductor nanostructures: Quantum states and electronic transport] Oxford University Press, (2010).
- [24] Svorcik, V., Zehentner, J., Rybka, V., Slepicka, P., and Hnatowicz, V., "Characterization of thin gold layers on polyethyleneterephthalate: transition from discontinuous to continuous, homogenous layer," *Applied Physics A* **75**(4), 541-544 (2002).
- [25] Panchuk, D. A., Bazhenov, S. L., Bol'shakova, A. V., Yarysheva, L. M., Volynskii, A. L., and Bakeev, N. F., "Correlation between structure and stress-strain characteristics of metallic coatings deposited onto a polymer by the method of ionic plasma sputtering," *Polymer Science Series A* **53**(3), 211-216 (2011).
- [26] Hodgman, C. D., [Handbook of Chemistry and Physics], Cleveland(1975).
- [27] Chan, E. P., Page, K. A., Im, S. H., Patton, D. L., Huang, R., and Stafford, C. M., "Viscoelastic properties of confined polymer films measured via thermal wrinkling," *Soft Matter* **5**(23), 4638-4641 (2009).

2.4 Siloxane-based thin films for biomimetic low-voltage dielectric actuators

Single layer dielectric elastomer actuators based on thermally evaporated, UV-cured polydimethylsiloxane sandwiched between sputtered Au-electrodes are fabricated.

The choice of pre-polymer determines the depositions rates for PDMS thin film preparation.

The PDMS chain length defines the network density - the stiffness of the polymer network can be tailored.

Manufactured as asymmetric cantilever structures, the bending characteristic revealed a maintained actuation of a 200 nm-thin film, activated in the voltage range between 1 and 12 V, compared to a 4 μm -thick, spin-coated film, operated between 100 and 800 V.

The force of a 200 nm-thin film cantilever actuator is quantified to about 10^{-4}N .

A multilayer actuator with more than 10^4 layers would reach forces comparable to natural muscles.

Published in Sensors and Actuators A: Physical



ELSEVIER

Contents lists available at ScienceDirect

Sensors and Actuators A: Physical

journal homepage: www.elsevier.com/locate/sna

Siloxane-based thin films for biomimetic low-voltage dielectric actuators



Tino Töpfer*, Florian Weiss, Bekim Osmani, Christian Bippes, Vanessa Leung, Bert Müller

University of Basel, Gewerbestrasse 14, Allschwil, CH 4123, Switzerland

ARTICLE INFO

Article history:

Received 10 December 2014

Received in revised form 15 June 2015

Accepted 15 June 2015

Available online 30 June 2015

Keywords:

Polydimethylsiloxane
Molecular beam deposition
AFM nanoindentation
Ultraviolet spectroscopy
Mid-infrared spectroscopy
Cantilever bending
Artificial muscle

ABSTRACT

Molecular beam deposition of siloxane-based polymer thin films was employed to realize single-layer dielectric elastomer actuators. With molecular weights of 6000 and 28,000 g/mol, vinyl-terminated polydimethylsiloxane (PDMS) was evaporated under high-vacuum conditions at crucible temperatures between 100 and 180 °C. Both deposition rate and realizable film thickness showed linear dependency with respect to the crucible temperature and were significantly higher for PDMS with lower molecular weight. Optimized growth conditions for 6000 g/mol were obtained at 180 °C with a deposition rate of (130 ± 5) nm per hour and a maximal film thickness of (530 ± 1) nm. Thermally induced polymerization was observed to limit the maximum accessible evaporation temperature for hydride-terminated PDMS above 180 °C and for vinyl-terminated PDMS above 230 °C. Ultraviolet (UV) light induced polymerization of vinyl-terminated PDMS was successfully established via radicalization at the functional vinyl end groups of the chains. Atomic force microscopy nanoindentation of the UV-polymerized network reveals that the oligomer chain length determines the elastic modulus of the polymer layer. Manufactured as asymmetric cantilever structures, the bending characteristic gave evidence that a 200 nm-thin film, activated in the voltage range between 1 and 12 V, maintains the actuation compared to a 4 μ m-thick, spin-coated film, operated between 100 and 800 V. The force of the presented 200 nm-thin film cantilever actuator was about 10^{-4} N. This means that a multilayer actuator with more than 10^4 layers would reach forces comparable to natural muscles. Therefore, such nanostructures can qualify for medical applications for example to treat severe incontinence.

© 2015 The Authors. Published by Elsevier B.V. This is an open access article under the CC BY-NC-ND license (<http://creativecommons.org/licenses/by-nc-nd/4.0/>).

1. Introduction

Research on dielectric, electrically activated polymer (EAP) actuators for biomimetic implants focuses toward a significant reduction of the actuation voltages [1,2]. Micrometer-thick, silicone-based polymer films, prepared for example by spin-coating, require voltages in the range of several 100 V to a few kV to reach thickness strains of 25 to 48% [3,4]. Although the generation of high voltages through electromagnetic transformers is established, the limitations are large component size and often relatively low efficiency. Associated costs and potential health risks for medical device applications within the human body are further drawbacks. Therefore, one should either increase the dielectric constant of the polymer, for example by adding fillers in the elastomer network [5,6], or decrease the film thickness to reduce the operation voltage. Taking advantage of molecular beam deposi-

tion (MBD), we follow the pathway to reduce the film thickness to the sub-micrometer range. Compared with the well-established spin coating [7], solvents are not required. In order to reach the necessary actuation forces/pressures, however, stack actuators [8] have to be realized. This approach implies the reliable preparation of both polymer and stretchable electrode multilayers. Although MBD is known for excellent film homogeneity and relatively low defect densities, reliable MBD for polymer layers is challenging as heating in the crucible often causes dissociation to lower molecular weight components, pyrolysis, and even polymerization [9]. Such processes significantly modify evaporation rates and beam composition. These complex phenomena limits the evaporation temperature ranges typically to values between 150 and 450 °C and the deposition rates of the material to values below the desired range of about 1 μ m/h or 1 monolayer/s. Nevertheless, once vacuum deposition of appropriate organic and electrode materials is available, one can prepare and characterize in situ film growth of multi-stack actuators under well-defined high-vacuum (HV) conditions.

* Corresponding author.

It is hypothesized that MBD of vinyl-terminated polydimethylsiloxane (PDMS) with molecular weights M_w of 6000 and 28,000 g/mol allows for the preparation of low-voltage DEAs under HV conditions. We know that siloxane-based polymers are dielectric elastomers in actuator configurations because of their elasticity and dielectric behavior. Strain levels of 30 to 40% were reached [10]. Especially the millisecond response and the acceptance as a biocompatible material for applications within the human body make silicone suitable for biomimetic applications in artificial muscles [10,11].

Cross-linking of PDMS is achievable through the presence of functional groups either at the chain end or in the form of a copolymer. Covalent bonding can be realized either by heat-induced curing using a catalyst [12] or applying ultra-violet radiation to force the photo-initiated reaction of radicals [13,14]. Mid-infrared (MIR)-spectroscopy, for example, can support the analysis of polymerization in vinyl-terminated PDMS under continuous illumination by means of a deuterium broadband lamp, avoiding any use of cross-linkers or catalysts.

To characterize the performance of planar EAP actuators one can place them on a rectangular cantilever and measure the bending as a function of the applied voltage. Recently, experimental results of such a cantilever bending system [15] were published. Here a 200 nm-thin silicone film was embedded between two Au electrodes each 10 nm-thin. This EAP actuator was placed on a 25 μm -thick polyetheretherketone (PEEK) cantilever to obtain an asymmetric structure, which notably bends through the application of a voltage as small as a few volts. The cantilever bending approach is known from atomic force microscopy and similar methods to be extremely sensitive, see e.g. [16]. Therefore, this approach has also been applied for the current study.

It can reasonably be expected that low-voltage DEAs prepared by means of biocompatible materials with intrinsic properties, which include millisecond response and remarkable energy efficiency [10], will not only become parts of medical implants but find applications in a wide variety of other fields.

2. Materials and methods

2.1. Silicones used

The study on thermal evaporation is based on vinyl-terminated dimethylsiloxane DMS-V21 (Gelest Inc., Morrisville, PA, USA), vinyl-dimethylsiloxane copolymer AB116647 (abcr GmbH, Karlsruhe, Germany) and hydride-terminated hydride-dimethylsiloxane copolymer HMS-H271 (Gelest Inc., Morrisville, PA, USA). Elastosil 745 A/B (Wacker Chemie AG, München, Germany) is solely used for spin coating of micrometer-thick films.

2.2. Thermal characterization of PDMS

The characterization of thermal degradation was carried out with thermal gravimetric analysis (TGA) using a TGA/SDTA851e system (Mettler Toledo, Greifensee, Switzerland). The data were acquired with a heating rate of 10 K per minute under nitrogen atmosphere for PDMS terminated with hydride and vinyl groups. The temperature at which thermally induced crosslinking occurs was determined by heating micrometer-thin films with a rate of 5 K per hour, starting from 150 °C under atmospheric conditions.

2.3. Thermal evaporation of PDMS

The deposition experiments were carried out under high-vacuum conditions. After bake-out at a temperature of 120 °C for two hours, a base pressure of 10^{-8} mbar was achieved using a

Agilent SH-110 dry scroll pump (Swissvacuum Technologies SA, Marin-Epagnier, Switzerland) with a pumping speed of 110 l/min in combination with Agilent V-81-M turbo pump (Swissvacuum Technologies SA, Marin-Epagnier, Switzerland) with a pumping speed of 77 l/s for N_2 at a rotation frequency of 1350 Hz. We utilized a low temperature effusion cell (Dr. Eberl MBE Komponenten GmbH, Weil der Stadt, Germany) with precise regulation and high temperature stability in order to realize a homogeneous temperature distribution inside the crucible (NTEZ crucible with a volume of 2 cm^3). The temperature ramp of the evaporator was adjusted to a heating rate of 10 K per minute. When the shutter of the evaporator was opened a rise of the vapor pressure was detected to 1×10^{-6} mbar and up to 5×10^{-6} mbar at 120 °C and 180 °C source temperature, respectively. The pressure was detected with a FRG-700 Varian inverted Magnetron Pirani Gauge (Swissvacuum Technologies SA, Marin-Epagnier, Switzerland) in front of the turbo pump, at a distance of 600 mm to the evaporator. The substrate was placed 300 mm in front of the evaporation source. A quartz crystal microbalance (LewVac, Ote Hall Farm, Burgess Hill, UK) served for the film thickness measurement.

2.4. Crosslinking of poly-dimethylsiloxane (PDMS)

Photodecomposition of Si-vinyl bonds occurs as a result of direct UV radiation with a wavelength below 300 nm [17]. To obtain the radicalization wavelength of the Si-vinyl bonds, a UV-vis measurement was performed with an Agilent 8453 Spectrometer (Agilent Technologies, Basel, Switzerland). The solvent hexane (HPLC grade, Fischer Scientific, Wohlen, Switzerland) was utilized.

The UV radicalization was realized with a deuterium D2 broadband UV lamp (Yuyu Lightning, China) covering a spectral range between 180 and 450 nm with maximum intensity at a wavelength of 210 nm.

Mid-infrared (MIR) spectroscopy with a Varian 670-IR spectrometer (Varian Inc., Santa Clara, USA) was used to investigate the resulting polymer network by analyzing the absorption bands of bond-vibrations from 600 to 4000 cm^{-1} with steps of 4 cm^{-1} .

2.5. Nanoindentation of PDMS cross-linked networks

The nanomechanical properties of the deposited polymers were quantified using the FlexAFM ARTIDIS system (Nanosurf AG, Liestal, Switzerland). The nominal spring constant of the cantilevers (CONTSCR, Nanosensors, Neuchatel, Switzerland) was determined to be 0.2 N/m using the Sader method [18]. The ARTIDIS system allows systematic sampling at selected points of interest. The size of each spot was either $15 \times 15 \mu\text{m}^2$ or $20 \times 20 \mu\text{m}^2$. Each spot was overlaid with a 64×64 points array. The array defines the locations of the 4096 nanoindentation tests. The FlexAFM ARTIDIS automatically acquired the data and generated a stiffness map and histogram for each spot. The power law method by Oliver & Pharr [19] was used to calculate the Young's modulus. The CONTSCR-cantilever tip radius was 7 nm. The approach was done with a speed of 6 $\mu\text{m/s}$ while the measurements were taken at a force setpoint of 4 nN.

2.6. Preparation and mechanical characterization of asymmetric EAP structures

The polymer films, either grown by MBD (see Section 2.3) with a thickness of 200 nm or spin-coated (Spincoater WS-400B-6NPP, Laurel Technologies, North Wales, USA) with a thickness of 4 μm (Elastosil A/B at 3000 rpm for 150 s, heat cured for 2 h at 120 °C), were embedded between two 10 nm sputtered Au-electrodes (Magnetron sputter system, Balzers Union SCD040,

Lichtenstein) and placed on a 25 μm polyetheretherketone PEEK substrate (Aptiv 2000, Vitrex, Lancashire, UK). The related sputtering conditions corresponded to 0.05 mbar Ar-atmosphere and a constant working current of 30 mA. The thickness of the Au electrodes was 10 nm, determined by a calibration curve plotting time versus thickness measured using a quartz crystal microbalance (QSG 301, Balzers, Lichtenstein). To get contact access to the lower electrode the grown PDMS layer was dissolved and washed off partially by submerging the structure into ethyl acetate. On the growth of an adhesion layer between PEEK and Au or PDMS and Au was renounced to simplify the actuation characterization. Nevertheless recently published results indicate that the conductivity as well as the adhesion of a 10 nm-thin Au electrode to the polymer is sufficiently high enough to follow strains as large as 20% [20]. The thickness of the polymer layer after MBD or spin-coating and following polymerisation was determined using 3D laser microscopy (Keyence VK-X200, Keyence International, Belgium) with a spatial resolution of 0.5 nm in z-direction. Finally, this stack was cut into asymmetric cantilever structures (cf. Fig. 8).

With the advantage of no severe geometric restrictions, the cantilever beam deflection method has shown the potential to characterize the mechanics of thin films on a substrate [21–23], and cells on a cantilever [24] or even on whole asymmetric EAP structures [25–27]. Therefore, we applied this method to characterize EAP films by means of electrical actuation. A detailed description of the utilized apparatus can be found in literature [15,26]. When a voltage U is applied between the two electrodes, an electrostatic pressure p leads to a strain in the vertical direction S_z (Eq. (1)), which is then, due to the incompressibility of the polymer network, equally translated into a strain in horizontal directions S_x and S_y .

$$S_x = \frac{1}{2}S_z = -\frac{p}{2E} = -\frac{1}{2E}\epsilon_r\epsilon_0\left(\frac{U}{h_f}\right)^2 \quad (1)$$

This strain in the horizontal direction leads to a surface stress between the EAP film with thickness h_f and the PEEK-substrate, resulting in a torque that bends the entire EAP-cantilever structure. The bending can be detected by the deflection d of a reflected laser beam (660 nm Streamline diode laser, Laser2000, Germany) on a position sensitive detector (PSD, Spoton Laser2000) (see Fig. 4). According to Stoney [28]

$$S_x = \frac{E_s h_s^2}{6(1-\nu_s)h_f} \times \frac{d}{LD} \quad (2)$$

the strain S_x between the surfaces is proportional to the displacement d , which is dependent on the substrate properties (elastic modulus E_s thickness h_s). Merging Eqs. (1) and (2) it becomes clear that one can expect a quadratic dependence between the applied voltage U and the displacement d . The ratio between displacement d , cantilever length L , and the distance between the cantilever and the detector D can otherwise be described by the inverse of the bending radius R with $d/LD = 1/R$.

3. Results

3.1. Thermal characterization of PDMS

The thermal gravimetric analysis of the PDMS showed that the temperature onset of molecular weight loss $T_{\text{weight-loss}}$ is, with a value of $450^\circ\text{C} \pm 20\text{K}$, 200 K lower for hydride-terminated (HMS-H271) than for the vinyl-terminated polymers (DMS-V21 and AB116647). In addition, we observed that hydride-terminated PDMS started to form cross-linked networks at temperatures above $180^\circ\text{C} \pm 5\text{K}$, whereas vinyl-terminated PDMS required temperatures of $230^\circ\text{C} \pm 5\text{K}$ to form cross-linked networks under ambient conditions.

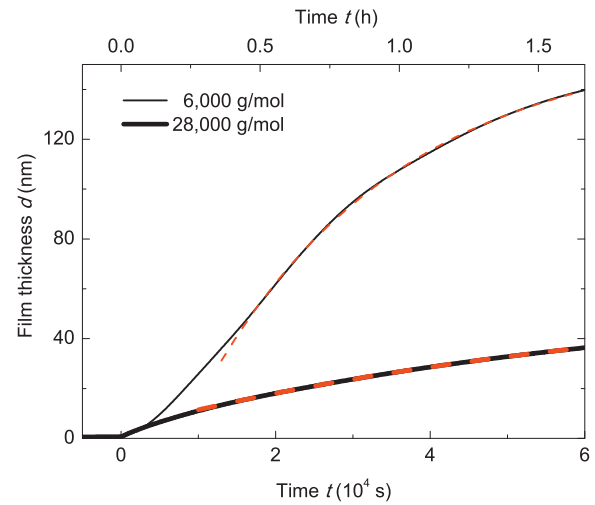


Fig. 1. Temporal behavior of molecular beam deposition of PDMS with molecular weights of 6000 (thin line) and 28,000 g/mol (thick line) at a source temperature of 120°C and a background pressure of 1×10^{-6} mbar. Eq. (3) describes the experimentally observed time dependence as the fits (dashed lines) of the polymers with the molecular weights of 6000 g/mol ($d_{\text{max}} = (160.0 \pm 0.5)$ nm, $\tau = (2.52 \pm 0.01) \times 10^4$ s) and of 28,000 g/mol ($d_{\text{max}} = (58.0 \pm 0.2)$ nm, $\tau = (6.56 \pm 0.03) \times 10^4$ s), as indicated.

3.2. Thermal evaporation of PDMS

Figs. 1 and 2 demonstrate that the selected polymers can be evaporated under high-vacuum conditions to fabricate nanometer-thin polymer films. Due to the higher thermal stability of the vinyl-terminated PDMS, detailed investigations of MBD growth for DMS-V21 and AB116647 were gathered. At a source temperature of 120°C in the time frame up to 10^4 s, a linear growth behavior for both polymers was observed. Eq. (3) below shows that the growth rate, related to the particle flux $dd/dt = j(T)$, is proportional to the

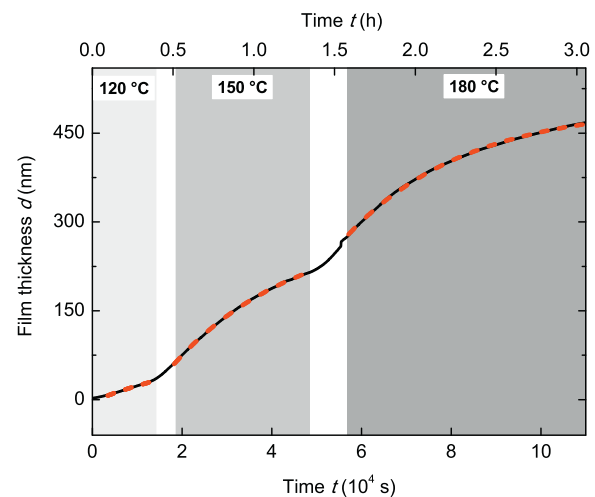


Fig. 2. The time dependence of the evaporation rate can be adjusted by the choice of the evaporation temperature. The representative graph for the molecular beam deposition of PDMS with a molecular weight of 6000 g/mol (DMS-V21) follows the behavior given by Eq. (3) at each of the source temperatures given. The time constant increases from (6.0 ± 0.3) via (8.6 ± 0.2) to $(10.4 \pm 0.1) \times 10^4$ s and the film thickness at infinite time reaches (95 ± 5) , (280 ± 1) , and (530 ± 1) nm, respectively.

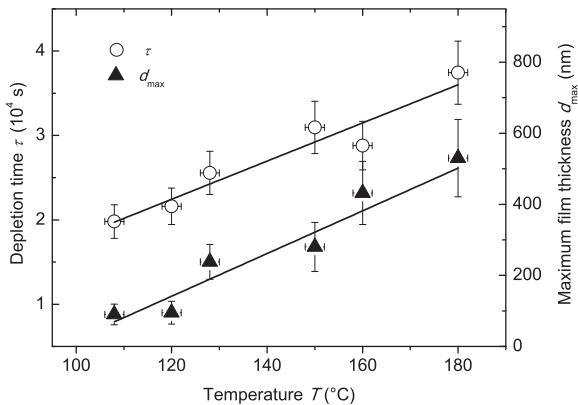


Fig. 3. The temperature dependences of the asymptotic film thickness d_{\max} and the fitted time constants τ exhibit a linear behavior for the vinyl-terminated PDMS with a molecular weight of 6000 g/mol. One can take advantage from this behavior and select the optimized source temperature to reach the desired film thickness within the available period of time.

equilibrium vapor pressure $p(T)$ and inversely proportional to the mass m of the molecules [29]:

$$j(T) = \frac{p(T)}{\sqrt{2\pi m k T}}. \quad (3)$$

The equation contains the Boltzmann constant k . During evaporation of the two polymers at the source temperature of 120 °C the background pressure was 10^{-6} mbar. The relation between the growth rates of the polymers with molecular weights of 6000 and 28,000 g/mol is therefore determined by the ratio of the square roots of the molecular weights, i. e. about 2.2. Experimentally we obtained growth rates of (130 ± 5) and (35 ± 2) nm per hour, respectively, which corresponds to a ratio of 3.7.

For evaporation times above 10^4 s we observed a deviation from the linear behavior. The growth rates became smaller and smaller. The acquired behavior can be described by the following equation:

$$d(t) = d_{\max} \left[1 - \exp\left(-\frac{t}{\tau}\right) \right]. \quad (4)$$

For the source temperature of 120 °C we have fitted the two parameters, i.e. the asymptotic film thickness d_{\max} and the time constant τ . Fig. 1 demonstrates that the polymer with lower molecular weight has a 2.6 smaller time constant than the PDMS with the larger molecular weight. The ratio of the maximal film thicknesses is found to be about 2.8.

The data of Fig. 1 show that using the present experimental setup, the polymer DMS-V21, and a source temperature of 120 °C one cannot realize films with a thickness above 160 nm. Fig. 2 presents our attempts for the polymer DMS-V21 to increase the maximal film thickness by applying higher source temperatures, i.e. 150 and 180 °C. This deposition experiment with a lower filling level of the source led to maximal film thicknesses of (95 ± 5) , (280 ± 1) , and (530 ± 1) nm, respectively. The related time constants also significantly increased from (6.0 ± 0.3) via (8.6 ± 0.2) to $(10.4 \pm 0.1) 10^4$ s.

Fig. 3 demonstrates that the asymptotic film thickness and the related time constants linearly depend on the source temperature from 110 to 180 °C. The asymptotic film thickness as a function of the source temperature is described using the linear fit $d_{\max}(T) = (6.0 \pm 1.1) \text{ nm/K} \times T - (580 \pm 130) \text{ nm}$. The time constant follows a similar behavior: $\tau(T) = (226 \pm 31) \text{ s/K} \times T - (470 \pm 40) \text{ s}$. The error bars of the fit parameters not only contain statistical errors derived from the fitted data but also reasonable estimates

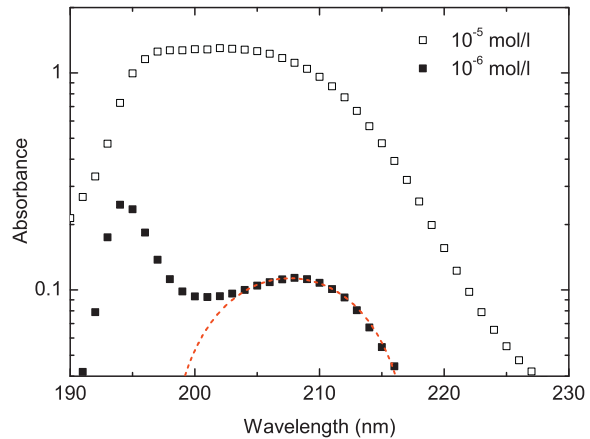


Fig. 4. Ultra-violet spectroscopy of the vinyl-terminated polymer AB116647, diluted in hexane to 10^{-5} and 10^{-6} mol/l. The $\pi - \pi^*$ transition of the vinyl double bond at $(207.7 \pm 0.1) \text{ nm}$ was determined with a Gaussian fit using a solvent cut-off at the wavelength of $(194.5 \pm 0.1) \text{ nm}$.

of the systematic errors. The measured data and the related linear fits displayed in Fig. 3 lead to the conclusion that at a source temperature below 100 °C, one does not obtain any meaningful film thickness. In general, deposition rates as high as $1 \mu\text{m}$ per hour are desired, corresponding to source temperatures above 180 °C. At source temperatures between 180 and 200 °C, however, we observed boiling retardation of the polymer DMS-V21 within the crucible associated with spitting of polymer material onto the substrate, although the evaporation source is known for homogenous temperature distribution.

3.3. Crosslinking of poly-dimethylsiloxane (PDMS)

Fig. 4 displays the absorbance of the AB116647 polymer film for wavelengths between 190 and 230 nm (ultra-violet spectroscopy). The dilution in hexane was adjusted to 10^{-6} mol/l to discriminate between the absorption peaks of the vinyl group and the solvent (see Fig. 4). Based on a Gaussian fit, one obtains the wavelength of the $\pi - \pi^*$ transition of the vinyl double bond. It corresponds to $(207.7 \pm 0.1) \text{ nm}$.

The spectrum of the deuterium lamp thus covers the wavelength for activating the cleavage of the vinyl double bonds. Applied for a period of three hours, the polymer thin film received an energy density of $(3000 \pm 100) \text{ W/m}^2$. The irradiance at the wavelength of 207.7 nm at a distance of 0.2 m was measured to be $(3.0 \pm 0.1) \text{ mW/m}^2$ per nm.

Mid-infrared (MIR) spectroscopy data, as presented in Fig. 5, served for the investigation of modifications in the polymer owing to treatment with ultra-violet light. The data given in Fig. 5(a) show the absorption bands of vinyl ($\text{SiCH}=\text{CH}_2$) vibrations at the wavenumbers of 1590 cm^{-1} , 1410 cm^{-1} , and 960 cm^{-1} , as well as of the C–H bond vibration at the wavenumber of 3060 cm^{-1} as known from the literature [30].

The spectroscopy data of Fig. 5(b) include the Si–O vibration band at the wavenumber of 1065 cm^{-1} and the $\text{SiCH}_2-\text{CH}_2\text{Si}$ vibrations around a wavenumber of 1130 cm^{-1} [30]. The absorbance of the polymer film before and after the UV irradiation have been normalized for the absorption band at the wavenumber of 1065 cm^{-1} , since the Si–O bonds are the most stable ones in the silicone chains. Table 1 of Ref. [31] contains the related dissociation energy, which corresponds to a radicalization wavelength of 155 nm. This wavelength is well below the ones generated by the lamp used.

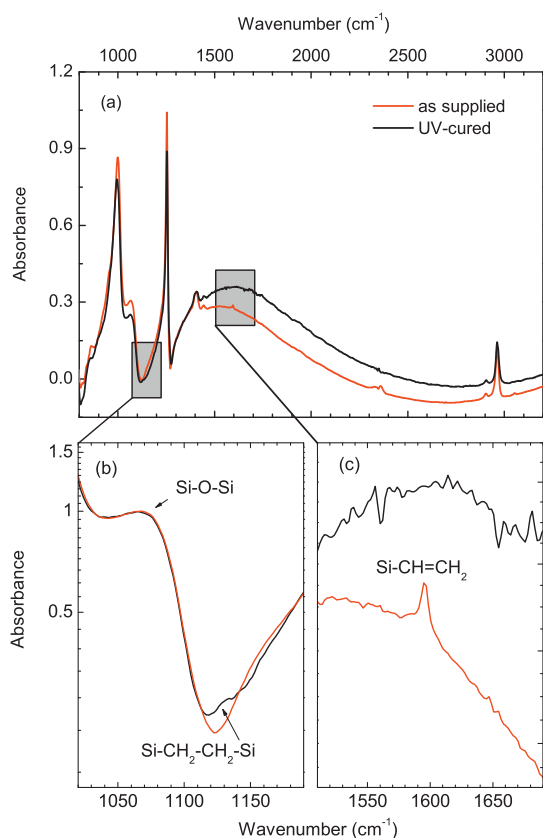


Fig. 5. Mid-infrared spectroscopy of the vinyl-terminated polymer DMS-V21: (a) The absorbance of the polymer as supplied corresponds to the red-colored data, the data in black are the absorbance values of the ultra-violet-cured thin film. (b) The data within the selected spectral range verify the occurrence of the absorption band around a wavenumber of 1130 cm^{-1} attributed to $\text{SiCH}_2\text{—CH}_2\text{Si}$ vibrations. The absorbance was normalized according to the Si—O—Si vibration band at the wavenumber of 1065 cm^{-1} a feature assumed to be unaffected by the applied radiation. (c) The change of the vinyl vibration (SiCH=CH_2) at the wavenumber of 1590 cm^{-1} after the treatment is obvious. (For interpretation of the references to colour in this figure legend, the reader is referred to the web version of this article.)

Therefore, the spectroscopy data of Fig. 5(b) clearly indicate that a significant number of $\text{SiCH}_2\text{—CH}_2\text{Si}$ bonds have been formed as the result of the UV treatment. At the wavenumber of 1130 cm^{-1} the absorbance increased from 0.22 to 0.26.

As exemplarily demonstrated for a wavenumber of 1590 cm^{-1} in Fig. 5(c), the peaks related to the vinyl bonds of the polymer before the UV treatment disappear after such a treatment.

3.4. Young's modulus determination of siloxane films

The frequency of the 4096 measured elastic moduli follows a Gaussian distribution for both the spin-coated and the evaporated DMS-V21 films. After UV-treatment, the spin-coated, $4\text{ }\mu\text{m}$ -thin polymer had an average elastic modulus of $(480.9 \pm 0.2)\text{ kPa}$ with a half width of $(16.2 \pm 0.2)\text{ kPa}$, whereas the 200 nm -thin film prepared by molecular beam deposition gave rise to an average elastic modulus of $(1685.8 \pm 1.4)\text{ kPa}$ with a half width of $(187.5 \pm 2.8)\text{ kPa}$. This means that the thin film prepared by evaporation at a source

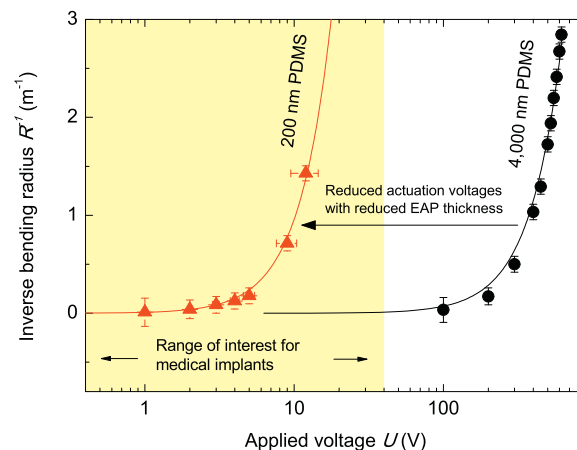


Fig. 6. The application of a voltage to the EAP micro- and nano-structures placed on $25\text{ }\mu\text{m}$ -thick PEEK substrates results in bending radii that follow the predicted quadratic behavior (fits represented by the full lines). The 200 nm -thin PDMS actuator demonstrated the aimed-for actuation efficiency within the medically relevant range of voltages for the realization of artificial muscles.

temperature of $120\text{ }^\circ\text{C}$ is 3.5 times stiffer than the spin-coated microstructure.

3.5. Bending of the asymmetric, dielectric actuators

Fig. 6 represents selected experimental data that follow the characteristic quadratic behavior predicted from Eq. (1). The full lines are the related fits. The currently state-of-the-art, $4\text{ }\mu\text{m}$ -thick, spin-coated, Elastosil A/B based actuators need voltages as high as several hundred volts to reach the desired deformation or stress-strain transfer (see Fig. 6). The 200 nm -thin, DMS-V21-based actuators (red triangles) prepared by molecular beam deposition at an evaporation temperature of $150\text{ }^\circ\text{C}$ and subsequent UV-treatment actuates at voltages as low as a few volts and hence can become the basis of artificial muscles within the human body. It should be noted that the breakdown voltages corresponded to $(60 \pm 6)\text{ V}/\mu\text{m}$ for the 200 nm -thin DMS-V21 polymer and $(120 \pm 12)\text{ V}/\mu\text{m}$ for the $4\text{ }\mu\text{m}$ -thick Elastosil film. The maximal detected curvature of the cantilevers before breakdown was $(2.67 \pm 0.2)\text{ m}^{-1}$ for the $4\text{ }\mu\text{m}$ -thick cantilever actuator applying a voltage of 500 V and $(1.43 \pm 0.1)\text{ m}^{-1}$ for the 200 nm -thin cantilever actuator using a voltage of 12 V . The corresponding driving forces, applied at the cross-sectional area of the polymer film, are $(5.9 \pm 0.7) \cdot 10^{-3}\text{ N}$ for the $4\text{ }\mu\text{m}$ -thick and $(6.9 \pm 1.2) \cdot 10^{-5}\text{ N}$ for the 200 nm -thin cantilever actuator, respectively. For the horizontally mounted cantilever the curvature was calibrated based on the gravitational force. For the $4\text{ }\mu\text{m}$ -thick actuator a curvature of $(1.41 \pm 0.22)\text{ m}^{-1}$ was detected. For the 200 nm -thin actuator the curvature corresponded to $(1.25 \pm 0.19)\text{ m}^{-1}$.

4. Discussion

PDMS is known for its resistance to environmental degradation induced by oxygen, ozone, and sunlight [6]. Furthermore, kinetics studies of thermal degradation have shown that the thermal stability of $(\text{CH}_3)_3\text{Si}$ end-blocked PDMS is present up to a temperature of $339\text{ }^\circ\text{C}$ under ambient conditions [32]. The thermal treatment of terminated PDMS, however, does exhibit reduced thresholds of thermally induced cross-linking in air. This behavior

is related to the higher thermal stability of the SiCH=CH₂ double bond compared to the Si–H bond. Either placed at the end or in the middle of the polymer chain, the SiCH=CH₂SiCH=CH₂ bonds have an enthalpy of (690 ± 4) kJ/mol (see Table 4.11 of Ref. [33]). Alternatively, to radicalize the vinyl group, dissociation energies of (435 ± 21) kJ/mol for SiC → Si + C [34] and of (424 ± 1) kJ/mol for CH₂ → CH + H [33] have been reported. The dissociation energy of the Si–H bonds is with an amount of (377 ± 13) kJ/mol significantly lower [34]. Due to the highest dissociation energy of (462 ± 1) kJ/mol for the methyl side groups (see Table 4.11 of Ref. [33]), the thermal stability of PDMS is given by the termination of the siloxane chain. Therefore, the lower temperatures for Si–H compared to Si–vinyl bonds have to be exceeded so that bond cleavage and cross-linking do occur. This coincides with the fact that oxidation rates during thermal treatment of Si–H groups were found to be higher than the rates for the Si–vinyl groups [17,35]. The enhanced thermal stability of vinyl-terminated PDMS enables the use of higher evaporation temperatures and hence complies more to the demand for high evaporation rates than hydride-terminated PDMS. Israeli et al. have shown that the termination with phenyl groups improves the thermal stability of PDMS even further [36].

Consequently, the thermal evaporation of the PDMS has restrictions owing to the thermal stability of the polymer chains. Above the temperature range at which the PDMS is stable, the physical and chemical properties change associated with the shift of the molecular weight distribution [9]. The result depends on the concurrent rates of the decay and chain-linking processes within the evaporator. For evaporation temperatures well below thermal instability one observes a constant growth rate, which only depends on the source temperature. We observed this behavior only for the polymer with a low molecular weight of 6000 g/mol and within a restricted period of time. Subsequently, we have found an asymptotic decrease of the growth rates that limits the film thickness to a maximal value given by the choice of the source temperature. In general, time-dependent growth processes with *N* particles are described by a rate equation, often simply a differential equation of first order:

$$\frac{d^2N(t, T)}{dt^2} + \frac{1}{\tau}N(t, T) = 0. \quad (5)$$

Under static temperature conditions of the evaporation source, which we can reasonably assume, integration over time leads to the exponential behavior of *N*(*t*) with the number of particles near the surface of the evaporation material *N*_s and the number of particles in the evaporation material *N*_c.

$$N(t) = N_s + N_c \exp\left(-\frac{t}{\tau}\right). \quad (6)$$

At a source temperature below 180 °C only molecules with a molecular weight much lower than the mean value and which are in the surface region of the evaporation material can leave the source. We hypothesize that the diffusion of the molecules does not compensate for the molecule's loss as the result of evaporation.

Thus, after the depletion of the particles with a relatively low molecular weight localized near the surface of the evaporation material, the diffusion rate within the polymer, characterized by the time constant τ , dominates the growth behavior. The diffusion rate of polymers between bulk and surface region, described by their viscosity, is inversely proportional to the molecular weight; in other words the surface depletion decreases with lower molecular weight. The evaporation rate, according to Eq. (3), is also inversely proportional to the molecular weight, thus we expect that the low molecular weight polymers have been evaporated faster. The ratio of the growth rates has been 3.7 times higher for the polymer with molecular weight of 6000 g/mol

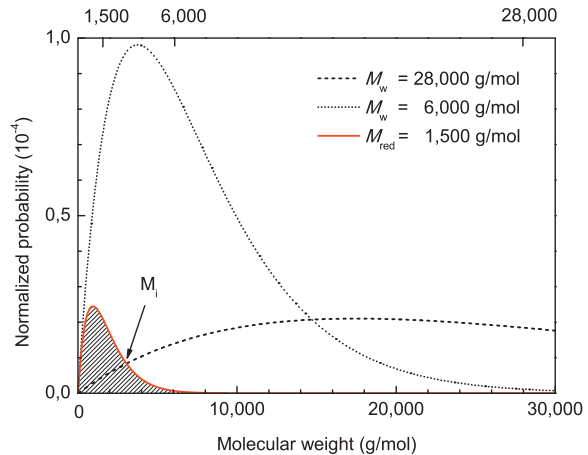


Fig. 7. The Flory distributions with average molecular weights of 28,000 g/mol (dashed line) and 6000 g/mol (dotted line) are shown. The schematic representation of evaporation probability of the polymer with nominal molecular weight of 6000 g/mol at a crucible temperature of 120 °C (red graph) demonstrates a preferential evaporation of low molecular weight oligomers with reduced average molecular weight of 1500 g/mol. The evaporation probability for polymers with nominal molecular weight of 28,000 g/mol is described by the overlap of MWD₂₈₀₀₀ with the reduced MWD₁₅₀₀. The reduced MWD₁₅₀₀ can be found when the ratio of determined maximum film thicknesses of 2.6 is assigned to equal the ratio of integrals over the two shifted MWDs of the supplied polymers (see Eq. (7)). (For interpretation of the references to colour in this figure legend, the reader is referred to the web version of this article.)

compared to 28,000 g/mol. The time constant for surface depletion, however, was found to be 2.6 smaller for the polymer with molecular weight of 6000 g/mol compared to 28,000 g/mol. Therefore, we conclude that the diffusion rate within the reservoir of polymer with molecular weight of 6000 g/mol is only 1.4 times higher compared to the polymer with molecular weight of 28,000 g/mol.

The discrepancy factor of 2.6 between the experimentally obtained maximal film thicknesses can be explained by considering the polydispersity of the evaporation material. The polymers we were supplied with have molecular weight distributions (MWD), which might be described according to the Flory distribution [37]. The probability for evaporation depends on the molecular weight of the individual molecule. In typical situations, the evaporation temperature is high enough that all molecules near the surface can leave the crucible, independent of their weight. There might be however conditions at which the smaller molecules are evaporated, whereas the larger ones remain within the crucible. At an evaporation temperature of 120 °C we reasonably presume that such thermal conditions are present for the polymers used. As a consequence, we believe that the MWD of the evaporated molecules significantly differs from the polymers supplied and a depletion of smaller molecules within the evaporation source causes the time dependence described. In order to obtain a better understanding of this phenomenon, one may take advantage of the experimentally obtained ratio of maximal film thicknesses of 2.6. Here, one may use an iterative approach to shift the MWD₆₀₀₀ of the supplied polymer with molecular weight of 6000 g/mol to a reduced average molecular weight *M*_{red} of the evaporated molecules, such that the integral over this reduced MWD_{red} (grey hatched area in Fig. 7) is 2.6 times higher than the integral over the overlap of MWD_{red} with MWD₂₈₀₀₀. The ratio of evaporated particles is mainly dependent on the derivation of the molecular weight distributions MWD_{red} and MWD₂₈₀₀₀, integrated in the range from the lowest

possible value (siloxane monomer: 88 g/mol) to the temperature-dependent value \bar{M}_i :

$$\frac{\frac{1}{C_{6000}} \int_{88 \text{ g/mol}}^{\infty} \left(\frac{P}{M_{6000}} M \exp \left[-\frac{P}{M_{\text{red}}} M \right] \right) dM}{\frac{1}{C_{28000}} \int_{88 \text{ g/mol}}^{M_i} \left(\frac{P}{M_{28000}} M \exp \left[-\frac{P}{M_{28000}} M \right] \right) dM + \frac{1}{C_{6000}} \int_{M_i}^{\infty} \left(\frac{P}{M_{6000}} M \exp \left[-\frac{P}{M_{\text{red}}} M \right] \right) dM} = 2.6. \quad (7)$$

As the number of particles in the reservoir before evaporation is expected to be equal, the MWDs of the supplied polymers are normalized by a factor of $C_{6000} = 3750$ and $C_{28000} = 17,500$. We assumed that the polydispersity P of PDMS corresponded to 1.6 as determined by single-molecule atomic force microscopy [38]. The solution of Eq. (7) leads to an average molecular weight (1500 ± 15) g/mol of the evaporated PDMS with a nominal molecular weight of 6000 g/mol and to (2800 ± 28) g/mol for the evaporated PDMS with a nominal molecular weight of 28,000 g/mol. Here the error bars are given by the ratio of the experimentally determined maximal film thicknesses. Accordingly, the probability of evaporation for molecules above a molecular weight of 7000 g/mol is negligible. We computed that only 6.2% of the polymer with a molecular weight of 6000 g/mol and 2.4% of the polymer with a molecular weight of 28,000 g/mol evaporate at the selected source temperature of 120 °C. These proportions explain the growth rates, which are low compared to the desired rates in the range of 1 μm per hour, and the depletion resulting in maximal film thicknesses of only a few hundreds of nanometers.

These thin films are therefore assumed to consist of molecules with a molecular weight between 88 and about 7000 g/mol. In order to increase the film's stability polymerization should be initiated. Polymerization of elastomer thin films, based on PDMS can be readily reached through hydrosilylation or heat-induced cross-linking reactions involving catalysts [12]. Alternatively the cleavage of the functional groups can also be realized by radicalization with UV light [13]. The radicalization of functional groups was observed with MIR spectroscopy and can be elucidated by assuming two main crosslinking paths. First, the extinction of the 1590 cm^{-1} absorption band indicates that the double bond of the vinyl group was activated under UV-radiation resulting in free highly reactive bonding sites on both sides of the double bond. These are expected to end-link the single chains along these functional groups, either connecting at the free electron on the CH— or the one on the CH₂—side of the vinyl group. Obviously, these connections contribute as an end-linking process to the extension of the polymer chains. Entanglement occurs at chain lengths above 16,000 g/mol as found by Al-Maawali et al. [38]. Thus, this chain length has to be reached to create an entangled network. Second, as observed by Graubner et al. [39,40], we detected a side reaction indicating the radicalization of the methyl (CH₃) side groups either by C—H or even Si—C bond rupture. Under ambient conditions UV-excited oxygen interacts with radicalized Si—C or C—H bonds resulting via side reactions in a cross-linking of the polymer chains by Si—O, Si bonds or SiCH₂—CH₂Si bonds to a three-dimensional network. Based on the complete disappearance of the vinyl vibrations we conclude that all the functional end groups were radicalized and linked, whereas for the amount of cross-linked methyl side groups only a qualitative conclusion can be drawn.

The degree of polymerization should be reflected in the mechanical properties of the film. Relying on the model of Mark et al. the elastic modulus for end-linked polymer networks is higher for low molecular weight chains than for networks consisting of high molecular weight polymer chains as the elastic modulus inversely depends on the molecular weight [41]:

$$Y = \frac{C\rho kT}{M_w}. \quad (8)$$

In this equation, $\rho = 0.97 \text{ g/cm}^{-3}$ is the density of the PDMS network at $T = 298.2 \text{ K}$, k is the Boltzmann constant and the constant C was determined to be 0.65 [41]. According to this model the elastic

modulus of the polymer DMS-V21 with a nominal molecular weight of 6000 g/mol is expected to be 280 kPa. The measured elastic modulus, determined by nanoindentation of a 4- μm , spin-coated, UV-polymerized polymer, was found to be (480.9 ± 0.2) kPa. This result implies that not only chain end-linking throughout the vinyl end groups occurs. Instead, as already proposed by the findings via MIR measurements, also cross-linking via the radicalized methyl-groups along the PDMS chain takes place, which leads to a 1.7 times higher elastic modulus than purely end-linked networks.

The elastic modulus of the MBD-grown DMS-V21 thin film was determined to be (1685.8 ± 1.4) kPa. According to Eq. (6), this value can be related to an average molecular weight of around 1000 g/mol of polymers being evaporated. We note that nanoindentation measurements contain a relative error of approximately 20% introduced by the uncertainty of the cantilever spring constant. This uncertainty is circumvented by comparing the ratios of elastic moduli determined under similar measurement conditions instead of relying on absolute values. Thus we can state that a much higher elastic modulus of the evaporated, UV-polymerized DMS-V21 thin film was found compared to the spin-coated, UV-polymerized thin film. Using the considerations of Mark et al., we estimated the average molecular weight of the evaporated polymer and calculated a value of 1700 g/mol [41]. This conclusion coincides with the considerations on the evaporation above. It should be mentioned that the quantities obtained are rather qualitative, whereas the reasonable hypothesis that the molecules with the lower molecular weight preferentially evaporate perfectly explains the experimental results. For application purposes the most important property is the functionality of the film within the actuator, which can be tested using a cantilever as substrate. At an evaporation temperature of 150 °C a 200 nm-thin DMS-V21 film was grown on an asymmetric cantilever microstructure. The stress-strain transfer is comparable to that of the 4- μm -thick, spin-coated EAP cantilever, but already operates at actuation voltages below 12 V. Therefore, reducing the EAP film thickness is promising for building actuators for medical applications, including artificial muscles.

The maximal curvatures, represented in Fig. 7, correspond to the expected bending moments of $(1.25 \pm 0.1) 10^{-7} \text{ Nm}$ and $(8.7 \pm 7.8) 10^{-10} \text{ Nm}$ for the 4 μm -thick polymer at a voltage of 500 V and the 200 nm-thin cantilever actuator at a voltage of 12 V, respectively. Induced by gravity, these curvatures would correspond to bending moments of $(1.03 \pm 0.05) \times 10^{-7} \text{ Nm}$ and $(2.03 \pm 0.12) \times 10^{-8} \text{ Nm}$ for the 4 μm -thick and the 200 nm-thin cantilever actuators according to the calibration measurement, described in Section 3.5. Thus the efficiency, given as the ratio of the bending moments, was found to be $(80 \pm 8)\%$ for the 4 μm -thick actuator, which is in agreement with the values published in literature for silicone-based DEAs [2]. Using the same approach, we have found a surprisingly high value of approximately 2300% for the 200 nm-thin EAP cantilever. It shows that the 200 nm-thin EAP actuator has more than 23 times higher actuation than expected. We can relate this phenomenon to the inhomogeneity of the polymer film, which contributes to the theoretical bending moment in a quadratic manner.

The breakdown voltage of 60 V/ μm for the 200 nm-thin DMS-V21 film, compared to 120 V/ μm for the 4 μm -thick Elastosil film, also indicates a significant inhomogeneity of the thermally grown film. We attribute the inhomogeneity more to the incorporated defects during UV-curing in atmosphere than to the MBD process

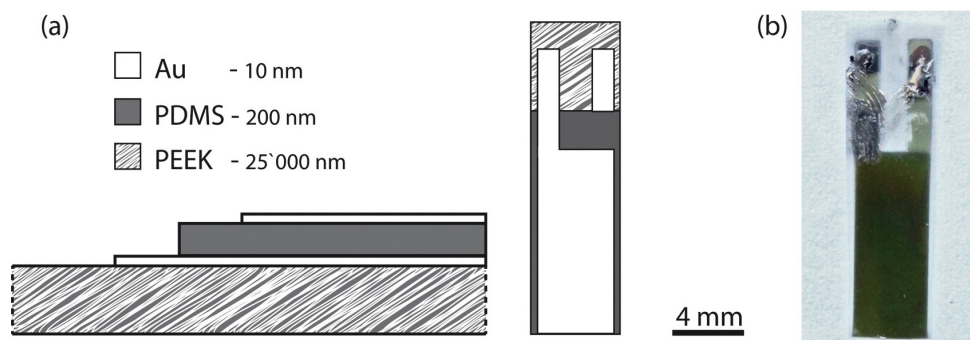


Fig. 8. a) A schematic cross-section and top view of an asymmetric cantilever actuator consisting of a PDMS-film embedded between two 10 nm-thin Au electrodes, placed on a 25 μm -thick PEEK substrate is presented. The shape of the Au electrodes was realized via a mask applied during the sputtering process as described in Section 2.4. b) The photograph of the 200 nm-thin single-layer EAP actuator prototype is shown.

itself. In addition, the UV source used provides an inhomogeneous illumination profile. Enabled through the higher mobility of the low molecular weight PDMS chains this led to a film thickness that is correlated with the irradiation intensity. This hypothesis is proposed based on a visual inspection of the surface, seen on the photograph in Fig. 8, and a statistical thickness measurement with 3D laser microscopy. An average thickness of (210 ± 60) nm was found with ten measurement spots over the active area of the cantilever actuator.

Another contribution to this low breakdown voltage is expected from the diffusion of Au atoms into the polymer film, which was not part of the present study, but is known to have a dominant impact for nanometer-thin elastomer films. A further source of uncertainty is the actual dielectric constant of the evaporated DMS-V21 film. Nevertheless, the breakdown voltage can compete with the values of $70 \text{ V}/\mu\text{m}$ obtained for matured silicones such as SVF5 [42]. Assuming that the dielectric properties of the evaporated DMS-V21 thin film are comparable to the Elastosil film, a strain of $(5.8 \pm 1.5)\%$ was according to Eq. (1) applied to the DMS-V21 network at an operating voltage of 12 V. We expect that the integration of UV-treatment into the high-vacuum environment and an UV-irradiation with a homogenous profile will significantly reduce the defect density and, hence, enhances the breakdown voltage and strain level, respectively.

Regarding the repetition and hysteresis for up to 1500 actuation cycles of such EAP cantilever actuators results, based on micrometer-thick polymer layers, have very recently been published [20], whereas the quantification of these parameters for 200 nm-thin film based EAP actuators is not quantified yet. For the determination of the curvature, however, we repeated the measurement for each data point presented for three times and did not notice any superior hysteresis.

5. Conclusion and Outlook

Molecular beam deposition of vinyl-terminated, siloxane-based polymers has been successfully shown, permitting the fabrication of nanometer-thin polymer films for single-layer EAP actuators. Actuation voltages smaller than 12 V were well below the approved medical limit and illuminate the key advance of these thin-film actuators making them promising candidates for biomimetic artificial muscles. MBD process control was realized by temperature and mass regulation of the utilized polymer. The choice of the polymer chain length allows the growth process as well as the resulting thin film elastic properties to be tailored. We have shown that the chain length defines the network density and therefore the stiffness of the polymer network. Via the polymer molecular weight also the

deposition rates and maximal realizable film thicknesses can be regulated. With lower molecular weight polymers higher deposition rates were realized leading to polymer films with a thickness of hundreds of nanometers.

The termination with functional groups at the polymer chain influences the thermal properties of the polymer. The main limitation constitutes the thermal stability of the polymer in use [43]. We proved studies on PDMS with different termination, showing that a vinyl-termination enhances the thermal stability compared to hydride termination [17]. For further improvement, phenyl termination was proposed by Israeli et al., which offers the possibility of using evaporation temperatures above 180°C and to achieve growth rates faster than $1 \mu\text{m}/\text{h}$ [36]. Combined with a homogeneity of better than 2%, the MBD of polymers allows for a reliable and repeatable growth process for stacked actuators, as needed to reach the desired actuation forces for artificial muscles. Once a multi-layer growth process is successfully established, nanometer-thin EAPs will address further applications in the field of biomimetics and robotics with a simplified energy supply as well as a reduced health risk. Proposed as artificial muscles dielectric EPA actuators exhibit strain levels well above 30% within the range of milliseconds response time [4] compared to less than 10% strain within a higher response time of a few seconds for stacked nematic elastomers [44]. Even state-of-the-art, tunable optics, based on relaxor ferroelectric actuators with driving voltages ranging from 40 to 500 V [45], could be replaced by low-voltage EAP actuators.

Acknowledgments

This activity was funded by the Nanotera.ch Initiative, a Collaboration of the Biomaterials Science Center (BMC) of the University of Basel, the Swiss Federal Laboratories for Material Science and Technologies (Empa), the Institute for Surgical Technology and Biomechanics (ISTB), Kantonsspital Schaffhausen and Inselspital Bern. The financial support of the Swiss National Science Foundation (project 200021-135496) is gratefully acknowledged. The authors thank Theodor Bühler (University of Applied Sciences Northwestern Switzerland) for the MIR-characterization of the polymer films, and Vitrex Europe for kindly providing the PEEK films.

References

- [1] Y. Bar-Cohen, Application of Dielectric EAP Actuators, in: Roy Kornbluh, R. Pelrine (Eds.), *Electroactive Polymers (EAP) Actuators as Artificial Muscles – Reality, Potential and Challenges*, 2nd ed., SPIE Press, Bellingham, 2004, pp. 475–495.
- [2] F. Carpi, D. Rossi, R. Kornbluh, R.P. Pelrine Sommer-Larsen, Dielectric elastomers as high-performance electroactive polymers, in: *Dielectric*

- Elastomers as Electromechanical Transducers, 1st. ed., Elsevier Ltd., Hungary, 2008, pp. 13–21.
- [3] R. Pelrine, R. Kornbluh, J. Joseph, R. Heydt, Q. Pei, S. Chiba, High-field deformation of elastomeric dielectrics for actuators, *Mater. Sci. Eng. C* 11 (2000) 89–100.
 - [4] R.E. Pelrine, R.D. Kornbluh, J.P. Joseph, Electrostriction of polymer dielectrics with compliant electrodes as a means of actuation, *Sens. Actuators A: Phys.* 64 (1998) 77–85.
 - [5] Q.M. Zhang, H. Li, M. Poh, F. Xia, Z.Y. Cheng, H. Xu, et al., An all-organic composite actuator material with a high dielectric constant, *Nature* 419 (2002) 284–287.
 - [6] A.E. Daugaard, S.S. Hassouneh, M. Kostrzewski, A.G. Benjenariu, A. Ladegaar Skov, High dielectric permittivity elastomers from well-dispersed expanded graphite in low concentrations, *Proc. SPIE* 8687 (2013) 868729.
 - [7] D.B. Hall, P. Underhill, J.M. Torkelson, Spin coating of thin and ultrathin polymer films, *Polym. Eng. Sci.* 38 (1998) 2039–2045.
 - [8] G. Kovacs, L. Düring, S. Michel, G. Terrasi, Stacked dielectric elastomer actuator for tensile force transmission, *Sens. Actuators A: Phys.* 155 (2009) 299–307.
 - [9] A.V. Rogachev, M.A. Yarmolenko, A.A. Rogachev, D.L. Gorbachev, Specific features of formation and molecular structure of polyaniline-based composite coatings deposited from active gas phase, *Russ. J. Appl. Chem.* 82 (2009) 1655–1661.
 - [10] R. Pelrine, R. Kornbluh, Q. Pei, J. Joseph, High-speed electrically actuated elastomers with strain greater than 100%, *Science* 287 (2000) 836–839.
 - [11] F.M. Weiss, H. Deyhle, G. Kovacs, B. Müller, Designing micro- and nanostructures for artificial urinary sphincters, *Proc. SPIE* 8340 (2012) 83400A.
 - [12] A.G. Wacker Chemie, <http://www.wacker.com/cms/de/products/product/product.jsp?product=10461>, 1st July 2015.
 - [13] U. Müller, H.J. Timpe, K.G. Häusler, K. Peters, R. Wagner, Lichtinitiierte polymer- und polymerisationsreaktionen. 36. Mitt.: photovernetzung vinylgruppenhaltiger poly(dimethylsiloxane), *Acta Polym.* 41 (1990) 54–54-59.
 - [14] N. Barié, M. Rapp, H.J. Ache, UV crosslinked polysiloxanes as new coating materials for SAW devices with high long-term stability, *Sens. Actuators B: Chem.* 46 (1998) 97–103.
 - [15] F.M. Weiss, X. Zhao, P. Thalmann, H. Deyhle, P. Urwyler, G. Kovacs, et al., Measuring the bending of asymmetric planar EAP structures, *Proc. SPIE* 8687 (2013) 86871X.
 - [16] P. Urwyler, J. Köser, H. Schiff, J. Gobrecht, B. Müller, Nano-mechanical transduction of polymer micro-cantilevers to detect bio-molecular interactions, *Biointerphases* 7 (2012) 1–8.
 - [17] Y. Israëli, J. Cavezzan, J. Lacoste, Photo-oxidation of polydimethylsiloxane oils: II-effect of vinyl groups, *Polym. Degrad. Stabil.* 37 (1992) 201–208.
 - [18] J.E. Sader, J.W.M. Chon, P. Mulvaney, Calibration of rectangular atomic force microscope cantilevers, *Rev. Sci. Instrum.* 70 (1999) 3967–3969.
 - [19] W.C. Oliver, G.M. Pharr, Measurement of hardness and elastic modulus by instrumented indentation: Advances in understanding and refinements to methodology, *J. Mater. Res.* 19 (2004) 3–20.
 - [20] T. Töpfer, B. Osmani, F.M. Weiss, C. Winterhalter, F. Wohlfender, V.Y.F. Leung, et al., Strain-dependent characterization of electrode and polymer network of electrically activated polymer actuators, *Proc. SPIE* 9430 (2015) 94300B.
 - [21] T.C. Hodge, S.A. Bidstrup-Allen, P.A. Kohl, Stresses in thin film metallization, *IEEE Trans. Comp. Packag. Manuf. Technol.* A 20 (1997) 241–2250.
 - [22] D.A. Panchuk, S.L. Bazhenov, A.V. Bolshakova, L.M. Yarysheva, A.L. Volynskii, N.F. Baakev, Correlation between structure and stress-strain characteristics of metallic coatings deposited onto a polymer by the method of ionic plasma sputtering, *Polym. Sci. Ser. A* 53 (2011) 211–216.
 - [23] V.K. Pamula, A. Jog, R.B. Fair, Mechanical Property Measurement Of Thin-film Gold Using Thermally Actuated Bimetallic Cantilever Beams, *Nanotech.* vol. 1, Nano Science and Technology Institute, Duke University, US, 2001, pp. 410–413.
 - [24] J. Köser, S. Gaiser, B. Müller, Contractile cell forces exerted on rigid substrates, *Eur. Cell. Mater.* 21 (2011) 479–487.
 - [25] M. Lallart, C. Richard, P. Sukwisut, L. Petit, D. Guyomar, N. Muensit, Electrostrictive bending actuators: modeling and experimental investigation, *Sens. Actuators A: Phys.* 179 (2012) 169–177.
 - [26] F.M. Weiss, T. Töpfer, B. Osmani, C. Winterhalter, B. Müller, Impact of electrode preparation on the bending of asymmetric planar electro-active polymer microstructures, *Proc. SPIE* 9056 (2014) 905607.
 - [27] V. Racherla, An electromechanical model for characterizing sensing and actuating performance of unimorphs based on plain dielectric polymers, *Sens. Actuators A: Phys.* 168 (2011) 343–350.
 - [28] G.G. Stoney, The tension of metallic films deposited by electrolysis, *Proc. R. Soc. London Ser. A* 82 (1909) 172–175.
 - [29] R.A. Swalin, *Thermodynamics of Solids*, John Wiley & Sons, New York, 1972.
 - [30] P.J. Launer, *Infrared Analysis of Organosilicon Compounds: Spectra-structure Correlations*, Laboratory for Materials, Inc. Burnt Hills, New York, 1987, pp. 12027.
 - [31] A.D. Delman, M. Landy, B.B. Simms, Photodecomposition of polymethylsiloxane, *J. Polym. Sci. Part A: Polym. Chem.* 7 (1969) 3375–3386.
 - [32] G. Camino, S.M. Lomakin, M. Lazzari, Polydimethylsiloxane thermal degradation Part 1. Kinetic aspects, *Polymer* 42 (2001) 2395–2402.
 - [33] S.J. Blanksby, G.B. Ellison, Bond dissociation energies of organic molecules, *Acc. Chem. Res.* 36 (2003) 255–263.
 - [34] J.A. Dean, Section 4. Properties of Atoms, Radicals, and Bonds, *Lange's Handbook of Chemistry*, 15th ed., McGRAWHILL Inc., University of Tennessee, Knoxville, 1999, pp. 441–453.
 - [35] J.-L.P.Y. Israeli, J. Cavezzan, J. Lacoste, J. Lemaire, Photo-oxidation of polydimethylsiloxane oils: part I-effect of silicon hydride groups, *Polym. Degrad. Stabil.* 36 (1992) 179–185.
 - [36] Y. Israeli, J. Lacoste, J. Cavezzan, J. Lemaire, Photooxidation of polydimethylsiloxane oils and resins. IV-Effect of phenyl groups, *Polym. Degrad. Stabil.* 47 (1995) 357–362.
 - [37] M. Rogošić, H.J. Mencer, Z. Gomzi, Polydispersity index and molecular weight distributions of polymers, *Eur. Polym. J.* 32 (1996) 1337–1344.
 - [38] S. Al-Maawali, J.E. Bemis, B.B. Akhremitchev, R. Leecharoen, B.G. Janesko, G.C. Walker, Study of the polydispersity of grafted poly(dimethylsiloxane) surfaces using single-molecule atomic force microscopy, *J. Phys. Chem. B* 105 (2001) 3965–3971.
 - [39] V.-M. Graubner, R. Jordan, O. Nuyken, B. Schnyder, T. Lippert, R. Kötz, et al., Photochemical modification of cross-linked poly(dimethylsiloxane) by irradiation at 172 nm, *Macromolecules* 37 (2004) 5936–5943.
 - [40] S.H. Kim, E.A. Cherney, R. Hackam, Effect of Dry Band Arcing on the Surface of Rtv Silicone Rubber Coatings, *International Symposium on Electrical Insulation, IEEE*, Baltimore MD, USA, 1992, pp. 237–240.
 - [41] J.E. Mark, J.L. Sullivan, Model networks of end-linked polydimethylsiloxane chains. I. Comparisons between experimental and theoretical values of the elastic modulus and the equilibrium degree of swelling, *J. Chem. Phys.* 66 (1977) 1006–1011.
 - [42] C. Löwe, X. Zhang, G. Kovacs, Dielectric elastomers in actuator technology, *Adv. Eng. Mater.* 7 (2005) 361–367.
 - [43] P. Kovacic, G. Sforazzini, A.G. Cook, S.M. Willis, P.S. Grant, H.E. Assender, et al., Vacuum-deposited planar heterojunction polymer solar cells, *ACS Appl. Mater. Interfaces* 3 (2010) 11–15.
 - [44] C.M. Spillmann, J. Naciri, B.D. Martin, W. Farahat, H. Herr, B.R. Ratna, Stacking nematic elastomers for artificial muscle applications, *Sens. Actuators A: Phys.* 133 (2007) 500–505.
 - [45] S.T. Choi, J.O. Kwon, F. Bauer, Multilayered relaxor ferroelectric polymer actuators for low-voltage operation fabricated with an adhesion-mediated film transfer technique, *Sens. Actuators A: Phys.* 203 (2013) 282–290.

Biographies



Tino Töpfer studied at the Albert-Ludwigs University of Freiburg i. Br. and received his diploma degree in physics in 2011. From 2010 to 2011 he prepared his diploma thesis specialized on semiconductor lasers at the Fraunhofer Institute of solid state physics (IAF) in Freiburg where he continued his work after graduation as a research assistant till 2012. Since 2013 he is working towards his PhD degree in physics on the realization of polymer thin films and their characterization by optical means at the Biomaterial Science Center (BMC, University of Basel). As a member of the Nano-Tera founded project "Smartsphincter" he aims for biomedical applications such as implantable low-voltage actuators.



Bekim Osmani did his B.Sc. in Mechanical Engineering and received his M.Sc. in Biomedical Engineering and Robotics at the Swiss Federal Institute of Technology in Zurich (ETHZ) in 2002. He worked from 2002 until 2004 as a scientific assistant at the Institute of Mechatronics at the Zurich University of Applied Sciences in Winterthur. After several years of experience in industry, he is currently working towards his PhD degree in Nanoscience on the fabrication and characterization of dielectric elastomer actuators for medical implants at the University of Basel.



Florian Weiss received his B.Sc. in Chemistry and Molecular Science at the University of Berne Switzerland in 2009, where he continued his studies in Inorganic Chemistry and Materials Science until 2011 when he accomplished his Master degree. After working 6 months in a collaboration project of the University of Bern and BASF he started his PhD at the University of Basel. Currently he is still at the Biomaterials Science Center (BMC, University of Basel) in collaboration with the Empa Dübendorf, Research Center Jülich and the Technical University of Denmark (DTU) to attain his PhD degree in Nanoscience working on MEMS/NEMS mimicking muscles.



Christian Bippes holds a diploma in Biochemistry from the University of Bayreuth, Germany, and received a PhD from the University of Technology Dresden, Germany, in 2009. From 2009 until 2013 he worked as a post-doc at the University of Technology Dresden, Germany, and ETH Zürich, Switzerland. Currently, he is working as application engineer at Nanosurf AG located in Liestal, Switzerland.



Vanessa Leung holds a B.Sc. (Hons.) in Physics (2001) from Massey University, New Zealand, and a Ph.D. (2006) jointly from the Australian National University, Australia, and the University of Bonn, Germany. This was followed by university research on experiments in atomic, molecular and optical (AMO) physics in Europe and the USA. Since 2012 she has focused on applying physics to technological problems, and doing science at the intersection of academia and industry. As part of a technology initiative between the University of Twente and Philips Lighting in the Netherlands, she used nano-photonics to develop more efficient white LED lighting. She is currently team leader of the Nano-Tera project on Artificial Muscles at

the University of Basel.



Bert Müller obtained MSc in Physics and MSc in English from the Dresden University of Technology, and a PhD in experimental physics, University of Hannover, Germany. He was postdoc at Physics Department of Paderborn University, Germany and Feodor Lynen-Fellow at the Physics Department of EPF Lausanne, Switzerland. It followed leading positions within the ETH domain, i.e. at the Physics Department of ETH Zürich, Swiss Institute for Materials Testing and Research, Materials Department and Information Technology and Electrical Engineering Department of ETH Zürich. Since 2001, Bert Müller teaches at the Physics Department of ETH Zürich as 'Privatdozent in Experimentalphysik'. Since 2006 he is Thomas Straumann-Professor for Materials Science in Medicine at the Medical Faculty of the University in Basel. Teaching experiences include the Medical Faculty in Bern (Biomaterials and Materials Science), Dental School of the University of Basel (Dental Materials and Technologies) and Science Faculty (Nanosciences and Surface Science). Currently, he is director of the Biomaterials Science Center and leads a research team of almost 30 scientists from several disciplines. The research activities include high-resolution X-ray imaging, biomaterials science and engineering, and artificial muscles. He is author of more than 200 scientific publications including patents.

2.5 Time resolved plasmonics on self-assembled hetero-nanostructures for soft nanophotonic and electronic devices

Spectroscopic ellipsometry constitutes a unique technique to access *in situ* optical properties, plasmonic fingerprints and film topography simultaneously.

In situ ellipsometry can reach sub-nanometer resolution through clever combination with real-space techniques.

Specifically tailored for thermal evaporation bi-functional thiol-terminated PDMS (SH-PDMS) serves as self-assembled adhesion monolayer for gold.

Functionalized organic species can substantially improve the homogeneity and stability of Au films deposited on an elastomer such as PDMS.

Nanometer-thin Cr-wrinkles can be tailored in real-time according to their plasmonic response.

Cr-wrinkles adhesion interlayer for gold reduces the percolation threshold remarkably by a factor of five to a confluent gold film above 4.4 nm.

Submitted to Nature Photonics

Time-resolved plasmonics on self-assembled hetero-nanostructures for soft nanophotonic and electronic devices

Tino Töpfer,^a Samuel Lörcher,^b Bekim Osmani,^a Vanessa Leung,^a Hans Deyhle,^a Thomas Pfohl,^a and Bert Müller^a

^a *Biomaterials Science Center, Department of Biomedical Engineering, University of Basel, Gewerbestrasse 14, 4123 Allschwil Switzerland*

^b *Chemistry Department, University of Basel, 4056 Basel, Switzerland*

Abstract

Soft, transparent, and biocompatible hetero-nanostructures based on electrically activated polymers are applicable to bio-MEMs, nano-photonics, micro-optics, and flexible electronics. Combining self-assembly with real-time tailoring of the electronic and optical properties of the nanometer-thin heterostructures allows the manufacturing process to be precise and low-cost. We use real-time spectroscopic ellipsometry (SE) to on-line monitor the optical properties, morphology, and nano-photonic fingerprints of Au nanoparticles and film formation on self-assembled polydimethylsiloxane-based (PDMS) nanostructures. Bi-functionalized thiol-PDMS tailored for molecular beam deposition serves as a self-assembled adhesion monolayer for Au. Suppressed plasmonic activity indicates homogeneous Au-growth through localized Au-thiol-PDMS bonding. Both, thiol-PDMS and isotropic wrinkled chromium-(Cr)-PDMS-nanostructures enhance a confluent assembly of evaporated Au contrary to the Au-cluster formation on untreated PDMS films. Our specifically tailored hetero-nanostructures based on thiol-PDMS or wrinkled Cr-PDMS adhesion layers are promising for low-voltage devices in soft electronics and nano-photonics, such as artificial muscles and adjustable photonic gratings.

Keywords: *Surface plasmonics, thiol-polydimethylsiloxane synthesis, self-assembled monolayers, soft hetero-nanostructures, organic molecular beam deposition, spectroscopic ellipsometry, atomic force microscopy.*

Electronic and nanophotonic devices based on biocompatible polymers are of great interest for soft robotics, microfluidics, flexible optoelectronics and opto-fluidics, as well as biomimetic sensors and actuators. Polydimethylsiloxane (PDMS) is widely used in microfluidics¹, and due to its low cost, ease of fabrication, biocompatibility and optical transparency, recent efforts have also been made to extend its range of application. These efforts include hybrid devices involving CMOS technology², soft bioelectronics³, and low-voltage nanostructured, stacked actuators for smart medical implants⁴. In addition, there is an increasing demand for low-voltage actuators for other electrically activated elastomer-based applications such as tactile displays⁵, adaptable lenses⁵ or sensors⁶.

Plasmonics is an application-rich merging of photonics and electronics⁷ that allows, for example, the size and morphology of metallic hetero-nanostructures to be optically determined without the restrictions posed by the diffraction limit. Plasmonic oscillations can be tuned from the mid-infrared, especially of interest for ultrafast data transfer in telecommunications based on semiconducting composites⁸ down to UV-visible for biosensing applications⁹ based on Au nanostructures. Dynamic control of the plasmonic behavior of Au nanostructures is of current scientific interest due to their potential for optoelectronic devices such as photonic crystals, gratings, and waveguides^{10,11}. Shape control of Au nanostructures is also relevant for the development of biomimetic materials and printed electronics¹².

The combination of surface plasmons with a soft, electrically activated substrate such as PDMS offers the intriguing possibility of dynamically influencing plasmonic frequencies by manipulating the underlying polymer layer through structural and dimensional control. Recently, we have demonstrated the precise tailoring of molecular weight distribution and functionality of thermally evaporated PDMS thin films¹³ which allows PDMS layers in the nanometer regime to be fabricated by organic molecular beam deposition (MBD). The high degree of experimental control possible with MBD processing provides the opportunity to engineer surface plasmons *in situ* by subsequent thermal deposition of metallic nanoparticles on the PDMS film.

Through self-assembly, the thermally deposited metallic layer evolves from discontinuously arranged nanoparticles to a confluent thin film, a process we have on-line observed. We

fabricated thermally evaporated metal/PDMS nanostructures and monitored the temporal evolution of surface plasmons with spectroscopic ellipsometry (SE). Collective electronic oscillations induced by the incident SE beam yield surface plasmon resonances (SPR) used to on-line track intrinsic structural properties of the hetero-nanostructures such as size, shape, and composition.

Due to the low PDMS surface energy¹⁴ adhesion promoters such as Cr are required to generate stable compliant Au-PDMS composites. Here, SE provides the on-line feedback required to allow for the controlled formation of wrinkled Cr-PDMS heterostructures. To circumvent the mechanical stiffness of Cr layers, we also synthesized bi-functionalized thiol-PDMS (SH-PDMS) with tailored molecular weights for MBD to serve as soft self-assembled adhesion monolayer. Suppressed plasmonic activity in the visible indicates homogenous Au-growth on both Cr and thiol-PDMS adhesion layers, compared to Au-cluster formation on pure PDMS. Remarkably, we determined that the percolation threshold for the first confluent monolayers is reduced to a few nanometers of Au film thickness.

By combining self-assembly with on-line examination of the plasmonic fingerprints, topographical structure, and optical properties of Au-nanoparticles on PDMS-based nanostructures, we have developed a procedure to optimize multilayer plasmonic structures for nanophotonic and electronic applications. In addition, by replacing Cr with bi-functionalized thiol-PDMS as a nanometer-thin adhesive, we have increased the flexibility of the multilayers, anticipating them to be used for flexible applications such as soft plasmonic nanosensors in biosensing or stretchable nanoelectronics.

Thermally evaporated soft hetero-nanostructures

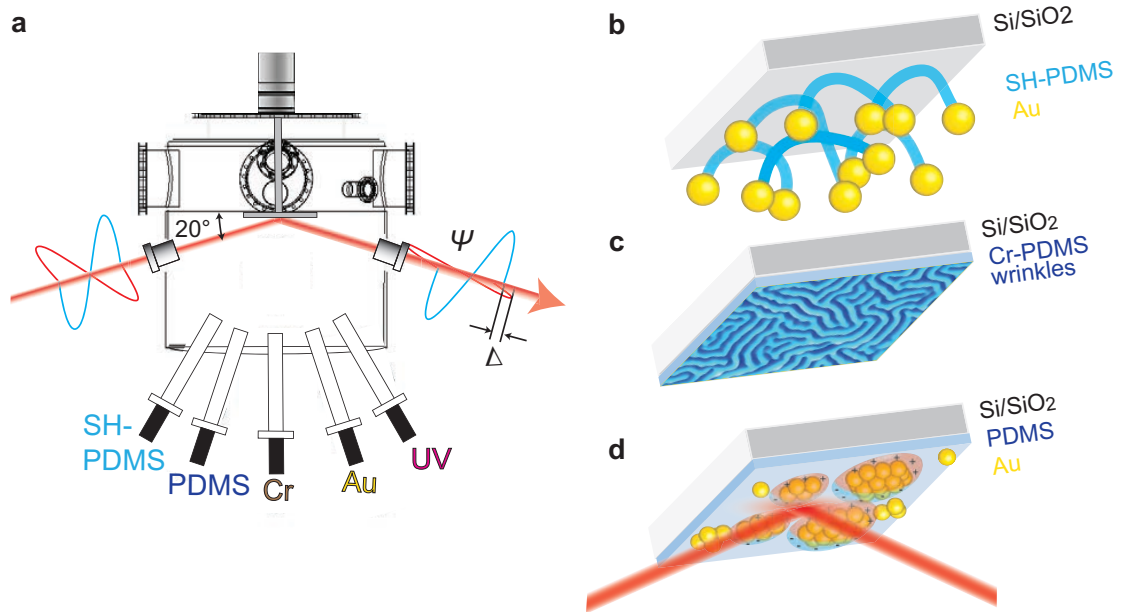


Figure 1 | Scheme of the thin film preparation. **a**, Cross-section of organic molecular beam deposition setup for the fabrication of soft multilayer nanostructures under ultra-high vacuum conditions. *In situ* spectroscopic ellipsometry at an incident angle of 20° simultaneously monitors film thickness, optical properties, and plasmonics. Coherent electron oscillations occur if the nanoparticles become excited at resonance frequency. Representative thermally grown soft nanostructures: **b**, self-assembled Au-particles covalently bound to a bi-functional, thio-terminated PDMS monolayer; **c**, wrinkled Cr/PDMS; **d**, Au-nanoparticles are thermally deposited on PDMS membrane.

Besides the optical properties real-time spectroscopic ellipsometry (SE) detects nano-photon fingerprints of Au-nanoparticles, which are directly related to size, surface coverage, and dielectric function of nanoparticles. Due to the incident $4 \times 10 \text{ mm}^2$ -beam dimension the ellipsometry setup monitors nanostructures on macroscopic area. A representative cross-section of the ultra-high vacuum (UHV) fabrication and *in situ* measurement configuration is shown in Figure 1a (for details see Methods). We first investigate the self-assembly of a thermally evaporated bi-functional thio-terminated PDMS monolayer, abbreviated SH-PDMS.

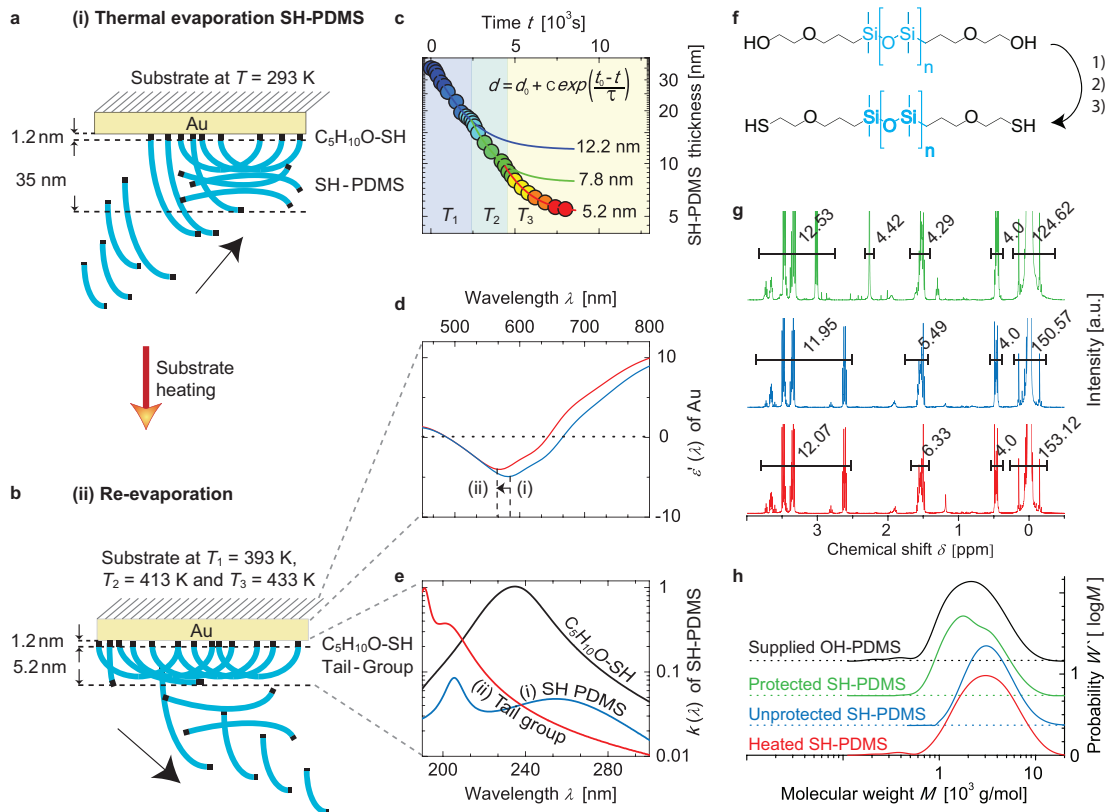


Figure 2 | Self-assembly of bi-functional thiol-terminated PDMS on Au. **a**, Self-assembly and stacking schemes of (i) thermally evaporated SH-PDMS chains consisting of the $(CH_2)_3-O-(CH_2)_2-SH$ -group (black) and the dimethylsiloxane repeating units (blue) on Au substrate. **b**, Monolayer of bi-covalently bound SH-PDMS chains to Au after (ii) re-evaporation of excess molecules. **c**, Time-resolved desorption of SH-PDMS chains at substrate temperatures 393 K (blue), 413 K (green) and 433 K (yellow). **d**, Blue shift of surface plasmon resonance peak of the Au substrate induced by SH-PDMS coating. **e**, Extinction coefficient of the bi-layer model for SH-PDMS consisting of the $(CH_2)_3-O-(CH_2)_2-SH$ -group (black) and the tail group (red) changing the optical properties during re-evaporation. **f**, Synthetic route to yield the bi-functional, thiol-terminated PDMS (SH-PDMS) from bi-hydroxyl-terminated PDMS (OH-PDMS) with 1) trifluoromethanesulfonic anhydride at -20 °C for 3 h; 2) potassium thioacetate at 25 °C for 12 h; 3) $LiAlH_4$ at 0 °C for 4h.

g, Nuclear magnetic resonance spectra of protected bi-functional thiol-terminated polydimethylsiloxane (green), unprotected bi-functional thiol-terminated polydimethylsiloxane (blue) and bi-functional thiol-terminated polydimethylsiloxane (red), thermally treated at a temperature of 443 K (150 °C) for a period of 40 min. **h**, The corresponding molecular weight distributions obtained from gel permeation chromatography traces recorded in CHCl_3 are presented. The black curve represents bi-functional hydroxyl-terminated polydimethylsiloxane (OH-PDMS) as supplied.

Many approaches to precisely control nanoscale architectures are based on the high affinity of thiols to Au¹⁵. Figure 2a sketches the thermal evaporation and assembly of synthesized SH-PDMS on Au at an evaporation temperature of 413 K (120 °C). The dielectric function is determined using a bi-layer Tauc-Lorentz model¹⁶. A 1.2 nm-thin, surface-near layer with a refractive index of $n = 1.75$ at $\lambda = 656$ nm combined with a superposed layer with a refractive index of $n = 1.5$ at $\lambda = 656$ nm fits to the experimentally obtained spectroscopic Ψ - and Δ -values. The derived thickness of 1.20 nm corresponds to the $(\text{CH}_2)_3\text{-O-(CH}_2)_2\text{-SH}$ (2-propoxyethyl-1-thiol) terminate group with an expected length of 1.04 nm. The refractive index of the overlying layer relates to the dimethylsiloxane repeating units of SH-PDMS superimposed with the optical properties of free $(\text{CH}_2)_3\text{-O-(CH}_2)_2\text{-SH}$ groups. Re-evaporation of the adsorbed, free SH-PDMS chains exposes the self-assembled monolayer (SAM) of SH-PDMS on Au. Figure 2c presents the stepwise reduction in film thickness for increased substrate temperatures related to SH-PDMS desorption. Van-der-Waals interactions of the methyl side-groups dominate intermolecular interactions between SH-PDMS on the substrate and in the crucible melt as well¹³. Therefore, an entire desorption of free SH-PDMS is assumed for substrate temperatures above the evaporation temperature. The S-Au bond strength of 167 kJ/mol¹⁵ enables substrate heating up to 433 K (140 °C) avoiding S-Au bond fracture. Adjusting the substrate temperature well above 413 K, the SH-PDMS film thickness asymptotically diminishes to 5.2 nm. The thickness of the surface near $(\text{CH}_2)_3\text{-O-(CH}_2)_2\text{-SH}$ group layer remained constant. This behavior indicates a SAM with ordered, covalently linked SH-PDMS. According to literature, the peak molecular weight of linear PDMS

evaporated at 413 K is 1,600 g/mol¹³ corresponding to a chain length of about 9.5 nm¹⁷. Assuming the characteristic 30° tilting angle of self-assembled alkene thiols¹⁵ a SAM thickness of 8.2 nm is calculated. This value does not match the experimentally determined layer thickness of 5.2 nm. During re-evaporation the distinct UV-absorption of the (CH₂)₃-O-(CH₂)₂-SH group around a wavelength of 240 nm¹⁸ reduces within the tail-group layer, see Figure 2e. In combination with the terminate SAM-thickness of 5.2 nm this implies bended, covalently double-bonded SH-PDMS chains on Au as residual after re-evaporation. The evaporation of 13.3 nm-long SH-PDMS chains at a evaporation temperature consistent with the substrate temperature of 443 K leads to a SAM-thickness of 7 nm. Hence, SH-PDMS SAM on gold can be precisely tailored via substrate temperature.

Another source of information are SPRs within the dielectric function of the underlying Au, determined by the dielectric properties of the environment¹⁹. The covalent S-Au bonding induces a red shift of the SPR peak during thermal deposition as the refractive index of the environment increases²⁰. However, we do observe a distinct blue shift of SPR from 590 to 580 nm during the re-evaporation process, *cf.* Figure 2d. This experimental observation rather relates to the structural transition from the Au film to nanoparticles as the result of the substrate heating²¹. Thus, the consideration of the structural changes is crucial to draw conclusions on the formation process of Au/SH-PDMS nanostructures by means of SE.

The synthesis of SH-PDMS from bi-functional hydroxyl-terminated polydimethylsiloxane (OH-PDMS) is described in Methods and schematically displayed in Figure 2f. The diagrams of Figure 2 f,g present nuclear magnetic resonance (NMR) and gel permeation chromatography data complying with the synthesis steps of SH-PDMS. Here, we emphasize the successful design of SH-PDMS molecular weight distribution (MWD) for the thermal evaporation. Based on the thermal degradation temperature of 443 K (150 °C) for thiol-groups²², the molecular weights of linear SH-PDMS to evaporate are limited to about 3,000 g/mol¹³. The synthesized SH-PDMS (see blue-colored curve in the diagram of Figure 2g) reveals a number average molecular weight M_n of 2,700 g/mol and thus, offers a broad range of the MWD to be evaporated. After evaporation under UHV conditions at a temperature of 443 K (150 °C) (red-colored curve in Figure 2g) a slight

shift to a number average molecular weight M_n of 2,800 g/mol is found. Proven within the NMR spectra, a negligible amount of di-sulfide links prolongs the SH-PDMS chains, which makes the SH-PDMS suitable for thermal evaporation.

Stacked mirrored, as schematically displayed in Figure 1b, the SH-PDMS self-assembly monolayer (SAM) is intended for localized covalent bonding of Au nanoparticles. This SH-PDMS/Au architecture will be useful to realize future adhesive and soft nano-electronics on nanometer-thin PDMS membranes.

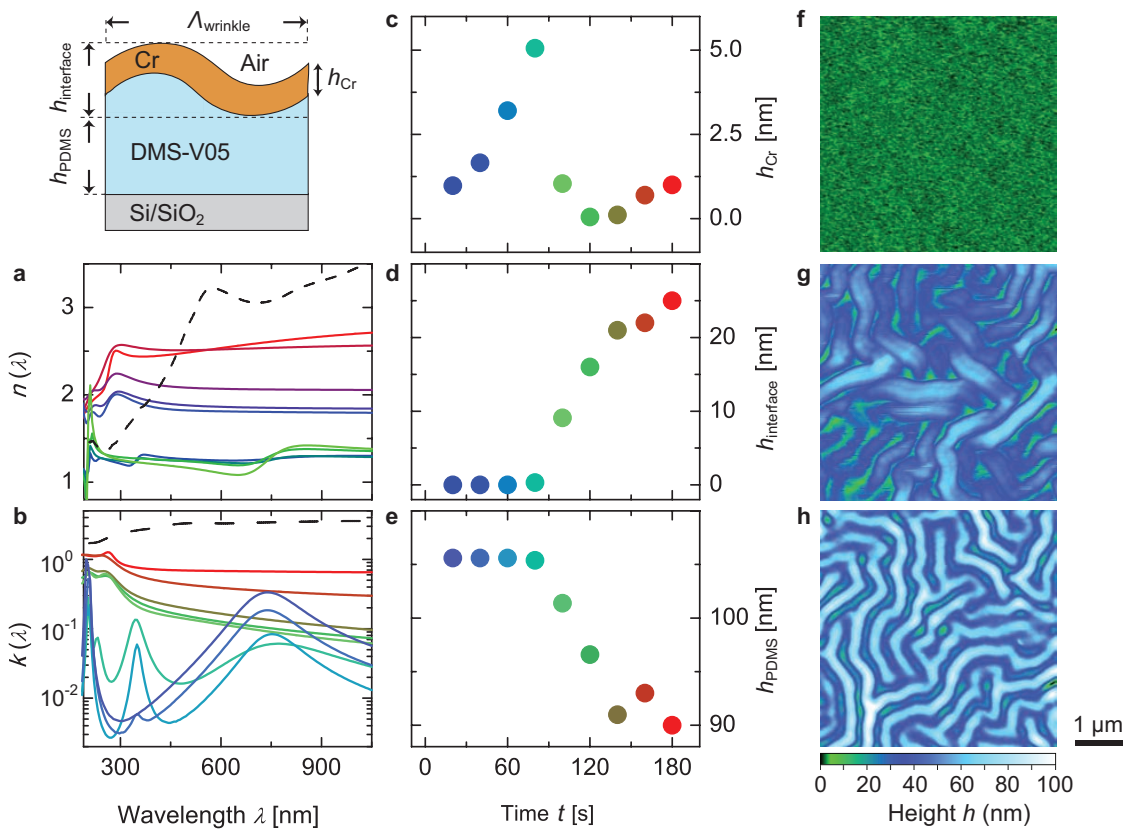


Figure 3 | Morphology evolution and plasmons of isotropic Cr/PDMS-nanostructures.

a, Spectroscopic data of refractive index n and **b**, extinction coefficient k data of thermally deposited Cr on UV-cured PDMS (DMS-V05) is shown for growth times between 20 and 180 s (blue to red) with 20 s intervals. The dashed line corresponds to Cr bulk values²³. The ellipsometry model (inset) consists of three layers: **c**, the Cr film with thickness h_{Cr} , **d**, a Cr/PDMS compound layer with thickness $h_{interface}$, gradually changing the optical properties

from Cr to that of **e**, the PDMS film with thickness h_{PDMS} . Atomic force microscopy scans reveal the morphological transformation from **f**, a flat PDMS film with surface roughness of 0.7 nm to **g**, a wrinkled Cr-PDMS surface at its terminal stage with a wrinkle periodicity of 470 nm. **h**, The morphology in equilibrium measured two weeks after preparation.

Alternatively, a matured approach to retrieve cohesion between thin Au films and soft PDMS membranes is the application of nanometer-thin Cr films. The additional metal interlayer, however, induces stiffening. Fabricated as pre-stretched wrinkled microstructure, Cr-PDMS can retrieve some flexibility under strain²⁴. PDMS pre-stretching to build oriented wrinkles is difficult to manage with the nanometer-thin PDMS membranes. Spontaneous, isotropic formation of wrinkles can be induced through heating during metal deposition²⁵. During the deposition experiment the evaporator's infrared (IR) radiation heats the PDMS membrane. Figure 3 shows a color-coded time sequence during Cr deposition. The tri-layer model applied to the ellipsometer data allows distinguishing between the flat Cr film with height h_{Cr} and the wrinkled Cr-PDMS interface layer with height $h_{\text{interface}}$. This model is justified, because the surface roughness of the PDMS film, determined by ellipsometry, remains below the value of (0.7 ± 0.1) nm, as determined by related AFM images, see Figure 3f. The graphs in Figure 3c,d,e elucidate the onset of wrinkle formation 80 s after the deposition started. The linear Cr deposition rate goes with the reducing PDMS film thickness h_{PDMS} , proving the formation of the wrinkled interface layer. We assume that a confluent Cr film forms, which is associated with increasing IR-light shielding. Subsequently, the PDMS film relaxes evolving isotropic wrinkles, a scenario supported by the on-line measurement of the refractive index $n(\lambda)$ and extinction coefficient $k(\lambda)$ data, cf. Figure 3a,b, that reveal SPR at a wavelength of 740 nm after 20 s deposition and a shift to 800 nm after 80 s deposition. This experimentally observed redshift implies the formation of Cr nanoparticles. Delocalized electrons of the NIR Drude-band in the extinction spectra occur at deposition times above 80 s. This indicates a coalescence of observed Cr nanoparticles for films thicker than 5 nm. This phase transition to confluent Cr films on PDMS is twice the one on C(100)²⁶. An additional resonance peak in the extinction spectra arises at a wavelength of 260 nm for deposition exceeding 80 s.

The corresponding refractive index at this wavelength is larger than that of bulk Cr (dashed black line) for the thicker films. We link this absorbance feature rather to the Cr microstructured morphology than to Cr's dielectric function, supported by the AFM image in Figure 3g. Isotropic wrinkles depict the terminate Cr-PDMS heterostructure topography. Fourier transformation of a series of images exhibits a wrinkle period of $\Lambda_{\text{wrinkle}} = (470 \pm 20)$ nm. This microstructured surface with dimensions in the range of the incident light wavelength can fulfill the surface plasmon excitation condition as published for periodic silver patterns on elastomers²⁷. A long-term relaxation process of the Cr/PDMS heterostructure is demonstrated by the AFM image in Figure 3f obtained two weeks after deposition. The Fourier transform also exhibits a wrinkle period (470 ± 20) nm, but the wrinkle shape evolves from a sinusoidal to a top-hat profile with average wrinkle amplitudes increasing from 50 nm to 80 nm.

Au formation on soft hetero-nanostructures

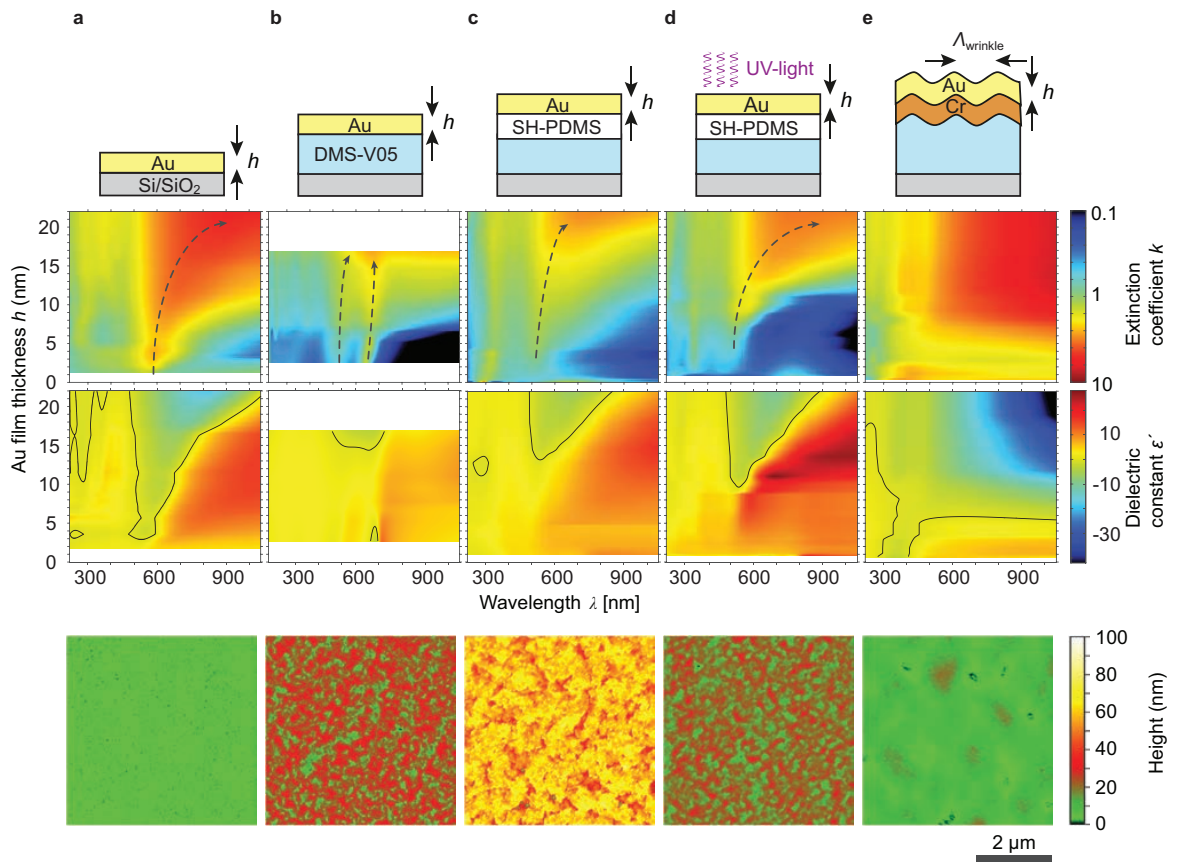


Figure 4 | Plasmonics of growing Au nanoparticles on hetero-nanostructures. Film-thickness-dependent spectroscopy of the extinction coefficient k (first row) and the real part ϵ' of the dielectric function (second row) are shown for thermally evaporated Au nanoparticles on **a**, Si/SiO₂; **b**, UV-cured thermally evaporated DMS-V05; **c**, thermally evaporated SH-PDMS; **d**, SH-PDMS deposition during UV-radiation (termed as UVSH-PDMS); **e**, isotropic wrinkled Cr-PDMS nanostructures. The color code of the extinction coefficient k is displayed logarithmically and the real part ϵ' of the dielectric function linearly. Dashed arrows indicate the occurrence and shift of surface plasmon resonance peak frequencies within the extinction coefficient spectra. The boundary for which the dielectric constant appears $\epsilon' < 0$ is marked as a black line. This event is connected to delocalized electron oscillations, which occurs in the NIR Drude-band. The final Au film morphologies on the corresponding hetero-nanostructures are characterized with atomic force microscopy (third row).

The multilayer hetero-nanostructures investigated are schematically depicted in Figure 4. Figure 4a,b shows the Au deposition on SiO₂ and on the UV-cured PDMS membrane 98 nm-thin. Based on literature^{21,28}, the related ellipsometry measurements serve as reference for Au deposited on rigid and soft substrates. The schemes in Figure 4c,d,e illustrate the Au formation on custom-built soft nanostructures. The ellipsometry gives rise to the dielectric constant ϵ' and the extinction coefficient k spectra of Au films up to 22 nm thick. The ellipsometer-derived values for the film thickness are based on the Drude-Lorentz oscillators model and validated via AFM measurements at step edges. Furthermore, the AFM images, as represented in the third row of Figure 4, confirm the ellipsometer-derived data on surface roughness. The employed Lorentz oscillators excellently adapt to the plasmonic absorption bands resulting in mean square errors well below unity for the modeled hetero-nanostructures (example data in supplemental Figure 6). UV-interband transitions from d -valance to s - and p -bands above the Fermi level of Au occur at resonance energies of 3.05 and 4.3 eV (406 and 288 nm), respectively, modeled by two Lorentz dispersions²⁹. Further discussions are based on the intrinsic property of Au nanoparticles having

plasma frequencies in the range of visible light. Local heating owing to plasmon resonance absorption can be neglected. A radiation intensity of 19 W cm^{-2} as used for laser-based selective photo-thermal cancer therapy³⁰ exceed the one of our setup with a diffuse halogen/deuterium lamp by five orders of magnitude. Thus, SE provides a sensitive but non-invasive characterization technique without influencing the intrinsic properties of the nanostructures.

First, the deposition of Au on SiO_2 is discussed. One SPR, consisting of two Lorentz oscillators (Figure 8e), exhibits a redshift and broadens with increasing average film thickness. For films thicker than 16 nm the second oscillator evolves into the NIR Drude-band (Figure 8e). The redshift of the SPR in the extinction spectrum goes along with dielectric constant ϵ' changes from positive to negative explained by the coalescence of metal nanoparticles and relates to localized free electrons. The percolation threshold can be defined as the insulator-to-metal transition (IMT) and implies the delocalized free electrons for $\epsilon' < 0$ in the NIR³¹. For Au/ SiO_2 the IMT is observed for films thicker than (20 ± 0.5) nm. Höver *et al.* presented an IMT for Au/ SiO_2 already for 8 nm-thin Au films³². The analysis is based on ϵ' -shifts at a wavelength of 20 μm , for which the transition behavior is increasingly pronounced and occurs for thinner Au layers. The IMT analysis based on ϵ' (1050 nm), however, does allow for comparisons among the hetero-nanostructures presented in Figure 4.

Second, we consider Au on a UV-cured PDMS membrane, illustrated in Figure 4b. Two main SPRs within the extinction spectrum at wavelengths of 540 and 650 nm for 2.7 nm-thin films are observed. Using selected deposition times, as given in Figure 7 of the supplemental section, the evolution of the SPRs can be followed in detail. Increasing the film thickness, these SPRs redshift and merge to one peak. Simultaneously a third SPR band in the NIR develops above 10 nm Au thickness. Although the blueshift of SPRs with increased particle height counters the redshift of the lateral growth, it has been stated that the lateral particle size dominates the shift of SPRs²¹. The SPR absorption splits into two bands for elongated nanometer-sized clusters³³. The detected SPRs at a film thickness of 2.7 nm suggest clusters with a lateral aspect ratio of 1.9. The third resonance may be due to the coalescence with increasing aspect ratio from 1.9 to 4.0 for 16.7 nm-thin Au³³. The analysis of related AFM images (Figure 7e,f in Supplemental) reveals an

aspect ratio of (2.1 ± 0.5) , a significantly smaller value for the terminal film thickness. Thus, a contribution of Au multipoles coalescing to distances below a few nanometer should be considered, which likewise splits and redshifts SPRs³⁴. Hence, to extract shape, size, and distance of Au islands *in situ* from multiple SPRs in the SE data, the predominant growth mode needs to be classified by a real-space imaging technique.

Compared to islanding on pure PDMS membranes, SH-PDMS promotes Au adhesion. As illustrated in Figure 4c one SPR is detected splitting up into two Lorentz oscillators for films above 4 nm. The IMT for Au/SH-PDMS was extrapolated to a film thickness of (25 ± 1) nm. The onset for localized electron oscillations at a SPR wavelength of 633 nm is derived already for Au films (15 ± 1) nm thin. To shed light on the Au islanding, the experimental data derived from ellipsometry are plotted for the changing growth regimes in Figure 5. We know that the Au evaporator provides a constant deposition rate, but for the first monolayers the ellipsometry measurement leads to a three to four times larger growth rate than expected. This phenomenon can be described by the relatively low surface energy of PDMS, which promotes nucleation of deposited Au adatoms known as the Volmer-Weber growth³⁵. With increasing Au cluster density the probability of coalescence enlarges. At a specific mean Au coverage, the percolation threshold will be reached and further deposition will result in a monolayer of Au clusters, schematically represented in Figure 5a. Herein, we determine the percolation threshold from the intersection of the ellipsometry-derived deposition rate h' with the expected mean deposition rate d' . For Au/SH-PDMS the percolation threshold corresponds to (24 ± 1) nm in agreement with the IMT value. The comparable value of (22 ± 1) nm for Au/PDMS suggests similarities in the Au nanocluster formation.

The distinct feature in extinction absorbance, i.e. a band around a wavelength of 280 nm for all Au thicknesses investigated, is represented in Figure 4c and associated with the $(\text{CH}_2)_3\text{-O-}(\text{CH}_2)_2\text{-SH}$ -group of SH-PDMS. This absorption feature indicates an entangled layer of Au and SH-PDMS. The comparably low Van-der-Waals interactions between free SH-PDMS chains enable their flexible arrangement according to cohesive forces of covalently attached Au adatoms towards Au nanoclusters assembly similar to the growth on pure PMDS. The related AFM images

exhibit a roughness of (8.1 ± 1.0) nm, consistent with (7.9 ± 0.8) nm for Au/PDMS. Because the cohesive forces between Au atoms are smaller than the covalent S-Au bonds³⁶, the Au nanoclusters are well connected to SH-PDMS chains. They can form a conducting matrix of nanometer-size clusters.

To build an ordered, confluent Au monolayer on SH-PDMS, UV-radiation has been applied to the hetero-nanostructure subsequent to the deposition of the Au cluster monolayer. Cross-linked to the PDMS membrane the rearrangement of top-layer SH-PDMS chains is presumably suppressed. Such suppression may lead to the ordered Au localized through covalent S-Au bonds. In fact, the decrease of oscillations from localized electrons at a wavelength of 633 nm implies a reinforced homogeneous growth mode. Especially for films thinner than 8 nm the plasmonic activity of localized electrons is reduced by one order magnitude compared to Au/PDMS. In addition, the absorbance band at wavelengths between 280 and 300 nm is less pronounced for Au/UVSH-PDMS. This observation indicates an abrupt interface between Au and UVSH-PDMS. Although the IMT at a film thickness of (25 ± 1) nm is consistent with Au/SH-PDMS and Au/PDMS, the gained percolation threshold has been only (12 ± 1) nm (Figure 5c). The surface roughness obtained via AFM experiments corresponds only to (4.4 ± 0.3) nm for Au/UVSH-PDMS.

For Au deposition on wrinkled Cr/PDMS heterostructures the IMT arises for films thicker than (5.2 ± 0.3) nm (Figure 4e). The percolation threshold of (4.4 ± 0.3) nm (Figure 5c) is just below this value. SPRs in the visible range of the extinction spectrum are entirely suppressed. Above the percolation threshold, the extinction coefficient increases with respect to Au/SH-PDMS. It is related to the propagation of surface plasmon oscillations within the underlying Cr film. Another resonance in the UV-range of the extinction spectrum occurs at Au film thicknesses h as low as 0.7 nm. Centered at a wavelength of 320 nm, the absorbance peak exhibits a redshift as the deposition proceeds. This resonance can originate from the wrinkled Cr microstructures. The observed redshift correlates with the increase of the wrinkle's wavelength during Au deposition, as evidenced by the AFM images of Figure 4e. The isotropic wrinkles disappear and an Au film with a roughness of only (2.9 ± 0.2) nm remains. The relaxation of wrinkles is understood as pre-

stretching of the underlying elastic membrane due to the heat load during Au deposition³⁷. Thus, compared to Au/PDMS the percolation threshold is a factor of five smaller.

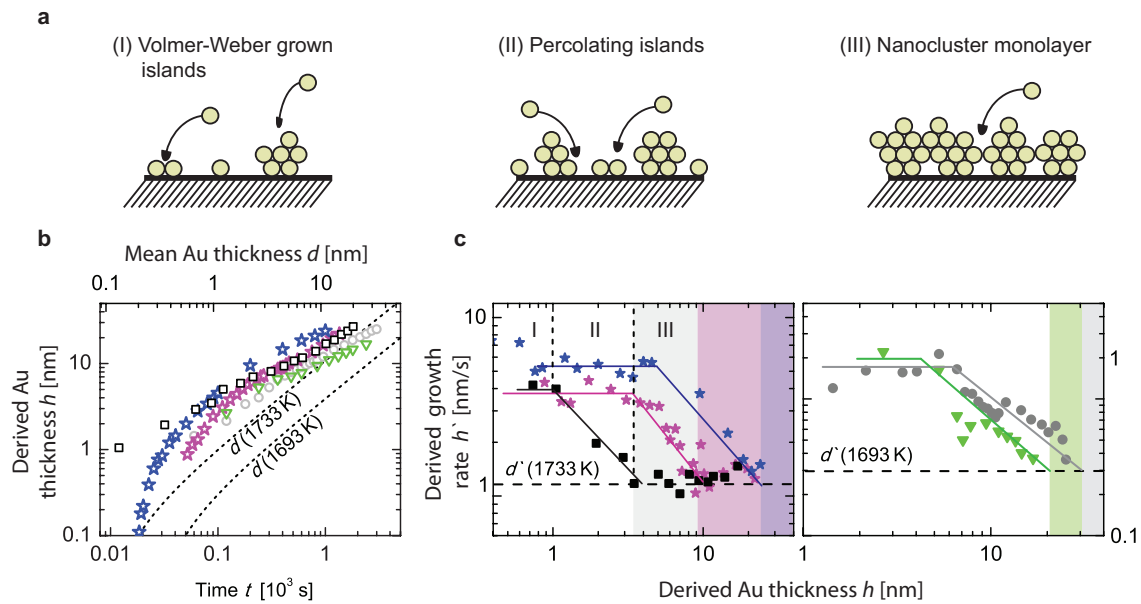


Figure 5 | Gold-nanoparticle percolation threshold. **a**, Schematics of Au film formation from islanding (3D Volmer-Weber) towards the assembly of a nanocluster monolayer are illustrated. **b**, The ellipsometry-derived Au film thickness h at representative time points for Au growth on Si/SiO₂ (grey circles), UV-cured thermally evaporated PDMS (green triangles), 7 nm-thin thermally evaporated SH-PDMS (blue stars), 7 nm-thin thermally evaporated SH-PDMS with synchronous UV-irradiation termed as UVSH-PDMS (violet stars), an isotropic wrinkled Cr-PDMS-nanostructure (black squares) is shown. Dotted lines illuminate the expected mean Au-thickness d as adjusted by the evaporator temperature correspondent to the top axis of the diagram. **c**, Ellipsometry-derived growth rates h' of Au on the presented hetero-nanostructures are shown. Expected mean growth rates d' for evaporation temperatures of $T = 1733\text{ K}$ and $T = 1693\text{ K}$ are marked as dashed lines. The proposed three growth phases are representatively marked for Au growth on Cr-PDMS wrinkles: (I) The 3D-pronounced formation of freestanding gold islands introduces higher growth rates than adjusted; (II) The percolation of Au nanoclusters directs the growth towards (III) 2D-assembly to first confluent cluster-monolayers. The percolation threshold to

ordered 2D-assembly is claimed as match between derived growth rate h' and the expected mean growth rate d' (colour shaded areas).

Conclusion

Organic and metal molecular beam deposition controlled via real-time spectroscopic ellipsometry paves the way to tailor multilayered metal/elastomer heterostructures of nanometer thickness. Because the analysis of optical properties and plasmonic fingerprints from ellipsometry bases upon models and serious assumptions, further input from complementary methods such as AFM is required. The present growth study also demonstrates that *in situ* ellipsometry can reach sub-nanometer resolution through clever combination with real-space techniques. For this reason, ellipsometry-based monitoring of growing, self-assembled layers with Au-S bonds and related soft hetero-nanostructures becomes a unique tool to quantitatively understand film formation processes.

Functionalized organic species can substantially improve the homogeneity and stability of Au films deposited on an elastomer such as PDMS. One can even retrieve compliance either by localized covalent Au-thiol bonds or thermally pre-stretched, nanometer-thin Cr, especially beneficial for future soft electronics. Elastic moduli gradients towards the underlying PDMS film can create anisotropic structures³⁸. The low-voltage DEA configuration of the soft heterostructures are anticipated for potential nanophotonic devices, including soft tunable gratings for nano-optics³⁹ and tunable plasmonic absorbers⁴⁰. Sensing and actuating can be achieved within one DEA heterostructure. The fabrication of biomimetic compliant sensors and actuators similar to human tissue is a key to realize artificial muscles⁴¹ and soft robotics.^{42,43}

Acknowledgements

The financial support of the Swiss National Science Foundation (project 200021-135496), of the nano-tera.ch initiative (project SmartSphincter), and of the Swiss Nanoscience Institute (SNI) for the AFM is gratefully acknowledged.

Supplementary material

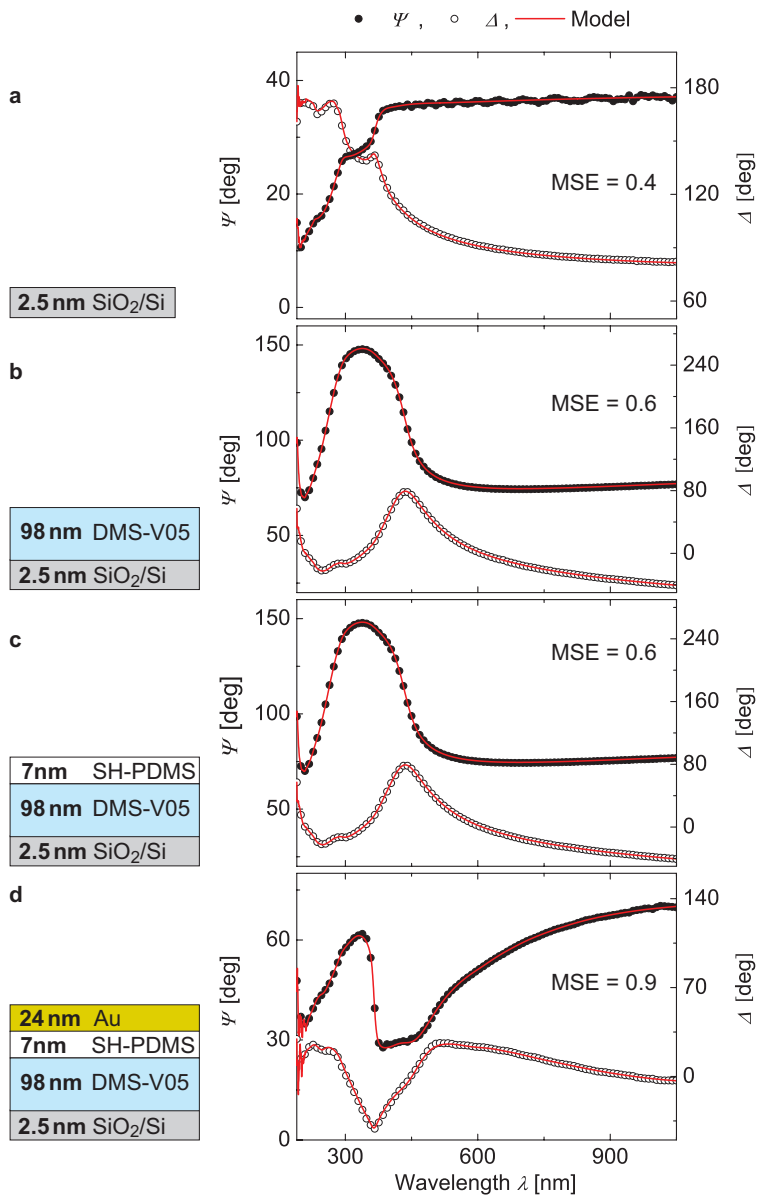


Figure 6 | Spectroscopic ellipsometry modeling of Au/PDMS hetero nanostructures.

Representative spectroscopic Ψ (filled triangles) - and Δ (open circles) spectra and proposed models (red line) match the optical properties of thermally evaporated hetero nanostructures:

- a**, Si(111)-substrate with 2.5 nm-thin native SiO₂ **b**, coated with thermally-evaporated and *in-situ* ultraviolet light-cured, 98 nm-thin DMS-V05 film **c**, coated with a 7 nm-thin SH-PDMS film **d**, coated with thermally-evaporated 24 nm-thin Au. The insets represent the ellipsometric model

used to fit the data. An interface layer between Au and SH-PDMS film as well as a surface roughness layer is included to obtain mean square errors (MSE) well below 1.

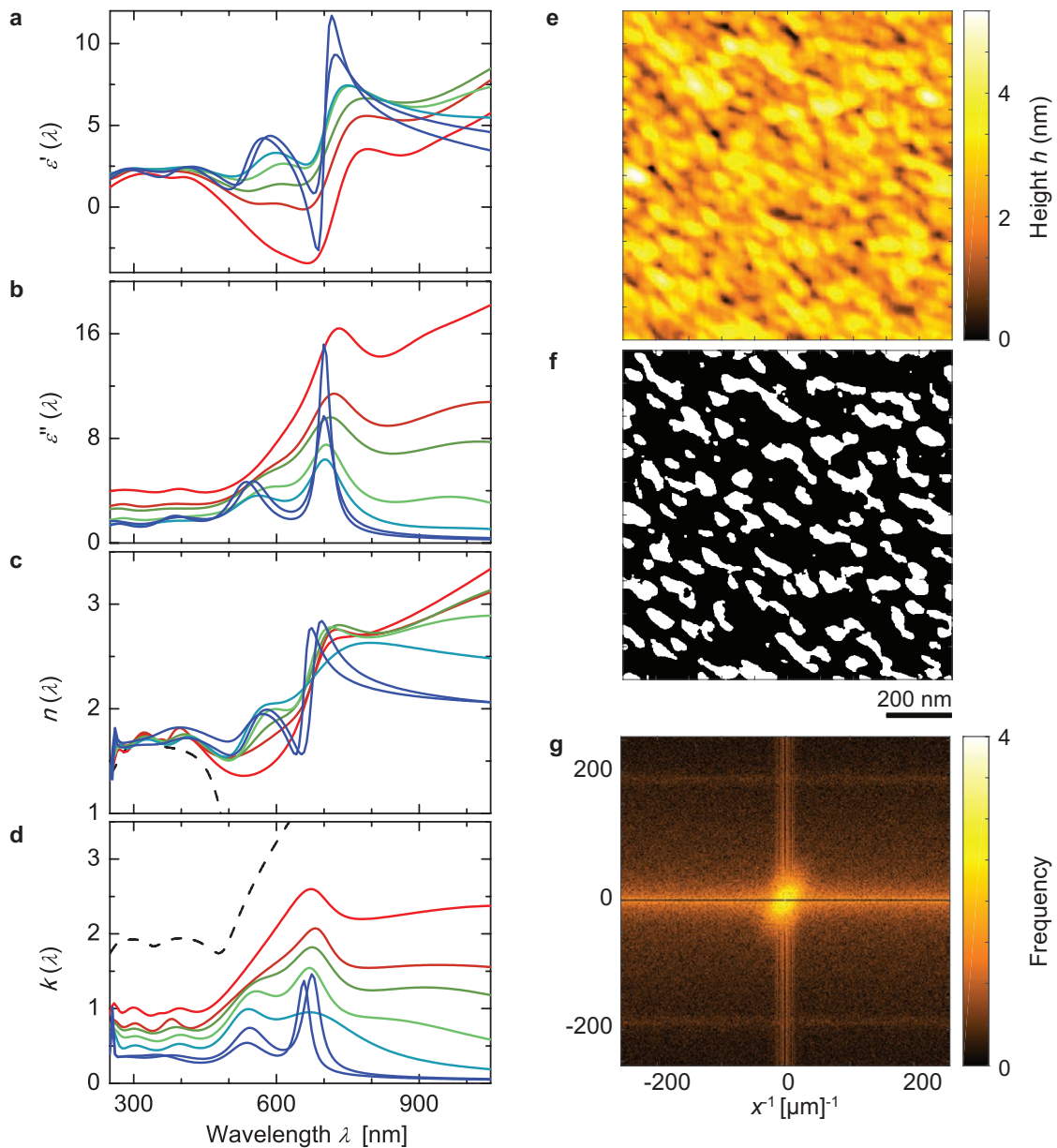


Figure 7 | Extracted dielectric function of Au-nanoparticles grown on PDMS. a, The imaginary part ϵ'' b, the real part ϵ' of the dielectric function c, the refractive index n and d, the extinction coefficient k of thermally evaporated Au on UV-cured DMS-V05 are extracted from spectroscopic Ψ – and Δ spectra and presented for representative growth times at 120 s, 240 s, 480 s, 840 s, 1300 s, 1800 s to 2400 s with corresponding film thicknesses between 2.7 nm, 5.3 nm, 7.1 nm, 9.5 nm, 12.2 nm, 14.6 nm to 16.8 nm, respectively, color-coded from blue to red.

The dashed line illustrates the bulk properties of Au found in literature.⁴⁴ Increased amplitudes of the extinction coefficient within the visible wavelength range can identify surface plasmon resonance peaks of Au elongated nanometer-sized clusters at a wavelength of about 540 nm and 640 nm. **e**, AFM surface scan of a $1 \times 1 \mu\text{m}^2$ -area on the Au film with corresponding thickness of 16.7 nm. **f**, Representative optical segmentation of the AFM surface scan of part (e). The 2D filter threshold strength determines the extracted size distribution of the elongated cluster semi axes. However, the average aspect of 2.1 ± 0.8 remains constant. **f**, Fourier transform of segmented AFM data from part (f) exhibits preferential orientation for elongated clusters.

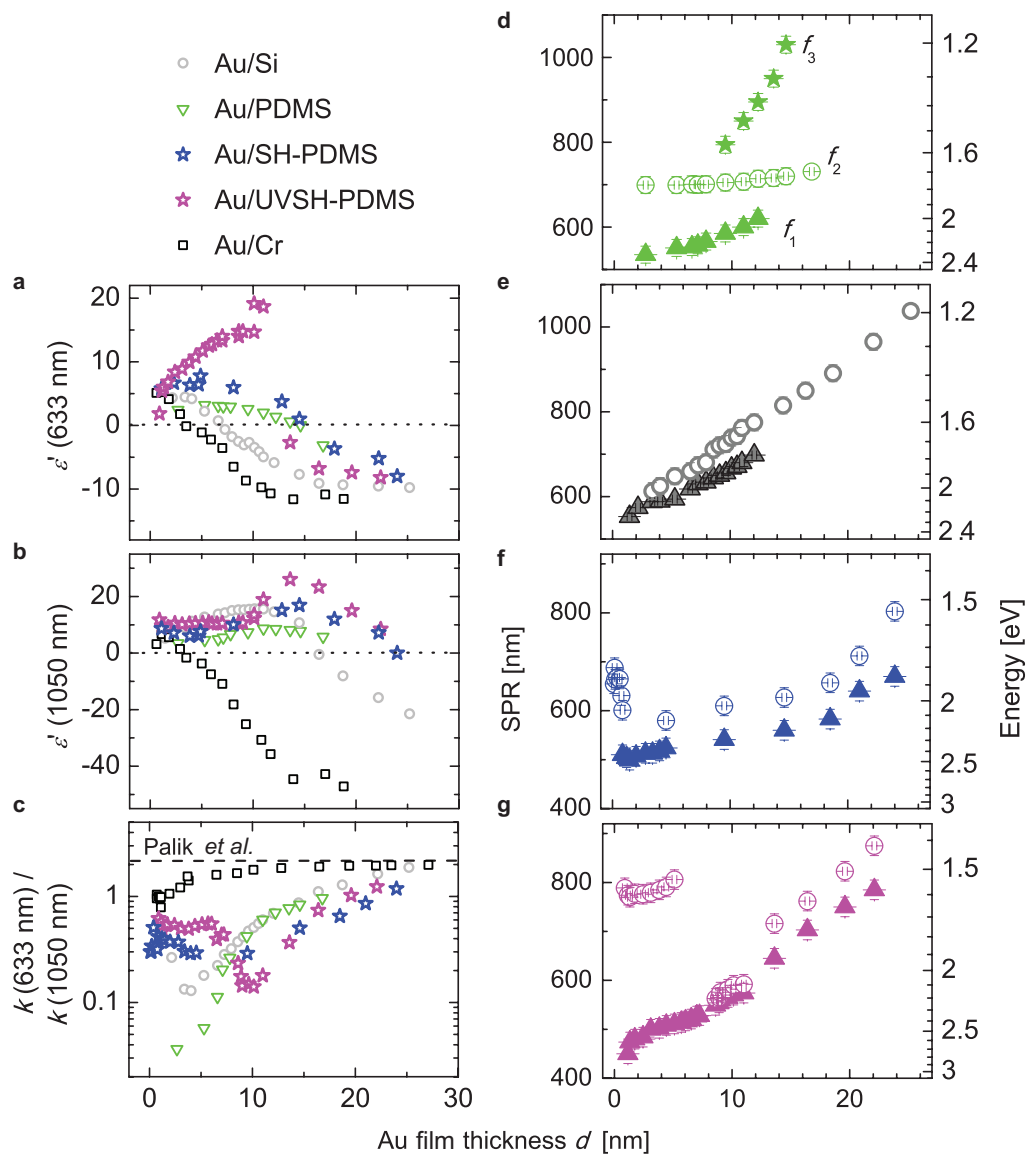


Figure 8 | Optical properties and surface plasmon resonance of growing Au-nanoparticles.

a, The real part ϵ' of the dielectric function at a wavelength of 633 nm corresponding to typical surface plasmon resonances of Au in the visible; **b,** at the wavelength of 1050 nm prominently influence by free electrons in the Drude-band, extracted from the 2D data plot in Figure 4 for growing gold films on Si/SiO₂ (grey circle), UV-cured thermally evaporated PDMS (DMS-V05) (green triangles), 7 nm-thin thermally evaporated SH-PDMS (blue star), on 7 nm-thin thermally evaporated UVSH-PDMS (violet star), a wrinkled Cr-nanostructure (black squares). **c,** To

illuminate the interplay of surface plasmon and Drude-band absorption during film formation, the ratio of extinction coefficient k at a wavelength of 633 nm and 1050 nm is presented. The dashed line displays bulk values of Au.⁴⁴ **d,e,f,g**, Surface plasmon resonance (SPR) frequencies f_1 (filled triangle), f_2 (open circle), f_3 (filled star) detected for gold films on Si/SiO₂ (grey circle), UV-cured thermally evaporated DMS-V05 (green triangles), 7 nm-thin thermally evaporated SH-PDMS (blue star), on 7 nm-thin thermally evaporated UVSH-PDMS (violet star). For Au growth on wrinkled Cr-nanostructure (black squares) no surface plasmons were distinguished.

References

- 1 McDonald, J. C. & Whitesides, G. M. Poly(dimethylsiloxane) as a Material for Fabricating Microfluidic Devices. *Acc. Chem. Res.* **35**, 491-499 (2002).
- 2 Zhang, B., Dong, Q., Korman, C. E., Li, Z. & Zaghoul, M. E. Flexible packaging of solid-state integrated circuit chips with elastomeric microfluidics. *Sci. Rep.* **3** (2013).
- 3 Hirsch, A., Michaud, H. O., Gerratt, A. P., de Mulatier, S. & Lacour, S. P. Intrinsically Stretchable Biphasic (Solid–Liquid) Thin Metal Films. *Adv. Mater.* (2016).
- 4 Töpfer, T. *et al.* Siloxane-based thin films for biomimetic low-voltage dielectric actuators. *Sensor Actuat. A Phys* **233**, 32-41 (2015).
- 5 Chakraborti, P. *et al.* A compact dielectric elastomer tubular actuator for refreshable Braille displays. *Sensor Actuat. A Phys.* **179**, 151-157 (2012).
- 6 Jung, K., Kim, K. J. & Choi, H. R. A self-sensing dielectric elastomer actuator. *Sensor Actuat. A-Phys.* **143**, 343-351 (2008).
- 7 Ozbay, E. Plasmonics: Merging Photonics and Electronics at Nanoscale Dimensions. *Science* **311**, 189-193 (2006).
- 8 Guo, P., Schaller, R. D., Ketterson, J. B. & Chang, R. P. H. Ultrafast switching of tunable infrared plasmons in indium tin oxide nanorod arrays with large absolute amplitude. *Nat Photon.* **10**, 267-273 (2016).
- 9 Moirangthem, R. S., Chang, Y.-C. & Wei, P.-K. Ellipsometry study on gold-nanoparticle-coated gold thin film for biosensing application. *Biomed. Opt. Express* **2**, 2569-2576 (2011).
- 10 Manjavacas, A. & Garcia de Abajo, F. J. Tunable plasmons in atomically thin gold nanodisks. *Nat Commun.* **5**, 1-7 (2014).
- 11 Stokes, N., McDonagh, A. M. & Cortie, M. B. Preparation of nanoscale gold structures by nanolithography. *Gold Bull* **40**, 310-320 (2007).
- 12 Grzelczak, M., Perez-Juste, J., Mulvaney, P. & Liz-Marzan, L. M. Shape control in gold nanoparticle synthesis. *Chem. Soc. Rev.* **37**, 1783-1791 (2008).
- 13 Töpfer, T., Lörcher, S., Weiss, F. & Müller, B. Tailoring the mass distribution and functional group density of dimethylsiloxane-based films by thermal evaporation. *APL Mater.* **4**, 056101 (2016).
- 14 Chaudhury, M. K. Surface free energies of alkylsiloxane monolayers supported on elastomeric polydimethylsiloxanes. *J. Ashes. Sci. Technol.* **7**, 669-675 (1993).
- 15 Ghosh, S. K. & Pal, T. Interparticle Coupling Effect on the Surface Plasmon Resonance of Gold Nanoparticles: From Theory to Applications. *Chemical Reviews* **107**, 4797-4862 (2007).
- 16 Jellison, G. E. & Modine, F. A. Parameterization of the optical functions of amorphous materials in the interband region. *Appl. Phys. Lett.* **69**, 371-373 (1996).
- 17 Al-Maawali, S. *et al.* Study of the Polydispersity of Grafted Poly(dimethylsiloxane) Surfaces Using Single-Molecule Atomic Force Microscopy. *The Journal of Physical Chemistry B* **105**, 3965-3971 (2001).
- 18 Cramer, N. B., Reddy, S. K., Cole, M., Hoyle, C. & Bowman, C. N. Initiation and kinetics of thiol–ene photopolymerizations without photoinitiators. *J. Polym. Sci. Pol. Chem.* **42**, 5817-5826 (2004).
- 19 De Sio, L., Caputo, R., Cataldi, U. & Umeton, C. Broad band tuning of the plasmonic resonance of gold nanoparticles hosted in self-organized soft materials. *J. Mater. Chem.* **21**, 18967-18970 (2011).
- 20 Anker, J. N. *et al.* Biosensing with plasmonic nanosensors. *Nature Mater.* **7**, 442-453 (2008).
- 21 Gupta, R., Dyer, M. J. & Weimer, W. A. Preparation and characterization of surface plasmon resonance tunable gold and silver films. *J. Appl. Phys.* **92**, 5264-5271 (2002).

- 22 Chandekar, A., Sengupta, S. K. & Whitten, J. E. Thermal stability of thiol and silane monolayers: A comparative study. *Appl. Surf. Sci.* **256**, 2742-2749 (2010).
- 23 Johnson, P. B. & Christy, R. W. Optical constants of transition metals: Ti, V, Cr, Mn, Fe, Co, Ni, and Pd. *Phys. Rev. B* **9**, 5056-5070 (1974).
- 24 Osmani, B. *et al.* in *AIP Conf. Proc.* 91-100.
- 25 Bowden, N., Brittain, S., Evans, A. G., Hutchinson, J. W. & Whitesides, G. M. Spontaneous formation of ordered structures in thin films of metals supported on an elastomeric polymer. *Nature* **393**, 146-149 (1998).
- 26 Lovrinčić, R. & Pucci, A. Infrared optical properties of chromium nanoscale films with a phase transition. *Phys. Rev. B* **80**, 205404 (2009).
- 27 Baba, A., Imazu, K., Yoshida, A., Tanaka, D. & Tamada, K. Surface plasmon resonance properties of silver nanoparticle 2D sheets on metal gratings. *SpringerPlus* **3**, 1-10 (2014).
- 28 Li, X. D., Chen, T. P., Liu, Y. & Leong, K. C. Influence of localized surface plasmon resonance and free electrons on the optical properties of ultrathin Au films: a study of the aggregation effect. *Opt. Express* **22**, 5124-5132 (2014).
- 29 Romaniello, P. & de Boeij, P. L. The role of relativity in the optical response of gold within the time-dependent current-density-functional theory. *J. Chem. Phys.* **122**, 164303 (2005).
- 30 El-Sayed, I. H., Huang, X. & El-Sayed, M. A. Selective laser photo-thermal therapy of epithelial carcinoma using anti-EGFR antibody conjugated gold nanoparticles. *Cancer Lett.* **239**, 129-135 (2006).
- 31 Oates, T. W. H., Wormeester, H. & Arwin, H. Characterization of plasmonic effects in thin films and metamaterials using spectroscopic ellipsometry. *Prog. Surf. Sci.* **86**, 328-376 (2011).
- 32 Hövel, M., Gompf, B. & Dressel, M. Dielectric properties of ultrathin metal films around the percolation threshold. *Phys. Rev. B* **81**, 035402 (2010).
- 33 Eustis, S. & El-Sayed, M. A. Why gold nanoparticles are more precious than pretty gold: noble metal surface plasmon resonance and its enhancement of the radiative and nonradiative properties of nanocrystals of different shapes. *Chem. Soc. Rev.* **35**, 209-217 (2006).
- 34 Khlebtsov, N. G. & Dykman, L. A. Optical properties and biomedical applications of plasmonic nanoparticles. *J. Quant. Spectrosc. Radiat. Transfer* **111**, 1-35 (2010).
- 35 Oates, T. W. H., Ryves, L. & Bilek, M. M. M. Dielectric functions of a growing silver film determined using dynamic in situ spectroscopic ellipsometry. *Opt. Express* **16**, 2302-2314 (2008).
- 36 Xue, Y., Li, X., Li, H. & Zhang, W. Quantifying thiol-gold interactions towards the efficient strength control. *Nat Commun.* **5** (2014).
- 37 Osmani, B. *et al.* in *SPIE 2016*. 979822-979811.
- 38 Chan, E. P. & Crosby, A. J. Spontaneous formation of stable aligned wrinkling patterns. *Soft Matt.* **2**, 324-328 (2006).
- 39 Olcum, S., Kocabas, A., Ertas, G., Atalar, A. & Aydinli, A. Tunable surface plasmon resonance on an elastomeric substrate. *Opt. Express* **17**, 8542-8547 (2009).
- 40 Teperik, T. V. *et al.* Omnidirectional absorption in nanostructured metal surfaces. *Nat Photon.* **2**, 299-301 (2008).
- 41 Fattorini, E. *et al.* Artificial Muscle Devices: Innovations and Prospects for Fecal Incontinence Treatment. *Ann. of Biom. Eng.* **44** (2016).
- 42 Rus, D. & Tolley, M. T. Design, fabrication and control of soft robots. *Nature* **521**, 467-475 (2015).
- 43 Anderson, I. A., Gisby, T. A., McKay, T. G., O'Brien, B. M. & Calius, E. P. Multi-functional dielectric elastomer artificial muscles for soft and smart machines. *J. Appl. Phys.* **112**, 041101 (2012).

Methods

Supplied materials. Supplied vinyl-terminated PDMS DMS-V05 (Gelest Inc., Morrisville, PA, USA) was utilized without additional purification steps. Au and Cr were supplied by Kurt J. Lesker Company, UK. As substrates, 2-inch n-doped Si-wafers (SIEGERT WAFER GmbH, Aachen, Germany) with a thickness of (279 ± 25) μm were used.

Synthesis of thiol-terminated polydimethylsiloxane. Bi-functional, hydroxyl-terminated polydimethylsiloxane (PDMS) Corbinol Fluid 5562, referred to as OH-PDMS, was supplied from Dow Corning, Germany. The other chemicals and dry solvents were bought from Sigma-Aldrich in the highest grade available and used as supplied. The solvents were distilled from technical grade supplies. The structure of PDMS was confirmed by ^1H nuclear magnetic resonance (^1H NMR): (400 MHz, $\text{CHCl}_3 + \text{K}_2\text{CO}_3$, δ , ppm): -0.50-0.35 (m, 122.70 H, -Si-O-Si(CH_3) $_2$ -), **0.36-0.76 (quint, 4.00 H (ref), -Si- CH_2 -)**, 1.41-1.84 (m, 4.55 H, -Si- CH_2 - CH_2 -), 1.89-2.16 (m, 1.62 H, -OH), 3.21-3.64 (2 t, 8.09 H -Si- CH_2 - CH_2 - CH_2 -O- CH_2 - CH_2 -), 3.64-3.96 (m, 3.98 H, -Si- C H_2 - CH_2 - CH_2 -O- CH_2 - CH_2 -OH)) and by gel permeation chromatography (GPC), see the black graph in Figure 2g. Inspired by the protocol of S.K. Bhatia *et al.*⁴⁵, 10 g (5.29 mmol, 1 eq.) of OH-PDMS were stirred overnight in a two-neck, round-bottom flask at 330 rpm, 81 °C, and 10^{-2} mbar to remove residual water. The atmosphere was exchanged three times with Ar. 50 ml of dry hexane were added. The mixture was cooled in Ar atmosphere to -20 °C while stirring at 180 rpm. 1.5 ml (11.0 mmol, 2.075 eq.) of triethylamine was added in one shot. After 15 min, 1.8 ml (10.8 mmol, 2.05 eq) of triuoromethanesulfonic anhydride was added and the activation of the terminal hydroxyl groups was left to proceed for 4 h before adding an excess of potassium thioacetate in dry dimethylformamid (22.0 mmol, 4.1 eq.). The reaction mixture was left stirring overnight, followed by three extractions with water to yield a

quantitative amount of a light brown viscous liquid after the evaporation of the hexane, from here on referred to as protected SH-PDMS. The NMR spectra of this protected SH-PDMS can be seen as the green-colored graph in Figure 2f: ^1H NMR (400 MHz, $\text{CHCl}_3 + \text{K}_2\text{CO}_3$, δ , ppm): -0.50-0.35 (m, 121.20 H, $-\text{Si}-\text{O}-\text{Si}((\text{CH}_3)_2)-$), **0.36-0.76 (quint, 4.00 H (ref), $-\text{Si}-\text{CH}_2-$)**, 1.31-1.46 (t, 0.47 H, $-\text{SH}$), 1.41-1.84 (m, 4.24 H, $-\text{Si}-\text{CH}_2-\text{CH}_2-$), 1.89-2.16 (m, 0.28 H, $-\text{OH}$), 2.16-2.46 (s, 4.32 H, $-\text{S}-\text{C}(\text{O})-\text{CH}_3$), 2.82-3.25 (t, 3.07 H, $-\text{Si}-\text{CH}_2-\text{CH}_2-\text{CH}_2-\text{O}-\text{CH}_2-\text{CH}_2-\text{S}-\text{C}(\text{O})-\text{CH}_3$), 3.21-3.64 (2 t, 8.19 H, $-\text{Si}-\text{CH}_2-\text{CH}_2-\text{CH}_2-\text{O}-\text{CH}_2-\text{CH}_2-$), 3.64-3.96 (m, 1.01 H, $-\text{Si}-\text{CH}_2-\text{CH}_2-\text{CH}_2-\text{O}-\text{CH}_2-\text{CH}_2-\text{OH}$), with the corresponding green-colored GPC curve in Figure 2g. To produce the terminal thiol functionality, 0.042 g (1.11 mmol, 2.1 eq.) of LiAlH_4 were dissolved in a 25 ml one-neck, round-bottom flask in 2 ml cold (ice bath) dry hexane and stirred at 200 rpm. 1 g (0.53 mmol, 1 eq.) of thioacetate-modified PDMS was dissolved in cold (ice bath) dry hexane and added drop-wise to the stirred LiAlH_4 . 4 ml of dry tetrahydrofuran was added to increase the solubility of the reaction partners and the deacetylation was left stirring for 3 h in the ice bath before quenching the excess of LiAlH_4 slowly with cold water. The triple extraction with water yielded 0.87 g of a golden, viscous liquid (unprotected SH-PDMS) after the evaporation of the hexane. The NMR spectra are shown as the blue-colored curve in Figure 2f: ^1H NMR (400 MHz, $\text{CHCl}_3 + \text{K}_2\text{CO}_3$, δ , ppm): -0.50-0.35 (m, 148.37 H, $-\text{Si}-\text{O}-\text{Si}((\text{CH}_3)_2)-$), **0.36-0.76 (quint, 4.00 H (ref), $-\text{Si}-\text{CH}_2-$)**, 1.41-1.84 (m, 5.43 H, $-\text{Si}-\text{CH}_2-\text{CH}_2-$), 1.89-2.16 (m, 0.44 H, $-\text{OH}$), 2.59-2.79 (dt, 2.60 H, $-\text{CH}_2-\text{S}-\text{S}-\text{CH}_2-$), 3.21-3.64 (2 t, 7.82 H, $-\text{Si}-\text{CH}_2-\text{CH}_2-\text{CH}_2-\text{O}-\text{CH}_2-\text{CH}_2-$), 3.64-3.96 (m, 1.24 H, $-\text{Si}-\text{CH}_2-\text{CH}_2-\text{CH}_2-\text{O}-\text{CH}_2-\text{CH}_2-\text{OH}$), with the corresponding blue-colored GPC graph in Figure 2g.

To assess the thermal stability of synthesized SH-PDMS, 100 mg was heated to 150 °C, far below the thermal decomposition temperature of PDMS backbone⁴⁶ or methyl side group bonds,⁴⁷ and kept at this temperature for 40 min. The analysis of thermally treated SH-PDMS can be seen in the red-colored ^1H NMR graph in Figure 2f: (400 MHz, $\text{CHCl}_3 + \text{K}_2\text{CO}_3$, δ , ppm): -0.50-0.35 (m, 153.64 H, $-\text{Si}-\text{O}-$

Si((CH₃)₂)₂), **0.36-0.76 (quint, 4.00 H (ref), -Si-CH₂-)**, 1.41-1.84 (m, 6.43 H, -Si-CH₂-CH₂-), 1.89-2.16 (m, 0.45 H, -OH), 2.59-2.79 (dt, 2.62 H, -CH₂-S-S-CH₂-), 3.21-3.64 (2 t, 7.99 H, -Si-CH₂-CH₂-CH₂-O-CH₂-CH₂-S-), 3.64-3.96 (m, 1.32 H, -Si-CH₂-CH₂-CH₂-O-CH₂-CH₂-OH)) with the corresponding red-colored GPC graph in Figure 2g.

The NMR and GPC spectra of supplied HO-PDMS indicate a chemically pure and homogeneously dispersed substance ($\bar{D} = 1.4$) with an NMR-based number average molecular weight M_n of 1733 g mol⁻¹ (the quintet at 0.36 to 0.76 served as reference of 4 H in all spectra). After the exchange of terminal hydroxy groups on OH-PDMS for thioacetate functionalities, a broad singlet within the NMR data at 2.16 to 2.41 ppm confirms the modification. The corresponding integral of 4.42 suggests that the reaction yielded about 75 % thioacetate functionality. The subsequent reduction with LiAlH₄ releases acetate, which is removed in the water extraction causing the disappearance of the respective singlet at 2.16 to 2.41 ppm (Figure 2f, blue-colored spectra). The integrals corresponding to the signals from the dimethylsiloxane units at -0.50 to 0.35 ppm rise from 125 to 151 after deacetylation, confirming the shift of molecular weight distribution to increased molecular weights (corresponding GPC curves from green to blue color in Figure 2g), indicating disulfide bond formation after deprotection. The integrals of the spacer CH₂-groups are preserved for the reaction steps and characteristic shifts of the CH₂-group, subsequently connected to -OH, -thioacetate and -SH have been observed. The signal of the unprotected terminal thiol groups seems superposed with the signal of the CH₂-group and is therefore not clearly resolved but indirectly confirmed by the increase of the respective integral at 1.41 to from 5.49 to 6.33 ppm, blue- and red-colored NMR spectra in Figure 2f, respectively. The GPC analysis confirms the integrity of the polymer chains during the reaction steps, the thermal stability of the SH-PDMS for a temperature of 150 °C and a heating period of 40 min. A slight shift to increased molecular weights indicates chain elongation due to disulfide bond formation (red-colored graph in Figure 2g). SH-PDMS was thermally evaporated at a

temperature of $(140 \pm 5)^\circ\text{C}$ to avoid the thermal degradation of the thiol groups above 150°C .²²

Molecular beam deposition. The PDMS, Au, and Cr were thermally evaporated and deposited under ultra-high vacuum (UHV) conditions at a base pressure of 10^{-7} mbar. DMS-V05 and synthesized SH-PDMS were evaporated using low-temperature effusion cells (NTEZ, Dr. Eberl MBE Komponenten GmbH, Weil der Stadt, Germany) with a 25 cm^3 crucible for DMS-V05 and a 2 cm^3 crucible for SH-PDMS. High-temperature effusion cells (HTEZ, Dr. Eberl MBE Komponenten GmbH, Weil der Stadt, Germany) with 10 cm^3 PBN-crucibles were utilized for Au and Cr. DMS-V05 thin films were evaporated at a crucible temperature of $(200 \pm 5)^\circ\text{C}$ well below the temperature of thermal degradation of the vinyl end groups.¹³ Au and Cr were evaporated at temperatures from $1,400^\circ\text{C}$ to $1,440^\circ\text{C}$ corresponding to deposition rates of about $1.1 \cdot 10^{-2}\text{ nm s}^{-1}$ and $3.0 \cdot 10^{-3}\text{ nm s}^{-1}$, respectively. Within the range of chosen deposition rates no distinct influence to the Au nanoparticle formation is expected.²¹ The Si-substrate was mounted within a distance of 400 mm from the crucibles and rotated at a speed of 5 rpm to obtain a homogenous growth.

Ultraviolet cross-linking. The cross-linking was initiated by *in-situ* ultra-violet (UV) light irradiation from an externally mounted source (H2D2 light source L11798, Hamamatsu, Japan) through a CaF-window.⁴

Real-time spectroscopic ellipsometry. To *in situ* examine the optical properties of the forming nanostructures, a spectroscopic ellipsometer (SE801, Sentech, Berlin, Germany) with SpectraRay3 software was utilized. The spectroscopic ψ - and Δ -values, ranging from 190 to 1050 nm, were monitored at a frequency between 0.5 to 2 Hz at an incident angle of 70° to the normal of the substrate's surface. The 4 mm diameter of incident beam resulted in a $4 \times 10\text{ mm}^2$ spot area on the substrate.

The obtained Ψ - and Δ -values, or the Fourier coefficients S_1 and S_2 , are related to the complex Fresnel reflection coefficients r_p and r_s of s- and p-polarized light and their ratio ρ by

$$\rho = r_p / r_s = \tan \Psi \cdot e^{i\Delta} \quad (1).$$

Based on the obtained Fresnel reflection coefficient ratio it is possible to extract the wavelength-dependent dielectric function $\varepsilon(\lambda)$

$$\langle \varepsilon \rangle = \langle \varepsilon' \rangle + i \langle \varepsilon'' \rangle = \langle \tilde{n} \rangle^2 = \left(\langle n \rangle + i \langle k \rangle \right)^2 = \varepsilon_0 \sin^2(\phi_0) \left[1 + \tan^2(\phi_0) \left(\frac{1-\rho}{1+\rho} \right)^2 \right] \quad (2).$$

with the angle of incidence ϕ_0 , the vacuum permittivity $\varepsilon_0 = 1$, $n(\lambda)$ the real and $k(\lambda)$ the imaginary parts of the refractive index, respectively.

To observe the growth and cross-linking of the evaporated PDMS its dielectric function was modeled with the Tauc-Lorentz (TL) dispersion formula.¹⁶ A Bruggeman effective medium model⁴⁸ was included to obtain the surface roughness induced by the nucleation centers or polymer/metal interface layers. This layer is considered to have an effective dielectric or optical property deduced from equal fractional parts of deposited PDMS and void material, cf. equation (3):

$$0 = \sum_{i=1}^N f_i \frac{n_i^2 - n_e^2}{n_i^2 + 2n_e^2} \quad (3)$$

The EMA is applicable if the grown film fulfills two key assumptions, namely first the surface roughness/nucleation centers are smaller than the minimum wavelength, in order to ignore light scattering, and second the dielectric function has to be size- and shape-independent. For the thermally evaporated PDMS, these assumptions are fulfilled. For the data evaluation the void fraction was set to 0.5, which is reasonable according to Fujiwara *et al.*⁴⁹.

To model the dielectric function of the utilized noble metals a Drude-Lorentz oscillator model was applied. Although, an enhanced flexibility of Gaussian oscillators is mentioned in literature⁵⁰, we found DL-oscillators to model precisely the

optical properties of nucleating Au nanoparticles. This is a combination of two dispersion types. First, the Drude absorption of free charge carriers, assuming that they act in phase in response to the applied electric field and second, the Lorentz oscillator, effectively describing the electrons bound to a positive ion core³¹.

For the assessment of the model the mean square error (MSE) of the divergence from the obtained fit to the acquired data was calculated. The MSE is defined in equation (4):

$$\text{MSE} = \frac{1}{N} \sqrt{\sum_{i=1}^N \left\{ \left(\frac{\Psi_i^{\text{mod}} - \Psi_i^{\text{exp}}}{\sigma_{\Psi_i}^{\text{exp}}} \right)^2 + \left(\frac{\Delta_i^{\text{mod}} - \Delta_i^{\text{exp}}}{\sigma_{\Delta_i}^{\text{exp}}} \right)^2 \right\}} \quad (4)$$

Atomic force microscopy. The surface topography of the thermally evaporated nanostructures was scanned using atomic force microscopy (AFM). The AFM scanning system (FlexAFM C3000, Nanosurf AG, Switzerland) was operated in tapping mode using a soft cantilever (Tap190AI-G probe, NanoAndMore GmbH, Wetzlar, Germany). Areas of $5 \times 5 \mu\text{m}^2$ were scanned with a vibration amplitude of 2 V and a set point of 20 %. In total, 512 lines at a speed of 1 s per line were acquired for each image. The root-mean-squares values were calculated using the Gwyddion 2.41 software (Gwyddion: Open-source software for SPM data analysis, <http://gwyddion.net>).

Nanoparticle segmentation. The acquired color images were converted to gray-scale using MATLAB (The MathWorks, Inc., Natick, United States). A 2D Frangi filter implemented in MATLAB (The MathWorks, Inc., Natick, United States)⁵¹ was used to identify the borders of the PDMS islands.

Nuclear magnetic resonance analysis. ¹H-NMR spectra were recorded on a Bruker DPX-400 spectrometer in deuterated chloroform without tetramethylsilane.

The analysis (phase correction and Wittaker Smoother to adjust the baseline) was performed in MestReNova 10.0.1-14719 (Mestrelab Research S.L., Spain).

Gel permeation chromatography. Gel permeation chromatography traces were recorded using WinGPC (v8.20 build 4815) connected to an Agilent 1200 system equipped with a refractive index detector (RI) and a series of analytical SDV columns (pre-column (5 cm), $1\text{e}^3 \text{ \AA}$ (30 cm), and $1\text{e}^5 \text{ \AA}$ (30 cm), all $5 \mu\text{m}$ particles and 0.8 cm in diameter, PSS, Germany). The columns and RI were kept at $35 \text{ }^\circ\text{C}$, the system was operated at a flow rate of 1 ml s^{-1} and calibrated against narrow distributed polystyrene standards.

References

- 44 Palik, E. D. *Handbook of Optical Constants of Solids III*. (Academic, 1998).
- 45 Bhatia, S. K. & Hajdu, J. A new approach to the synthesis of thioether phospholipids. Preparation of 1-thiohexadecyl-2N-acylaminodeoxyglycerophosphocholines. *Tetrahed. Lett.* **29**, 31-34 (1988).
- 46 Chenoweth, K., Cheung, S., van Duin, A. C. T., Goddard, W. A. & Kober, E. M. Simulations on the Thermal Decomposition of a Poly(dimethylsiloxane) Polymer Using the ReaxFF Reactive Force Field. *J. Am. Chem. Soc.* **127**, 7192-7202 (2005).
- 47 Deshpande, G. & Rezac, M. E. Kinetic aspects of the thermal degradation of poly(dimethyl siloxane) and poly(dimethyl diphenyl siloxane). *Polym. Degrad. Stab.* **76**, 17-24 (2002).
- 48 Bruggeman, D. A. G. Berechnung verschiedener physikalischer Konstanten von heterogenen Substanzen. I. Dielektrizitätskonstanten und Leitfähigkeiten der Mischkörper aus isotropen Substanzen. *Ann. Phys.* **416**, 665-679 (1935).
- 49 Fujiwara, H., Koh, J., Rovira, P. I. & Collins, R. W. Assessment of effective-medium theories in the analysis of nucleation and microscopic surface roughness evolution for semiconductor thin films. *Phys. Rev. B* **61**, 10832-10844 (2000).
- 50 Loncaric, M., Sancho-Parramon, J. & Zorc, H. Optical properties of gold island films - a spectroscopic ellipsometry study. *Thin Solid Films* **519**, 2946-2950 (2011).
- 51 Kroon, D.-J. *Hessian Based Frangi Vesselness Filter*, <<http://www.mathworks.com/matlabcentral/fileexchange/24409-hessian-based-frangi-vesselness-filter>> (2009).

3 Conclusions and Outlook

Organic molecular beam deposition (OMBD) enables the controlled evaporation of polydimethylsiloxane (PDMS) chains at temperatures below thermal degradation. The energy barrier of thermal degradation is determined by the stability of functional side groups, e.g. a degradation temperature of 230 °C for the vinyl terminations has been found. The side groups of linear PDMS chains dominate intermolecular Van-der-Waals interactions. Nevertheless, the unique flexibility of linear PDMS enables folding at the crucible surface such that molecular weights of up to 6.000 g/mol can be evaporated. As a result, the functional group density for end-terminated linear PDMS was tailored between 2.8 to 11 %. In principle the degree of functionality can be extended by using copolymers with altered side terminations. As a drawback, the substitution of methyl groups would lead to increased intermolecular interactions e.g. steric hindrance. The resulting increase in vaporization heat would narrow the spectrum of molecular weights accessible for thermal evaporation. Nevertheless, we propose the incorporation of phenyl terminations to manipulate the dielectric function of the PDMS thin films. Enhanced dielectric properties would influence the actuation efficiency positively in dielectric elastomer actuators. The heating of the substrate holder to temperatures close to that of the evaporation temperature should be considered in the future. This would sharpen both, the molecular weight distribution and the functional group density, which are broadened by the Boltzmann energy distribution. Thus, thermal evaporation allows for sharp tailoring of molecular weights and functional group density to manipulate e.g. the elastic properties and surface energy, respectively, of nanometer-thin PDMS films.

Within this work, the cross-linking mechanism of ultraviolet light (UV) curing has been illuminated for vinyl-terminated PDMS. Preferably vinyl-groups with pronounced absorption at 210 nm become radicalized and form prolonged chains. Additionally methyl side-groups become radicalized through irradiation at wavelengths below 190 nm. At high irradiation densities the interplay of cross-linking gradient and heat input from the irradiation source leads to isotropic-distributed wrinkled surface morphology. Thus, we propose *in situ* UV-curing during the deposition to reach homogenous cross-linking density and surface morphology. Time-resolved spectroscopic ellipsometry has been utilized to monitor the dynamics of cross-linking more in detail. It has been observed, that the cross-linking velocity is dependent on the chain length or to the functional group density, respectively. Obviously the longer the chains less bonds have to be cross-linked. As the accessible chain length for thermal evaporation is limited we propose Benzophenone-based photo initiators to be incorporated into the OMBD process. Implemented into the polymer network, their distinct absorption bands between 200 to 400 nm can extend the range of absorbable irradiation wavelengths. Thus, the growth rate for *in situ* cross-linked PDMS film is no longer limited by the UV-curing speed. Moreover it is expected to gain improved control of cross-linking density and elastic properties of the PDMS films.

Furthermore this work presents the control of UV-induced microstructures on PDMS thin-films. Coated with sputtered gold they can act as pre-stretched contact layers for DEAs tolerating high strains. Four point measurements revealed for the thinnest, still conductive, 10 nm-thin Au electrode a conductivity threshold for strains above 22%. Therefore, alternative approaches have to be considered for future stretchable electronics.

Spectroscopic ellipsometry (SE) constitutes a unique technique to access *in situ* optical properties, plasmonic fingerprints and film topography simultaneously. Two important conclusions stand out from this ellipsometric study: First, we highlight the ability to extract insulator-to metal transition of soft hetero nanostructures with sub-nanometer resolution. Once the prevalent growth mode of metal nanoparticles is derived from real space imaging e.g. atomic force microscopy, SE allows interpretation for the size, shape and percolation events of metal nanoparticles on multilayered heterostructures. Second, real-time monitoring offers the precise control of Au-S bond based SAMs and the formation of isotropic or prospective anisotropic ordered metal/elastomer heterostructures. Our results suggest a dramatic improvement in gold homogeneity and surface roughness for applied nanometer-thin interlayers of SH-PDMS and Cr. We claim the gold-coated hetero nanostructures under study to retrieve some flexibility under strain due to either localized covalent gold-thiol bonds or pre-stretched nanometer-thin Cr-wrinkles and thus they will enhance the maximal strain level for stretchable nanoelectronics. Recently, alloying gallium on gold has been shown to be a promising stretchable and self-healing electrode under high strains. The variability of the MBD system allows for the evaporation of two or more components simultaneously. Liquid metal electrodes, fluid at room temperature, blended of indium and gallium can be realized.

This work presents a proof of concept for the proposed thin film technology for low voltage operation of dielectric elastomer actuators. Single layer dielectric elastomer actuators based on thermally evaporated, UV-cured polydimethylsiloxane have been sandwiched between sputtered Au-electrodes. Manufactured as asymmetric cantilever structures, the bending characteristic revealed a maintained actuation of a 200 nm-thin film, activated in the voltage range between 1 and 12 V, compared to a 4 μm -thick, spin-coated film, operated between 100 and 800 V. The force of the 200 nm-thin film actuator was about 10^{-4} N. Extrapolated, multilayer actuators with more than 10^4 layers would reach forces comparable to natural muscles.

Growth rates of thermally evaporated *in situ* cured PDMS films were limited to 100 nm/h. First, improved growth rates can be realized with higher evaporation rates. This would demand for other functional side groups, e.g. phenyl with enhanced thermal stability. Second, multiple evaporators and multiple UV-irradiation sources could accelerate the process speed towards industrial applicability. Contrary, in cooperation with Florian Weiss *et al.* we presented alternating current electro-spray deposition (ACESD) as a suitable alternative technique to OMBD. By depositing vinyl-terminated PDMS solution and subsequent UV-curing PDMS thin films with sub-micrometer thickness were grown with up to two orders of magnitude increased deposition rates compared to OMBD. Further advantages of ACESD are the inexpensive set up and the unconstrained choice of polymer. However, sub-micrometer films with deposition rates above 1 $\mu\text{m}/\text{h}$ exhibited island-growth rather than homogeneous films. The locally height variations are related to multi-cone jet mode and minimal droplet sizes of a few micrometers within the spray. In future, once

a stable single cone-jet spray has been established the enhanced film homogeneity qualifies ACESD for industrial-scale production. Multiple nozzle arrangements could be employed, for example to manufacture large-area, multi-stack DEAs.

However, the precise growth control of nanometer-thin PDMS films from the first monolayer on, distinguishes OMBD for polymer thin film technology. The manufacturing of confluent PDMS thin-films is not only of interest for low-voltage actuation but also for low-voltage sensing based on the technology of single layer electrically activated polymers. For these single layer DEA nanostructures the drawback of small deposition rates vanishes while the great advantage of unique homogeneity arises. We anticipate that this technique will even qualify to realize functionalized surfaces for biomedical devices, such as microfluidic applications, or tailoring cell-polymer interactions.

Finally, this work presents a great improvement of PDMS nanometer-thin film preparation towards the fabrication of biomedical devices. MBD combined with real-time spectroscopic ellipsometry SE paves the way to tailor soft multilayer metal/elastomer heterostructures on the nanometer scale. In a low-voltage DEA configuration we anticipate great potential as nanophotonic devices, e.g soft tuneable gratings for nano-optics and finally for multilayer DEA-based artificial muscles for medical implants. Combined with *in situ* SE, a low-voltage-tuneable heterostructure morphology qualifies for flexible biosensors to monitor and manipulate bio-molecular interactions on metal nanoparticles e.g. antibodies.

Bibliography

- [1] Becker, H.-D., Stenzl, A., Wallwiener, D., and Zittel, T., [*Urinary and Faecal Incontinence*], Springer-Verlag, Berlin Heidelberg (2005).
- [2] Khater, U. M., Haddad, G., and Ghoniem, G. M., [*Pelvic Floor Dysfunction: A Multidisciplinary Approach*], ch. Epidemiology of Non-Neurogenic Urinary Dysfunction, 9–13, Springer, London (2009).
- [3] Fattorini, E. e. a., “Artificial Muscle Devices: Innovations and Prospects for Fecal Incontinence Treatment,” *Annals of Biomedical Engineering* **5**(44), 1355–1369 (2016).
- [4] Pelrine, R., Kornbluh, R., Pei, Q., and Joseph, J., “High-Speed Electrically Actuated Elastomers with Strain Greater Than 100%,” *Science* **287**(5454), 836–839 (2000).
- [5] Zhang, Q. M., Li, H., Poh, M., Xia, F., Cheng, Z.-Y., Xu, H., and Huang, C., “An all-organic composite actuator material with a high dielectric constant,” *Nature* (419), 284–287 (2016).
- [6] Madsen, F. B., Daugaard, A. E., Hvilsted, S., and Skov, A. L., “The Current State of Silicone-Based Dielectric Elastomer Transducers,” *Macromolecular Rapid Communications* (2016).
- [7] Rosset, S. and Shea, H. R., “Flexible and stretchable electrodes for dielectric elastomer actuators,” *Applied Physics A* **110**(2), 281–307 (2012).
- [8] Hwang, T., Kwon, H.-Y., Oh, J.-S., Hong, J.-P., Hong, S.-C., Lee, Y., Ryeol Choi, H., Jin Kim, K., Hossain Bhuiya, M., and Nam, J.-D., “Transparent actuator made with few layer graphene electrode and dielectric elastomer, for variable focus lens,” *Applied Physics Letters* **103**(2) (2013).
- [9] Watanabe, M., Shirai, H., and Hirai, T., “Wrinkled polypyrrole electrode for electroactive polymer actuators,” *Journal of Applied Physics* **92**(8) (2002).
- [10] Habrard, F., Patscheider, J., and Kovacs, G., “Super-compliant metallic electrodes for electroactive polymer actuators,” *Proc. SPIE* **8340**, 13–16 (2012).
- [11] Rosset, S., Niklaus, M., Dubois, P., and Shea, H. R., “Metal ion implantation for the fabrication of stretchable electrodes on elastomers,” *Advanced Functional Materials* **19**(3), 470–478 (2009).
- [12] Graz, I. M., Cotton, D. P. J., and Lacour, S. P., “Extended cyclic uniaxial loading of stretchable gold thin-films on elastomeric substrates,” *Applied Physics Letters* **7**(94), 071902 (2009).
- [13] Köser, J., Gaiser, S., and Müller, B., “Contractile cell forces exerted on rigid substrates,” *European Cells and Materials* (21), 479–487 (2011).

- [14] Meyer, G. and Amer, N. M., “Novel optical approach to atomic force microscopy,” *Applied Physics Letters* **12**(53), 1045–1047 (1988).
- [15] Osmani, B., Töpfer, T., Deschenaux, C., Nohava, J., Weiss, F. M., Leung, V., and Müller, B., “Micro- and nanostructured electro-active polymer actuators as smart muscles for incontinence treatment,” *AIP Conference Proceedings* **1646**(1) (2015).
- [16] Weiss, F. M., Töpfer, T., Osmani, B., Winterhalter, C., and Müller, B., “Impact of electrode preparation on the bending of asymmetric planar electro-active polymer microstructures,” **9056**, 905607–905609 (2014).
- [17] Bowden, N., Brittain, S., Evans, A. G., Hutchinson, J. W., and Whitesides, G. M., “Spontaneous formation of ordered structures in thin films of metals supported on an elastomeric polymer,” *Nature* **393**(6681), 146–149 (1998).
- [18] Jaworek, A. and Sobczyk, A. T., “Electrospraying route to nanotechnology: An overview,” *Journal of Electrostatics* **66**(3), 197–219 (2008).
- [19] Morota, K., Matsumoto, H., Mizukoshi, T., Konosu, Y., Minagawa, M., Tanioka, A., Yamagata, Y., and Inoue, K., “Poly(ethylene oxide) thin films produced by electrospray deposition: morphology control and additive effects of alcohols on nanostructure,” *Journal of Colloid and Interface Science* **279**(2), 484–492 (2004).
- [20] Rietveld, I. B., Kobayashi, K., Yamada, H., and Matsushige, K., “Process parameters for fast production of ultra-thin polymer film with electrospray deposition under ambient conditions,” *Journal of Colloid and Interface Science* **339**(2), 481–488 (2009).
- [21] Weiss, F., Töpfer, T., Osmani, B., Peters, S., Kovacs, G., and Müller, B., “Electro-spraying nanometer-thin elastomer films for low-voltage dielectric actuators,” *Advanced Electronic Materials* (1500476), 94300B (2016).
- [22] Xie, J., Jiang, J., Davoodi, P., Srinivasan, M. P., and Wang, C.-H., “Electrohydrodynamic atomization: A two-decade effort to produce and process micro/nanoparticulate materials,” *Chemical Engineering Science* **125**, 32–57 (2015).
- [23] Weiss, F., Töpfer, T., Osmani, B., Deyhle, H., Kovacs, G., and Müller, B., “Thin film formation and morphology of electro-sprayed polydimethylsiloxane,” *Advanced Electronic Materials* **13**(32), 3276–3283 (2016).
- [24] Cho, A.-Y., “Morphology of Epitaxial Growth of GaAs by a Molecular Beam Method: The Observation of Surface Structures,” *Journal of Applied Physics* **41**, 2780–2786 (jun 1970).
- [25] O’Connor, J., Sexton, B., and Smart, R., eds., [*Surface Analysis Methods in Materials Science*], Springer, Heidelberg (2013).
- [26] Kovacic, P., Sforazzini, G., Cook, A. G., Willis, S. M., Grant, P. S., Assender, H. E., and Watt, A. A. R., “Vacuum-Deposited Planar Heterojunction Polymer Solar Cells,” *ACS Appl. Mater. Interfaces* **3**(1) (2011).

-
- [27] Müller, B., Cai, C., Kündig, A., Tao, Y., Bösch, M., Jäger, M., Bosshard, C., and Günter, P., “In-plane alignment of non centrosymmetric molecules by oblique-incidence molecular beam deposition,” *Appl. Phys. Lett.* (74), 3110–3112 (1999).
- [28] Töpfer, T., Weiss, F., Osmani, B., Bippes, C., Leung, V., and Müller, B., “Siloxane-based thin films for biomimetic low-voltage dielectric actuators,” *Sensors and Actuators A: Physical* **233**, 32–41 (2015).
- [29] Weiss, F., Madsen, F. B., Osmani, B., Leung, V., Töpfer, T., and Müller, B., “Molecular beam deposition of high-permittivity polydimethylsiloxane for nanometer-thin elastomer films in dielectric actuators,” *Materials and Design* **105**, 106–113 (2016).
- [30] Oates, T. W. H., Ryves, L., and Bilek, M. M. M., “Dielectric functions of a growing silver film determined using dynamic in situ spectroscopic ellipsometry,” *Optics Express* **16**(4), 2302 (2011).

Acknowledgments

At the end of this journey I would like to acknowledge a number of special persons with which I had the opportunity to meet and share work, discussions and experiences during the past three years.

For offering me the possibility of this Phd-position I would like to express my gratitude first to Prof. Bert Müller. Under his supervision I grew within an interdisciplinary environment, which confronted me with challenging scientific problems from the first day. The ‘Smartsphincter’-project excited for the whole time with a variety of research topics, which haven’t been part of my personal expertise so far. He offered me the freedom to explore and build up two novel processes to realize nanometer-thin polydimethylsiloxane films, first alternate current electro-spray together with Florian Weiss at the EMPA in Dübendorf and second molecular beam deposition with the ‘Smartsphincter’-team Basel, both new to the dielectric actuator community. Finally this environment together with the socially enriching staff of this department broadened my horizon.

At this point I would also like to thank Prof. Ernst Meyer for accepting the position as second reviewer of my thesis.

Not to forget the valuable support from Sascha Martin for the construction of the test UHV chamber and letting me use his workshop at the physics department of the university Basel as well as the support from Volker Brunner from the workshop at the university hospital Basel and Andreas Tonin from the electric workshop at the physics department in Basel.

I am also grateful to Monica Schönenberger for letting me use the Nanotech Service lab and its equipment as well as Theo Bühler from the Fachhochschule Nordwestschweiz for lending us the sputter deposition system and introducing me to MIR-spectroscopy.

A special thanks goes to Samuel Lörcher for synthesizing polymer specifically tailored to our technical needs and helping me with the polymer analysis. He contributed an important part to my journal publications which enabled me finally to hand in my thesis in time. Thus another great thanks is attributed to Prof. Wolfgang Meyer for offering us the time at the GPC and NMR analysis apparatuses.

Of course I would like to thank all colleagues at the Biomaterials Science Center for the great time and support, especially Florian Weiss, Bekim Osmani, Vanessa Leung, Thomas Pfohl as well as Hans Deyhle for all their input, helpful discussions and data analysis.

Last but not least I would like to thank all my friends and family who were an amazing support throughout all these years, highlighting the former Freiburger physicians who dragged me through the tough practical training courses.

A heartfelt thanks is addressed to my girlfriend Marie Patierno for her tolerance and her support especially during the last months of the thesis and to my daughter who has given me great joy even that she is was not even in this world yet.

Curriculum vitae

Personal information

Name

Töpper, Tino

Address

 Alte Breisacher Strasse 15
 79112 Freiburg i. Br.

Telephone

+49 176 22932684

E-mail

tino_toepper@yahoo.de

Date of birth

15/01/87

Family status

Unmarried



Languages

German - Native

English - fluent

French - fluent

Career, Practical work

May 2013 – May 2016

Phd student at University of Basel

Realization and characterization of nanometer-thin polymer films for dielectric elastomer actuators acting as biomimetic artificial muscles implant

July 2010 – June 2012

Research assistant at the IAF Freiburg

Construction and alignment of complex laser modules (quantum cascade laser and disk lasers) for sensing, military and medical applications.

Characterisation of semiconductor heterostructures (SIMS, XRD, AFM)

Optical simulations (Mathematica, Spectrum 32) to develop semiconductor heterostructures for optically pumped disk lasers

Process optimization for the manufacturing and assembly of semiconductor lasers (CAD-drawings, Coatings, Liquid Capillary Bonding)

June 2009 – September 2009

Internship at Strathclyde University Glasgow (IOP)

Research on semiconductor lasers for optical communication systems and medical applications

October 2006 – May 2009

Research assistant at m2k-Laser GmbH

Characterization of semiconductor laser diodes, evaluation and maintenance of databases.

Publications

Journal Papers

18

Conference Proceedings

12

First Author

7

Poster contributions	
June 2016	ICSE-7 International Conference of spectroscopic ellipsometry
2013-2016	1 st – 3 rd Nano-tera Annual Meeting
June 2015	Swiss Conference on Biomaterials and Regenerative Medicine
June 2014	Gordon Research Conference on Polymer Physics
Talks	
March 2016	SPIE – Smart Materials 2016 in Las Vegas/USA <i>Characterization of ultraviolet light-cured polydimethylsiloxane films for low-voltage dielectric elastomer actuators</i>
May 2015	Nano-tera Annual Meeting in Bern/Switzerland <i>SmartSphincter – biomimetic implant to treat fecal incontinence</i>
March 2011	75. DPG conference in Dresden/Germany <i>GaSb-based semiconductor disk lasers optically pumped at different wavelengths</i>
Awards	
May 2015	3. Poster prize at Nano-tera Annual Meeting
Patents	
March 2014	Title: „Barrieren-gepumpter Halbleiter-Scheibenlaser mit einem aktiven Bereich minimaler Ausdehnung für verbesserte Leistungseffizienz und optimierte Entwärmung“ German patent Nr. 10 2014 205 022.7, submitted as U.S. patent
Supervising	
	M. Karapetkova, Master thesis: <i>Preparation and characterization of micrometer and submicrometer-thin multilayer dielectric elastomer actuators</i> , University of Basel (April 2016)
	F. Wohlfender, Project thesis: <i>Evaluating the elastic properties of ultraviolet-light-cured polydimethylsiloxane thin films for dielectric actuators</i> , University of Basel (June 2015)
	C. Winterhalter, Master thesis: <i>Fabrication and four-point electrical characterization of nanometer-thin gold layers on a soft polymer</i> , ETH Zürich (June 2014)
	C. Winterhalter, Project thesis: <i>Determination of effective elastic moduli from bending measurements of asymmetric planar electrically activated polymers</i> , ETH Zürich (Oct. 2013)
Academic studies, Schooling	
2005-2011	Physics studies at Albert-Ludwigs University of Freiburg
July 2010 – December 2011	Preparation of the diploma thesis at the Fraunhofer Institute of solid state physics (IAF) in Freiburg (Grade 1,0): „ <i>Leistungsgrenzen hocheffizienter 2µm-emittierender Scheibenlaser</i> “.
June 2010	Diploma in experimental- and theoretical physics (Grade 1,3)
February 2009	Diploma in semiconductor physics (Nebenfach) (Grade 1,7)

October 2007	Intermediate diploma in physics, mathematics and meteorology (Grade 2,3)
1996 - 2005	Abitur at Neideck Gymnasium Arnstadt (Grade 1,4) Specialization in physics and mathematics, Award from the „Deutsche Physikalische Gesellschaft“ (DPG) for excellent achievements
IT-knowledge	Office, Mathematica, Origin, Latex, Cad, Photoshop, Illustrator
Interests, Hobbies	
Since 2009	Member of the Oberliga-Volleyball department at SV-Gündlingen Playing piano Photography